A generalised theory for physics-augmented neurals networks in finite strain thermo-electro-mechanics

R. Ortigosa[†1], J. Martínez-Frutos[†2], A. Pérez-Escolar[†], I. Castañar[†], N. Ellmer[‡], A. J. Gil[‡3]

† *Technical University of Cartagena, Campus Muralla del Mar, 30202, Cartagena (Murcia), Spain*
‡*Zienkiewicz Institute for Modelling, Data and AI*
Faculty of Science and Engineering, Swansea University
Bay Campus, SA1 8EN, United Kingdom

Abstract

This manuscript introduces a novel neural network-based computational framework for constitutive modelling of thermo-electro-mechanically coupled materials at finite strains, with four key innovations: (i) It supports calibration of neural network models with various input forms, such as $\Psi_{nn}(\boldsymbol{F}, \boldsymbol{E}_0, \theta)$, $e_{nn}(\boldsymbol{F}, \boldsymbol{D}_0, \eta)$, $\Upsilon_{nn}(\boldsymbol{F}, \boldsymbol{E}_0, \eta)$, or $\Gamma_{nn}(\boldsymbol{F}, \boldsymbol{D}_0, \theta)$, with $\boldsymbol{F}$ representing the deformation gradient tensor, $\boldsymbol{E}_0$ and $\boldsymbol{D}_0$ the electric field and electric displacement field, respectively and finally, θ and η, the temperature and entropy fields. These models comply with physical laws and material symmetries by utilizing isotropic or anisotropic invariants corresponding to the material's symmetry group. (ii) A calibration approach is developed for the case of experimental data, where entropy η is typically unmeasurable. (iii) The framework accommodates models like $e_{nn}(\boldsymbol{F}, \boldsymbol{D}_0, \eta)$, specially convenient for the imposition of polyconvexity across the three physics involved. A detailed calibration study is conducted evaluating various neural network architectures and considering a large variety of ground truth thermo-electro-mechanical constitutive models. The results demonstrate excellent predictive performance on larger datasets, validated through complex finite element simulations using both ground truth and neural network-based models. Crucially, the framework can be straightforwardly extended to scenarios involving other physics.

Keywords: neural networks, machine learning, thermo-electro-mechanics, dielectric elastomers, finite elements.

1. Introduction

Electroactive polymers (EAPs) have emerged as a class of smart materials distinguished by their ability to undergo significant shape transformations in response to electrical stimuli [61, 60, 62, 42, 16]. Among these, dielectric elastomers stand out for their exceptional actuation properties, offering advantages such as light weight, rapid response, flexibility, and low stiffness. These materials are particularly notable for their capacity to sustain electrically induced strains, with area expansions of up to 1962% observed in studies conducted at Harvard's Suo Lab [45]. Their transformative potential is vast, with promising applications in bio-inspired robotics [53, 15, 34, 17, 44], humanoid robots, and advanced prosthetics [48, 74, 16], as well as the exciting frontier of tissue regeneration [54].

Magnetoactive materials represent another class of smart materials with significant applications in soft robotics and biomechanics [52, 6]. These materials leverage magnetic stimuli to

[1]Corresponding author: r.ortigosa@swansea.ac.uk
[2]Corresponding author: jesus.martinez@upct.es
[3]Corresponding author: a.j.gil@swansea.ac.uk

induce controlled deformations, enabling precise, programmable actuation for soft robotic systems [59]. In biomechanical contexts, magnetically driven deformations can be employed to guide cell migration, promoting directional cellular growth and tissue development, offering promising potential for advanced medical and robotic applications [31].

Whilst the primary focus of this paper is on electroactive materials, both electroactive and magnetoactive materials exhibit behavior that is temperature-dependent [50]. As a result, the interaction between mechanical, electrical/magnetic, and thermal effects must be considered to achieve accurate and realistic predictions of their behaviour in numerical simulations. Integrating these three physical domains is essential for capturing the complex response of such materials.

To accurately capture the behavior of electroactive and magnetoactive materials, it is essential to integrate the coupling between their mechanical, electrical/magnetic, and thermal physics within the constitutive model. In purely isothermal and reversible conditions, the constitutive behavior is described by the free energy density, typically expressed in terms of objective invariants of the deformation gradient tensor and either the electric field or its work-conjugate, the electric displacement field [21, 20, 22, 13, 14, 11, 12, 33]. In isothermal electro-mechanics, polyconvexity of the free energy has been extended to account for electro-mechanical interactions [58, 29, 57, 56], building on its original application in finite strain elasticity [2, 3, 5, 67, 68, 69, 70, 66]. For non-isothermal conditions, [51] extended invariant-based free energy formulations to thermo-electroactive materials at finite strains, advancing earlier work by [65, 73].

Recently, Machine Learning techniques have shown great promise in predicting material constitutive responses (i.e. the free energy density of the underlying material), based on experimental data, typically stress-stretch measurements. Additionally, Machine Learning has been employed as a surrogate for phenomenological, invariant-based free energy formulations [40]. Furthermore, these techniques have been applied to predict the homogenized behavior of composite materials [41], which, unless analytical homogeneization techniques can be applied, they would require a multiscale FEM^2 approach. In finite strain scenarios, this poses significant computational challenges due to the high cost of such simulations.

An increasing number of researchers are leveraging Machine Learning, particularly Neural Networks (NNs), for constitutive modeling. Constitutive Artificial Neural Networks (CANNs) have been introduced to ensure physical constraints like objectivity and material symmetry. Kuhl et al. [47] applied CANNs to rubber materials, validating their performance with uniaxial, biaxial, and shear data. Linka et al. [46] compared CANNs to standard NNs, showing that CANNs require less data for training isotropic models. Convexity, important for model stability, has been addressed through convex NNs developed by Klein et al. [39], which use invariants, the deformation gradient, its cofactor, and determinant to build polyconvex models. This approach has been extended to electro-mechanical systems [40, 41]. In addition, the authors in [28] proposed neural network-based models for thermoelasticity complying with both mixed polyconvex-concave conditions for the mechanical and thermal fields involved. Furthermore, the authors in [36] developed neutral network-based constitutive models for finite strain magneto-elasticity. The authors in [38] even explored the use of parametrized polyconvex neural networks, where partial convexity contraints were applied to the mechanical inputs (invariants) of the model, whiole other inputs were left unrestricted. Additionally, the EUCLID framework, developed by De Lorenzis et al. [72, 35, 24], facilitates unsupervised automated discovery of material laws. This method uses a catalogue of constitutive frameworks to fit a range of material data and has been explored with NNs and Bayesian implementations for learning elastic and viscoelastic models with varying anisotropy.

A less common Machine Learning technique is Gaussian Process Regression (GPR), rooted in probability theory. GPR is an interpolation method that uses Gaussian distributions to generate predictive distributions, offering the advantage of uncertainty quantification for error estimation and infill strategies [64, 8, 49, 1]. A key component is the correlation function, with the Radial

Basis Function (RBF) commonly used to correlate observed data in parametric space. Kriging, a GPR variant from geostatistics [1], can incorporate gradient data into the calibration process, known as Gradient Enhanced Kriging [55, 27]. Previous work demonstrated that using gradient data improves performance, allowing for fewer calibration points or enhanced accuracy with the same number of data points [23, 63].

The goal of this paper is to develop a flexible neural network-based framework for constitutive modelling of thermo-electro-mechanically coupled materials at finite strains. This framework enables the calibration of a wide range of free energy densities based on various input combinations, such as $\{\boldsymbol{F}, \boldsymbol{E}_0, \theta\}$, $\{\boldsymbol{F}, \boldsymbol{D}_0, \eta\}$, $\{\boldsymbol{F}, \boldsymbol{E}_0, \eta\}$, or $\{\boldsymbol{F}, \boldsymbol{D}_0, \theta\}$. Here, $\boldsymbol{F}$ represents the deformation gradient, $\boldsymbol{E}_0$ the electric field, $\boldsymbol{D}_0$ the electric displacement field, θ the temperature, and η the entropy field. Additionally, the framework incorporates two distinct calibration strategies tailored for either in-silico generated data or experimental data from laboratory settings, ensuring adaptability across different data sources.

The structure of this paper is as follows: Section 2 introduces the basic principles of kinematics and presents the governing equations of nonlinear thermo-electro-mechanics. Section 3 covers constitutive modeling, beginning with the Helmholtz strain energy density and introducing three alternative thermodynamic potentials derived from partial Legendre transformations, with the mechanical argument, $\boldsymbol{F}$, held constant. Section 4 introduces the two proposed calibration strategies. Section 5 details the finite element implementation of these governing equations in thermo-electro-mechanics. Finally, Section 6 conducts a comprehensive evaluation of the accuracy of the calibrated neural network models, further validated through a complex finite element simulation comparing the ground truth model with its neural network counterpart.

Notation: Throughout this paper, $\boldsymbol{A} : \boldsymbol{B} = A_{iI}B_{iI}$, $\forall \boldsymbol{A}, \boldsymbol{B} \in \mathbb{R}^{3\times3}$, and the use of repeated indices implies summation. The tensor product is denoted by $\otimes$ and the second order identity tensor by $\boldsymbol{I}$. The tensor cross product operation $\boldsymbol{\times}$ between two artibrary second order tensor $\boldsymbol{A}$ and $\boldsymbol{B}$ entails $[\boldsymbol{A} \boldsymbol{\times} \boldsymbol{B}]_{iI} = \mathcal{E}_{ijk}\mathcal{E}_{IJK}A_{jJ}B_{kK}$. Furthermore, $\boldsymbol{\mathcal{E}}$ represents the third-order alternating tensor. Lower case indices $\{i, j, k\}$ will be used to represent the spatial configuration whereas capital case indices $\{I, J, K\}$ will be used to represent the material configuration. The full and special orthogonal groups in $\mathbb{R}^3$ are represented as $\mathrm{O}(3) = \{\boldsymbol{A} \in \mathbb{R}^{3\times3}, | \, \boldsymbol{A}^T\boldsymbol{A} = \boldsymbol{I}\}$ and $\mathrm{SO}(3) = \{\boldsymbol{A} \in \mathbb{R}^{3\times3}, | \, \boldsymbol{A}^T\boldsymbol{A} = \boldsymbol{I}, \det\boldsymbol{A} = 1\}$, respectively and the set of invertible second order tensors with positive determinant is denoted by $\mathrm{GL}^+(3) = \{\boldsymbol{A} \in \mathbb{R}^{3\times3} | \det\boldsymbol{A} > 0\}$. Differentiation with respect to time of any field $(\bullet)$ will be denoted through $\dot{(\bullet)}$.

2. Nonlinear continuum thermo-electro-mechanics

A brief introduction into nonlinear continuum mechanics and the relevant governing equations will be presented in this section.

2.1. Kinematics: motion and deformation

Let us consider the motion of an EAP with reference configuration $\mathcal{B}_0 \in \mathbb{R}^3$ (refer to Figure 1). After the motion, the continuum $\mathcal{B}_0$ occupies a deformed configuration $\mathcal{B} \in \mathbb{R}^3$. The deformation mapping $\boldsymbol{\phi}(\boldsymbol{X}, t)$ links a material particle from the reference configuration $\boldsymbol{X} \in \mathcal{B}_0$ to the deformed configuration $\boldsymbol{x} \in \mathcal{B}$ according to $\boldsymbol{x} = \boldsymbol{\phi}(\boldsymbol{X}, t)$. Associated with $\boldsymbol{\phi}$, we define the deformation gradient tensor $\boldsymbol{F} \in \mathrm{GL}^+(3)$ (or fibre map) [10, 30, 19, 7] as $\boldsymbol{F} = \partial_{\boldsymbol{X}}\boldsymbol{\phi}$. The later permits to introduce its co-factor $\boldsymbol{H}$ (or area map) and its Jacobian J (or volume map), according to

$$\boldsymbol{H} = (\det\boldsymbol{F})\,\boldsymbol{F}^{-T}; \qquad J = \det\boldsymbol{F}, \tag{1}$$

which can be equivalently re-writen as [18, 9] as

$$\boldsymbol{H} = \frac{1}{2}\boldsymbol{F} \boldsymbol{\times} \boldsymbol{F}; \qquad J = \frac{1}{3}\boldsymbol{H} : \boldsymbol{F}. \tag{2}$$

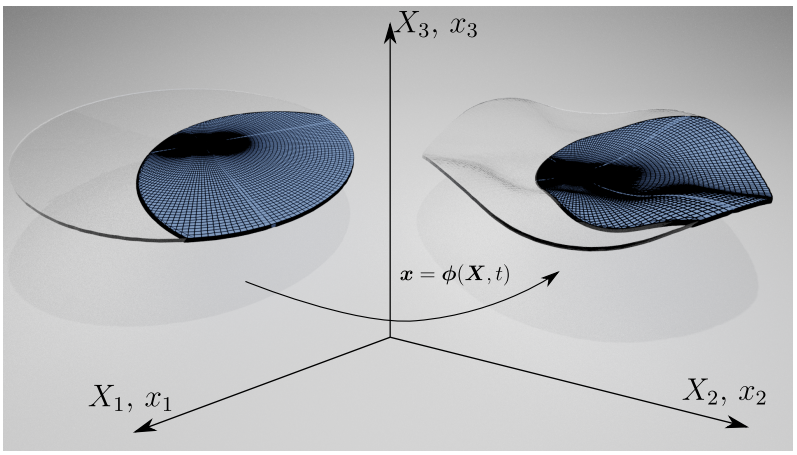

Figure 1: The mapping $\boldsymbol{\phi}$ and the reference $\mathcal{B}_0$ (left) and deformed $\mathcal{B}$ (right) configurations.

2.2. Governing equations in nonlinear thermo-electro-mechanics

The behaviour of the EAP is governed by a system of coupled PDEs. These include the conservation of linear momentum [30], which can be recast in a Lagrangian setting as

$$\begin{aligned} \rho_0 \dot{\boldsymbol{v}} - \mathrm{DIV}\boldsymbol{P} - \boldsymbol{f}_0 &= \boldsymbol{0}; && \text{in } \mathcal{B}_0 \times [0,T]; \\ \boldsymbol{P}\boldsymbol{N}_{\mathcal{B}_0} &= \boldsymbol{t}_0; && \text{on } \partial_{\boldsymbol{t}}\mathcal{B}_0 \times [0,T]; \\ \boldsymbol{\phi} &= \bar{\boldsymbol{\phi}}; && \text{on } \partial_{\boldsymbol{\phi}}\mathcal{B}_0 \times [0,T]; \\ \boldsymbol{\phi}|_{t=0} &= \boldsymbol{\phi}_0; && \text{in } \mathcal{B}_0; \\ \dot{\boldsymbol{\phi}}\Big|_{t=0} &= \boldsymbol{v}_0; && \text{in } \mathcal{B}_0, \end{aligned} \tag{3}$$

where $\rho_0 : \mathcal{B}_0 \to \mathbb{R}^+$ represents the mass density of the continuum in the reference configuration, $\boldsymbol{v}$ the velocity field. Furthermore, $\boldsymbol{f}_0$ represents a body force per unit undeformed volume $\mathcal{B}_0$ and $\boldsymbol{t}_0$, the traction force per unit undeformed area applied on $\partial_{\boldsymbol{t}}\mathcal{B}_0 \subset \partial\mathcal{B}_0$, such that $\partial_{\boldsymbol{t}}\mathcal{B}_0 \cup \partial_{\boldsymbol{\phi}}\mathcal{B}_0 = \partial\mathcal{B}_0$ and $\partial_{\boldsymbol{t}}\mathcal{B}_0 \cap \partial_{\boldsymbol{\phi}}\mathcal{B}_0 = \emptyset$. Moreover, $\bar{\boldsymbol{\phi}}$ represents the Dirichlet condition for $\boldsymbol{\phi}$, $\boldsymbol{\phi}_0$ and $\boldsymbol{v}_0$ are the initial conditions for the mapping $\boldsymbol{\phi}$ and the velocity fields, respectively. Local conservation of angular momentum leads to the well-known tensor condition $\boldsymbol{P}\boldsymbol{F}^T = \boldsymbol{F}\boldsymbol{P}^T$, where $\boldsymbol{P}$ represents the first Piola-Kirchhoff stress tensor. Finally, $\boldsymbol{N}_{\mathcal{B}_0}$ represents the outwardd normal at $\boldsymbol{X} \in \partial_{\boldsymbol{t}}\mathcal{B}_0$, and DIV, the divergence operator in the reference configuration.

The second set of PDEs that govern the behaviour of the EAP comprises the electrostatic form of the Gauss' and Faraday's laws, recast in a Lagrangian setting as follows

$$\begin{aligned} \boldsymbol{E}_0 &= -\partial_{\boldsymbol{X}}\varphi; && \text{in } \mathcal{B}_0 \times [0,T]; \\ \mathrm{DIV}\boldsymbol{D}_0 &= -\rho_0^e; && \text{in } \mathcal{B}_0 \times [0,T]; \\ \boldsymbol{D}_0 \cdot \boldsymbol{N} &= -\omega_0^e; && \text{on } \partial_{\omega}\mathcal{B}_0 \times [0,T]; \\ \varphi &= \bar{\varphi}; && \text{on } \partial_{\varphi}\mathcal{B}_0 \times [0,T], \end{aligned} \tag{4}$$

where $\varphi : \mathcal{B}_0 \to \mathbb{R}$ represents the electric potential, $\rho_0^e : \mathcal{B}_0 \to \mathbb{R}$ is the electric charge per unit volume in the reference configuration and ω_0^e, the electric charge per unit undeformed area applied on $\partial_{\omega}\mathcal{B}_0 \subset \partial\mathcal{B}_0$, such that $\partial_{\omega}\mathcal{B}_0 \cup \partial_{\varphi}\mathcal{B}_0 = \partial\mathcal{B}_0$ and $\partial_{\omega}\mathcal{B}_0 \cap \partial_{\varphi}\mathcal{B}_0 = \emptyset$. Finally, $\bar{\varphi}$ represents the Dirichlet condition for φ. In above equation (4), $\boldsymbol{E}_0$ and $\boldsymbol{D}_0$ represent the material electric field and electric displacement field, respectively.

Finally, the last coupled PDE governing the behaviour of the EAP is the balance of energy, which in the absence of internal state variables (i.e. plastic strain or viscoelasticity), can be

written in a Lagrangian setting as

$$\begin{aligned} \theta\dot{\eta} + \mathrm{DIV}\boldsymbol{Q}_\theta - R_\theta &= 0; && \text{in } \mathcal{B}_0 \times [0,T]; \\ \boldsymbol{Q}_\theta \cdot \boldsymbol{N} &= -Q_\theta; && \text{on } \partial_Q\mathcal{B}_0 \times [0,T]; \\ \theta &= \bar{\theta}; && \text{on } \partial_\theta\mathcal{B}_0 \times [0,T]; \\ \theta|_{t=0} &= \bar{\theta}_0; && \text{in } \mathcal{B}_0, \end{aligned} \tag{5}$$

where θ is the absolute temperature field and η and $\boldsymbol{Q}_\theta$, the entropy and heat flux per unit undeformed volume $\mathcal{B}_0$, respectively. In addition, R_θ represents the heat source per unit undeformed volume $\mathcal{B}_0$, Q_θ, the heat source per unit undeformed area applied on $\partial_Q\mathcal{B}_0 \subset \partial\mathcal{B}_0$, and $\bar{\theta}_0$ the Dirichlet condition for θ. In (5), $\partial_\theta\mathcal{B}_0$ represents the part of the boundary $\partial\mathcal{B}_0$ where essential temperature boundary conditions are applied such that $\partial_Q\mathcal{B}_0 \cup \partial_\theta\mathcal{B}_0 = \partial\mathcal{B}_0$ and $\partial_Q\mathcal{B}_0 \cap \partial_\theta\mathcal{B}_0 = \emptyset$.

3. Constitutive equations in nonlinear thermo-electro-elasticity

The governing equations presented in Section 2 are coupled by means of a suitable constitutive law. The objective of the following section is to introduce some notions on constitutive laws in thermo-electro-elasticity.

3.1. The Helmholtz free energy

In the case of thermo-electro-elasticity, and in the absence of internal state variables, the Helmholtz free energy Ψ per unit of undeformed volume can be defined as

$$\Psi : \mathrm{GL}^+(3) \times \mathbb{R}^3 \times \mathbb{R}^+, \qquad (\boldsymbol{F}, \boldsymbol{E}_0, \theta) \to \Psi\left(\boldsymbol{F}, \boldsymbol{E}_0, \theta\right). \tag{6}$$

In order to derive constitutive equations, we begin with the Clausius-Duhen inequality, which takes the following form

$$-\dot{\Psi} + \boldsymbol{P} : \dot{\boldsymbol{F}} - \boldsymbol{D}_0 \cdot \dot{\boldsymbol{E}}_0 - \eta\dot{\theta} - \frac{1}{\theta}\boldsymbol{Q}_\theta \cdot \partial_{\boldsymbol{X}}\theta \geq 0. \tag{7}$$

For the EAP, following [30, 19], use of the Coleman-Noll procedure into (7) leads to

$$\Big(\boldsymbol{P} - \partial_F\Psi\Big) : \dot{\boldsymbol{F}} - \Big(\boldsymbol{D}_0 + \partial_{\boldsymbol{E}_0}\Psi\Big) \cdot \dot{\boldsymbol{E}}_0 - \Big(\eta + \partial_\theta\Psi\Big)\dot{\theta} - \frac{1}{\theta}\boldsymbol{Q}_\theta \cdot \partial_{\boldsymbol{X}}\theta \geq 0. \tag{8}$$

Fourier law relates the spatial heat flux $\boldsymbol{q}$ and the spatial gradient of θ by virtue of the following expression

$$\boldsymbol{q}_\theta = -\boldsymbol{k}\partial_{\boldsymbol{x}}\theta, \tag{9}$$

where $\boldsymbol{k}$ represents the semi-positive definite second order thermal conductivity tensor in the deformed configuration. The relation between $\boldsymbol{q}_\theta$ and its material counterpart $\boldsymbol{Q}_\theta$ in (5) can be carried out by making use of the Gauss' theorem and the Nanson's rule (i.e. $d\boldsymbol{a} = \boldsymbol{H}d\boldsymbol{A}$) [10], yielding

$$\boldsymbol{Q}_\theta = -\boldsymbol{K}\partial_{\boldsymbol{X}}\theta; \qquad \boldsymbol{K} = J^{-1}\boldsymbol{H}^T\boldsymbol{k}\boldsymbol{H}. \tag{10}$$

Positive definiteness of the material thermal conductivity tensor $\boldsymbol{K}$ permits to establish from equation (8) the following relationships

$$\boldsymbol{P} = \partial_F\Psi(\boldsymbol{F}, \boldsymbol{E}_0, \theta); \qquad \boldsymbol{D}_0 = -\partial_{\boldsymbol{E}_0}\Psi(\boldsymbol{F}, \boldsymbol{E}_0, \theta); \qquad \eta = -\partial_\theta\Psi(\boldsymbol{F}, \boldsymbol{E}_0, \theta). \tag{11}$$

The Helmholtz free energy density must adhere to the principle of objectivity or material frame indifference, which entails its invariance with respect to rotations $\boldsymbol{Q} \in \mathrm{SO}(3)$ applied to the spatial configuration, namely

$$\Psi(\boldsymbol{Q}\boldsymbol{F}, \boldsymbol{E}_0, \theta) = \Psi(\boldsymbol{F}, \boldsymbol{E}_0, \theta); \qquad \forall \boldsymbol{F} \in \mathrm{GL}^+(3),\ \boldsymbol{E}_0 \in \mathbb{R}^3,\ \theta \in \mathbb{R}^+,\ \boldsymbol{Q} \in \mathrm{SO}(3). \tag{12}$$

Furthermore, a second invariance condition must hold, known as the material symmetry conditions, which reads as follows

$$\Psi(\boldsymbol{F}\boldsymbol{Q}^T, \boldsymbol{Q}\boldsymbol{E}_0, \theta) = \Psi(\boldsymbol{F}, \boldsymbol{E}_0, \theta); \qquad \forall \boldsymbol{F} \in \mathrm{GL}^+(3),\, \boldsymbol{E}_0 \in \mathbb{R}^3,\, \theta \in \mathbb{R}^+,\, \boldsymbol{Q} \in \mathcal{G} \subset \mathrm{O}(3), \tag{13}$$

where $\mathcal{G}$ denotes the symmetry group of the material under consideration. Section 3.3 will demonstrate how the two physical conditions specified in equations (12) and (13) can be imposed a priori. Moreover, the Helmholtz free energy density $\Psi(\boldsymbol{F}, \boldsymbol{E}_0, \theta)$, along with the first Piola-Kirchhoff stress tensor $\boldsymbol{P}(\boldsymbol{F}, \boldsymbol{E}_0, \theta)$, the electric displacement field $\boldsymbol{D}_0(\boldsymbol{F}, \boldsymbol{E}_0, \theta)$ and the entropy $\eta(\boldsymbol{F}, \boldsymbol{E}_0, \theta)$ must vanish in the absence of deformations (i.e. $\boldsymbol{F} = \boldsymbol{I}$, with $\boldsymbol{I}$ the second order identity tensor), electric fields (i.e. $\boldsymbol{E}_0 = \boldsymbol{0}$) and when the temperature is equal to the so-called reference temperature, denoted as θ_R. All that is mathematically stated as

$$\begin{aligned} &\Psi(\boldsymbol{F}, \boldsymbol{E}_0, \theta)|_{\boldsymbol{I},\boldsymbol{0},\theta_R} = 0; && \boldsymbol{P}(\boldsymbol{F}, \boldsymbol{E}_0, \theta)|_{\boldsymbol{I},\boldsymbol{0},\theta_R} := \partial_{\boldsymbol{F}}\Psi(\boldsymbol{F}, \boldsymbol{E}_0, \theta)|_{\boldsymbol{I},\boldsymbol{0},\theta_R} = \boldsymbol{0}; \\ &\boldsymbol{D}_0(\boldsymbol{F}, \boldsymbol{E}_0, \theta)|_{\boldsymbol{I},\boldsymbol{0},\theta_R} =: -\partial_{\boldsymbol{E}_0}\Psi(\boldsymbol{F}, \boldsymbol{E}_0, \theta)|_{\boldsymbol{I},\boldsymbol{0},\theta_R} = \boldsymbol{0}; && \eta(\boldsymbol{F}, \boldsymbol{E}_0, \theta)|_{\boldsymbol{I},\boldsymbol{0},\theta_R} := -\partial_{\theta}\Psi(\boldsymbol{F}, \boldsymbol{E}_0, \theta)|_{\boldsymbol{I},\boldsymbol{0},\theta_R} = 0. \end{aligned} \tag{14}$$

Equation (11) establishes the relationship between the first derivatives of the Helmholtz free energy density, namely $\{\boldsymbol{P}, \boldsymbol{D}_0, \eta\}$, with their work conjugates, namely $\{\boldsymbol{F}, \boldsymbol{E}_0, \theta\}$, thus closing the system of coupled PDEs in (2.2), governing the behaviour of EAPs. However, the second derivatives of the Helmholtz energy lead also to constitutive tensors with insightful physical relevance, in particular when characterising the behaviour of the EAP in the linearised regime, i.e. in the vicinity of $\{\boldsymbol{F}, \boldsymbol{E}_0, \theta\} \approx \{\boldsymbol{I}, \boldsymbol{0}, \theta_R\}$. These are embedded within the (symmetric) Hessian of the Helmholtz free energy density, denoted as $[\mathbb{H}_\Psi]$, namely

$$[\mathbb{H}_\Psi] = \begin{bmatrix} \partial^2_{\boldsymbol{F}\boldsymbol{F}}\Psi & \partial^2_{\boldsymbol{F}\boldsymbol{E}_0}\Psi & \partial^2_{\boldsymbol{F}\theta}\Psi \\ & \partial^2_{\boldsymbol{E}_0\boldsymbol{E}_0}\Psi & \partial^2_{\boldsymbol{F}\theta}\Psi \\ \text{sym.} & & \partial^2_{\theta\theta}\Psi \end{bmatrix}, \tag{15}$$

where $\partial^2_{\boldsymbol{F}\boldsymbol{F}}\Psi$ represents the fourth order elasticity tensor, $\partial^2_{\boldsymbol{F}\boldsymbol{E}_0}\Psi$ the third order piezoelectric tensor, $\partial^2_{\boldsymbol{E}_0\boldsymbol{E}_0}\Psi$ represents the second order dielectric tensor, whereas $\partial^2_{\boldsymbol{F}\theta}\Psi$ and $\partial^2_{\boldsymbol{E}_0\theta}\Psi$ are second and first order tensors encoding the influence of the thermal field θ on the first Piola-Kirchhoff stress tensor $\boldsymbol{P}$ and on the electric displacement field $\boldsymbol{D}_0$. Finally, $\partial^2_{\theta\theta}\Psi$ can be related with a relevant physical property of a material, in particular, the specific heat capacity, denoted as c_v, and defined as [73]

$$c_v(\boldsymbol{F}, \boldsymbol{E}_0, \theta) = -\theta\partial^2_{\theta\theta}\Psi(\boldsymbol{F}, \boldsymbol{E}_0, \theta). \tag{16}$$

In addition to the physical conditions encompassing the objectivity condition (12), the material symmetry condition (13) and the reference conditions (14), there are mathematical conditions that the Helmholtz free energy density $\Psi(\boldsymbol{F}, \boldsymbol{E}_0, \theta)$ must comply with. In the context of thermo-electro-elasticity, it is accepted that suitable conditions that $\Psi(\boldsymbol{F}, \boldsymbol{E}_0, \theta)$ must satisfy are: rank-one convexity with respect to the deformation gradient $\boldsymbol{F}$, concavity with respect to $\boldsymbol{E}_0$, and concavity with respect to the absolute temperature θ, i.e.

$$(\boldsymbol{u} \otimes \boldsymbol{V}) : \partial^2_{\boldsymbol{F}\boldsymbol{F}}\Psi : (\boldsymbol{u} \otimes \boldsymbol{V}) \geq 0; \qquad \begin{bmatrix} \boldsymbol{V} \\ \delta\theta \end{bmatrix} : \begin{bmatrix} \partial^2_{\boldsymbol{E}_0\boldsymbol{E}_0}\Psi & \partial^2_{\boldsymbol{E}_0\theta}\Psi \\ \text{sym.} & \partial^2_{\theta\theta}\Psi \end{bmatrix} \begin{bmatrix} \boldsymbol{V} \\ \delta\theta \end{bmatrix} \leq 0, \tag{17}$$

which must hold for $\forall \boldsymbol{u}, \boldsymbol{V} \in \mathbb{R}^3$, $\delta\theta \in \mathbb{R}^+$, $\{\boldsymbol{F}, \boldsymbol{E}_0, \theta\} \in \{\mathrm{GL}^+(3), \mathbb{R}^3, \mathbb{R}^+\}$. Notice that concavity with respect to θ in (17) entails positiveness of the specific heat capacity c_v in (16), whereas the two previous conditions in (17) are related with the concept of material stability and hyperbolicity in the isothermal case [68, 56].

3.2. Alternative thermodynamical potentials

Provided that the Helmholtz free energy density $\Psi(\boldsymbol{F},\boldsymbol{E}_0,\theta)$ is concave with respect to $\boldsymbol{E}_0$ and θ (as specified by the second and third conditions in (17)), it becomes possible to define the following three alternative thermodynamic potentials via appropriate Legendre transformations

$$\begin{aligned} e(\boldsymbol{F},\boldsymbol{D}_0,\eta) &= \inf_{\boldsymbol{E}_0,\theta}\left\{\Psi(\boldsymbol{F},\boldsymbol{E}_0,\theta)+\boldsymbol{E}_0\cdot\boldsymbol{D}_0+\theta\eta\right\};\\ \Upsilon(\boldsymbol{F},\boldsymbol{D}_0,\theta) &= \inf_{\boldsymbol{E}_0}\left\{\Psi(\boldsymbol{F},\boldsymbol{E}_0,\theta)+\boldsymbol{E}_0\cdot\boldsymbol{D}_0\right\};\\ \Gamma(\boldsymbol{F},\boldsymbol{E}_0,\eta) &= \inf_{\theta}\left\{\Psi(\boldsymbol{F},\boldsymbol{E}_0,\theta)+\theta\eta\right\}, \end{aligned} \tag{18}$$

which permits to establish analogous relationships to those in (11) as

$$\begin{aligned} &\boldsymbol{P}=\partial_F e(\boldsymbol{F},\boldsymbol{D}_0,\eta); && \boldsymbol{E}_0=\partial_{\boldsymbol{D}_0} e(\boldsymbol{F},\boldsymbol{D}_0,\eta); && \theta=\partial_\eta e(\boldsymbol{F},\boldsymbol{D}_0,\eta);\\ &\boldsymbol{P}=\partial_F \Upsilon(\boldsymbol{F},\boldsymbol{D}_0,\theta); && \boldsymbol{E}_0=\partial_{\boldsymbol{D}_0} \Upsilon(\boldsymbol{F},\boldsymbol{D}_0,\theta); && \eta=-\partial_\theta \Upsilon(\boldsymbol{F},\boldsymbol{D}_0,\theta);\\ &\boldsymbol{P}=\partial_F \Gamma(\boldsymbol{F},\boldsymbol{E}_0,\eta); && \boldsymbol{D}_0=-\partial_{\boldsymbol{E}_0} \Gamma(\boldsymbol{F},\boldsymbol{E}_0,\eta); && \theta=\partial_\eta \Gamma(\boldsymbol{F},\boldsymbol{E}_0,\eta). \end{aligned} \tag{19}$$

Obviously, the three new potentials, $e(\boldsymbol{F},\boldsymbol{D}_0,\eta)$, $\Upsilon(\boldsymbol{F},\boldsymbol{D}_0,\theta)$ and $\Gamma(\boldsymbol{F},\boldsymbol{D}_0,\eta)$ need to comply with the material frame indifference condition in (12) and with the material symmetry condition in (13). Additionally, in the reference configuration, each of these potentials must comply with the conditions below

$$\begin{aligned} &\left\{\begin{array}{ll} e(\boldsymbol{F},\boldsymbol{D}_0,\eta)|_{\boldsymbol{I},\boldsymbol{0},0}=0; & \boldsymbol{P}(\boldsymbol{F},\boldsymbol{D}_0,\eta)|_{\boldsymbol{I},\boldsymbol{0},0}:=\partial_{\boldsymbol{F}} e(\boldsymbol{F},\boldsymbol{D}_0,\eta)|_{\boldsymbol{I},\boldsymbol{0},0}=\boldsymbol{0};\\ \boldsymbol{E}_0(\boldsymbol{F},\boldsymbol{D}_0,\eta)|_{\boldsymbol{I},\boldsymbol{0},0}:=\partial_{\boldsymbol{D}_0} e(\boldsymbol{F},\boldsymbol{D}_0,\eta)|_{\boldsymbol{I},\boldsymbol{0},0}=\boldsymbol{0}; & \theta(\boldsymbol{F},\boldsymbol{D}_0,\eta)|_{\boldsymbol{I},\boldsymbol{0},0}:=\partial_\eta e(\boldsymbol{F},\boldsymbol{D}_0,\eta)|_{\boldsymbol{I},\boldsymbol{0},0}=\theta_R; \end{array}\right.\\ &\left\{\begin{array}{ll} \Upsilon(\boldsymbol{F},\boldsymbol{D}_0,\theta)|_{\boldsymbol{I},\boldsymbol{0},\theta_R}=0; & \boldsymbol{P}(\boldsymbol{F},\boldsymbol{D}_0,\theta)|_{\boldsymbol{I},\boldsymbol{0},\theta_R}:=\partial_{\boldsymbol{F}}\Upsilon(\boldsymbol{F},\boldsymbol{D}_0,\theta)|_{\boldsymbol{I},\boldsymbol{0},\theta_R}=\boldsymbol{0};\\ \boldsymbol{E}_0(\boldsymbol{F},\boldsymbol{D}_0,\theta)|_{\boldsymbol{I},\boldsymbol{0},\theta_R}:=\partial_{\boldsymbol{D}_0}\Upsilon(\boldsymbol{F},\boldsymbol{D}_0,\theta)|_{\boldsymbol{I},\boldsymbol{0},\theta_R}=\boldsymbol{0}; & \eta(\boldsymbol{F},\boldsymbol{D}_0,\theta)|_{\boldsymbol{I},\boldsymbol{0},\theta_R}:=-\partial_\theta\Upsilon(\boldsymbol{F},\boldsymbol{D}_0,\theta)|_{\boldsymbol{I},\boldsymbol{0},\theta_R}=0; \end{array}\right.\\ &\left\{\begin{array}{ll} \Gamma(\boldsymbol{F},\boldsymbol{D}_0,\eta)|_{\boldsymbol{I},\boldsymbol{0},0}=0; & \boldsymbol{P}(\boldsymbol{F},\boldsymbol{E}_0,\eta)|_{\boldsymbol{I},\boldsymbol{0},0}:=\partial_{\boldsymbol{F}}\Gamma(\boldsymbol{F},\boldsymbol{E}_0,\eta)|_{\boldsymbol{I},\boldsymbol{0},0}=\boldsymbol{0};\\ \boldsymbol{D}_0(\boldsymbol{F},\boldsymbol{E}_0,\eta)|_{\boldsymbol{I},\boldsymbol{0},0}:=-\partial_{\boldsymbol{D}_0}\Gamma(\boldsymbol{F},\boldsymbol{E}_0,\eta)|_{\boldsymbol{I},\boldsymbol{0},0}=\boldsymbol{0}; & \theta(\boldsymbol{F},\boldsymbol{E}_0,\eta)|_{\boldsymbol{I},\boldsymbol{0},0}:=\partial_\eta\Gamma(\boldsymbol{F},\boldsymbol{E}_0,\eta)|_{\boldsymbol{I},\boldsymbol{0},0}=\theta_R. \end{array}\right. \end{aligned} \tag{20}$$

Furthermore, provided that $\Psi(\boldsymbol{F},\boldsymbol{E}_0,\theta)$ is also rank-one convex with respect to $\boldsymbol{F}$ (i.e. first condition in (17)), the resulting thermodynamical potentials in (18) would satisfy the following convexity/concavity properties

$$\begin{aligned} &\begin{bmatrix}(\boldsymbol{u}\otimes\boldsymbol{V})\\ \boldsymbol{V}_\perp\\ \delta\eta\end{bmatrix}:\begin{bmatrix}\partial^2_{\boldsymbol{F}\boldsymbol{F}}e & \partial^2_{\boldsymbol{F}\boldsymbol{D}_0}e & \partial^2_{\boldsymbol{F}\eta}e\\ \partial^2_{\boldsymbol{F}\boldsymbol{F}}e & \partial^2_{\boldsymbol{F}\boldsymbol{D}_0}e & \partial^2_{\boldsymbol{F}\eta}e\\ \partial^2_{\boldsymbol{F}\boldsymbol{F}}e & \partial^2_{\boldsymbol{F}\boldsymbol{D}_0}e & \partial^2_{\boldsymbol{F}\eta}e\end{bmatrix}:\begin{bmatrix}(\boldsymbol{u}\otimes\boldsymbol{V})\\ \boldsymbol{V}_\perp\\ \delta\eta\end{bmatrix}\geq 0;\\ &\begin{bmatrix}(\boldsymbol{u}\otimes\boldsymbol{V})\\ \boldsymbol{V}_\perp\end{bmatrix}:\begin{bmatrix}\partial^2_{\boldsymbol{F}\boldsymbol{F}}\Upsilon & \partial^2_{\boldsymbol{F}\boldsymbol{D}_0}\Upsilon\\ \text{sym.} & \partial^2_{\boldsymbol{D}_0\boldsymbol{D}_0}\Upsilon\end{bmatrix}:\begin{bmatrix}(\boldsymbol{u}\otimes\boldsymbol{V})\\ \boldsymbol{V}_\perp\end{bmatrix}\geq 0; \qquad \partial^2_{\theta\theta}\Upsilon\leq 0;\\ &\begin{bmatrix}(\boldsymbol{u}\otimes\boldsymbol{V})\\ \delta\eta\end{bmatrix}:\begin{bmatrix}\partial^2_{\boldsymbol{F}\boldsymbol{F}}\Gamma & \partial^2_{\boldsymbol{F}\eta}\Gamma\\ \text{sym.} & \partial^2_{\eta\eta}\Gamma\end{bmatrix}:\begin{bmatrix}(\boldsymbol{u}\otimes\boldsymbol{V})\\ \delta\eta\end{bmatrix}\geq 0; \qquad \boldsymbol{V}\cdot\partial^2_{\boldsymbol{E}_0\boldsymbol{E}_0}\Gamma\,\boldsymbol{V}\geq 0, \end{aligned} \tag{21}$$

which must hold for

$$\begin{aligned} &\boldsymbol{u},\boldsymbol{V},\boldsymbol{V}_\perp\in\mathbb{R}^3,\delta\eta\in\mathbb{R}, && \{\boldsymbol{F},\boldsymbol{D}_0,\eta\}\in\{\mathrm{GL}^+(3),\mathbb{R}^3,\mathbb{R}\};\\ &\boldsymbol{u},\boldsymbol{V},\boldsymbol{V}_\perp\in\mathbb{R}^3, && \{\boldsymbol{F},\boldsymbol{D}_0,\theta\}\in\{\mathrm{GL}^+(3),\mathbb{R}^3,\mathbb{R}^+\};\\ &\boldsymbol{u},\boldsymbol{V}\in\mathbb{R}^3,\delta\eta\in\mathbb{R}, && \{\boldsymbol{F},\boldsymbol{E}_0,\eta\}\in\{\mathrm{GL}^+(3),\mathbb{R}^3,\mathbb{R}\}, \end{aligned} \tag{22}$$

respectively, where $\boldsymbol{V}_\perp$ is such that $\boldsymbol{V}_\perp\cdot\boldsymbol{V}=0$. Above conditions, in conjunction with (17) dictate that the four potentials, namely $\Psi(\boldsymbol{F},\boldsymbol{E}_0,\theta)$, $e(\boldsymbol{F},\boldsymbol{D}_0,\eta)$, $\Upsilon(\boldsymbol{F},\boldsymbol{D}_0,\theta)$ and $\Gamma(\boldsymbol{F},\boldsymbol{E}_0,\theta)$,

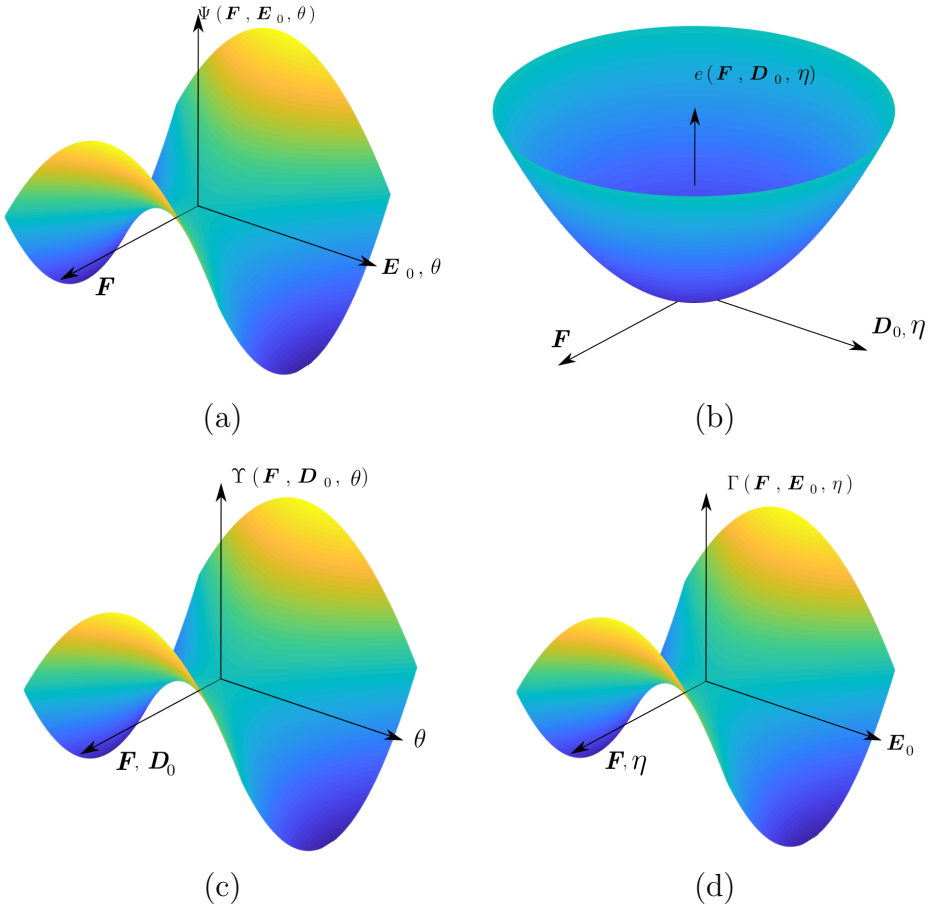

Figure 2: Convexity/concavity properties of the various thermodynamical potentials $\Psi(\boldsymbol{F}, \boldsymbol{E}_0, \theta)$, $e(\boldsymbol{F}, \boldsymbol{D}_0, \eta)$, $\Upsilon(\boldsymbol{F}, \boldsymbol{D}_0, \theta)$ and $\Gamma(\boldsymbol{F}, \boldsymbol{E}_0, \theta)$ in the vicinity of the reference configuration (i.e. $\boldsymbol{F} \approx \boldsymbol{I}$, $\boldsymbol{E}_0 \approx \boldsymbol{0}$ and $\theta \approx \theta_R$). Specifically, we observe: $\Psi(\boldsymbol{F}, \boldsymbol{E}_0, \theta)$ is convex with respect to $\boldsymbol{F}$ and concave with respect to $\{\boldsymbol{E}_0, \theta\}$; $e(\boldsymbol{F}, \boldsymbol{D}_0, \eta)$ is convex with respect to $\{\boldsymbol{F}, \boldsymbol{D}_0, \eta\}$; $\Upsilon(\boldsymbol{F}, \boldsymbol{D}_0, \theta)$ is convex with respect to $\{\boldsymbol{F}, \boldsymbol{D}_0\}$ and concave with respect to θ; $\Gamma(\boldsymbol{F}, \boldsymbol{E}_0, \eta)$ is convex with respect to $\{\boldsymbol{F}, \eta\}$ and concave with respect to $\boldsymbol{E}_0$.

in the vicinity of the reference configuration, namely $\boldsymbol{F} \approx \boldsymbol{I}$, $\boldsymbol{E}_0 \approx \boldsymbol{0}$ and $\theta \approx \theta_R$, will adopt the convexity/concavity properties displayed in Figure (2).

As discussed in [29], defining phenomenological thermodynamic potentials that must satisfy both rank-one convexity and concavity conditions-such as $\Psi(\boldsymbol{F}, \boldsymbol{E}_0, \theta)$, $\Upsilon(\boldsymbol{F}, \boldsymbol{D}_0, \theta)$, and $\Gamma(\boldsymbol{F}, \boldsymbol{E}_0, \eta)$-is generally more challenging than when the potential is only required to be rank-one convex or convex with respect to all its arguments, as is the case with the internal energy $e(\boldsymbol{F}, \boldsymbol{D}_0, \theta)$. Motivated by this simplification, the authors in [29, 57] aimed to define constitutive models for the internal energy of EAPs within the framework of isothermal electro-mechanics. This was achieved by extending the concept of polyconvexity [2, 70, 66, 71], originally from hyperelasticity (purely mechanical systems), to this multi-physics context. Indeed, a sufficient condition for ensuring the rank-one convexity of $e(\boldsymbol{F}, \boldsymbol{D}_0, \eta)$, as shown in equation (21), can be fulfilled through the polyconvexity of $e(\boldsymbol{F}, \boldsymbol{D}_0, \eta)$. For this purpose, we assume the existence of a function $\mathbb{W}$ such that:

$$\mathbb{W} : \mathrm{GL}^+(3) \times \mathrm{GL}^+(3) \times \mathbb{R}^+ \times \mathbb{R}^3 \times \mathbb{R}^3 \times \mathbb{R}, \qquad (\boldsymbol{F}, \boldsymbol{H}, J, \boldsymbol{D}_0, \boldsymbol{d}, \eta) \to \mathbb{W}(\boldsymbol{F}, \boldsymbol{H}, J, \boldsymbol{D}_0, \boldsymbol{d}, \eta), \tag{23}$$

where $\boldsymbol{H}$ and J are the co-factor and determinant of $\boldsymbol{F}$, defined in (1) and (2), whilst $\boldsymbol{d}$ is a field obtained as $\boldsymbol{d} = \boldsymbol{F}\boldsymbol{D}_0$. Then, $e(\boldsymbol{F}, \boldsymbol{D}_0, \eta)$ is said to be polyconvex [2, 4, 5] if it can be equivalently written as

$$e(\boldsymbol{F}, \boldsymbol{D}_0, \eta) = \mathbb{W}(\boldsymbol{F}, \boldsymbol{H}, J, \boldsymbol{D}_0, \boldsymbol{d}, \eta), \tag{24}$$

where $\mathbb{W}(\boldsymbol{F}, \boldsymbol{H}, J, \boldsymbol{D}_0, \boldsymbol{d}, \eta)$ must be convex with respect to all its arguments. For twicely differentiable functions, convexity of $\mathbb{W}(\boldsymbol{F}, \boldsymbol{H}, J, \boldsymbol{D}_0, \boldsymbol{d}, \eta)$ is equivalent to positive definiteness of its Hessian operator $[\mathbb{H}_{\mathbb{W}}]$, i.e.

$$\delta\mathcal{V}^T : [\mathbb{H}_{\mathbb{W}}] : \delta\mathcal{V} \geq 0, \quad \forall\, \delta\mathcal{V} = \begin{bmatrix} \delta\boldsymbol{F} & \delta\boldsymbol{H} & \delta J & \delta\boldsymbol{D}_0 & \delta\boldsymbol{d} & \delta\eta \end{bmatrix}^T, \tag{25}$$

where the (symmetric) Hessian operator $[\mathbb{H}_{\mathbb{W}}]$ incorporates all the second derivatives of $\mathbb{W}$, i.e.

$$[\mathbb{H}_{\mathbb{W}}] = \begin{bmatrix} \partial^2_{\boldsymbol{F}\boldsymbol{F}}\mathbb{W} & \partial^2_{\boldsymbol{F}\boldsymbol{H}}\mathbb{W} & \partial^2_{\boldsymbol{F}J}\mathbb{W} & \partial^2_{\boldsymbol{F}\boldsymbol{D}_0}\mathbb{W} & \partial^2_{\boldsymbol{F}\boldsymbol{d}}\mathbb{W} & \partial^2_{\boldsymbol{F}\eta}\mathbb{W} \\ & \partial^2_{\boldsymbol{H}\boldsymbol{H}}\mathbb{W} & \partial^2_{\boldsymbol{H}J}\mathbb{W} & \partial^2_{\boldsymbol{H}\boldsymbol{D}_0}\mathbb{W} & \partial^2_{\boldsymbol{H}\boldsymbol{d}}\mathbb{W} & \partial^2_{\boldsymbol{H}\eta}\mathbb{W} \\ & & \partial^2_{JJ}\mathbb{W} & \partial^2_{J\boldsymbol{D}_0}\mathbb{W} & \partial^2_{J\boldsymbol{d}}\mathbb{W} & \partial^2_{J\eta}\mathbb{W} \\ & & & \partial^2_{\boldsymbol{D}_0\boldsymbol{D}_0}\mathbb{W} & \partial^2_{\boldsymbol{D}_0\boldsymbol{d}}\mathbb{W} & \partial^2_{\boldsymbol{D}_0\eta}\mathbb{W} \\ \text{sym.} & & & & \partial^2_{\boldsymbol{d}\boldsymbol{d}}\mathbb{W} & \partial^2_{\boldsymbol{d}\eta}\mathbb{W} \\ & & & & & \partial^2_{\eta\eta}\mathbb{W} \end{bmatrix}. \tag{26}$$

3.3. Invariant-based thermo-electro-mechanics

A simple manner to accommodate the principle of objectivity or material frame indifference and the requirement of material symmetry is through the dependence of any of the thermodynamical potentials, namely $\Psi(\boldsymbol{F}, \boldsymbol{E}_0, \theta)$, $e(\boldsymbol{F}, \boldsymbol{D}_0, \eta)$, $\Upsilon(\boldsymbol{F}, \boldsymbol{D}_0, \theta)$ or $\Gamma(\boldsymbol{F}, \boldsymbol{E}_0, \eta)$ with respect to invariants of the right Cauchy-Green deformation gradient tensor $\boldsymbol{C} = \boldsymbol{F}^T\boldsymbol{F}$, $\boldsymbol{E}_0$ or $\boldsymbol{D}_0$ and also with respect to θ or η. Let us denote as $\mathbf{I}_\Psi$, $\mathbf{I}_e$, $\mathbf{I}_\Upsilon$ and $\mathbf{I}_\Gamma$ the set of electro-mechanical objective invariants of $\Psi(\boldsymbol{F}, \boldsymbol{E}_0, \theta)$, $e(\boldsymbol{F}, \boldsymbol{D}_0, \eta)$, $\Upsilon(\boldsymbol{F}, \boldsymbol{D}_0, \theta)$ or $\Gamma(\boldsymbol{F}, \boldsymbol{E}_0, \eta)$, respectively, required to characterise a given material symmetry group $\mathcal{G}$. Then, it is possible to express the four thermodynamical potentials equivalently as

$$\begin{aligned} \Psi(\boldsymbol{F}, \boldsymbol{E}_0, \theta) &= \mathbb{U}_\Psi(\mathbf{I}_\Psi(\boldsymbol{C}, \boldsymbol{E}_0), \theta); & e(\boldsymbol{F}, \boldsymbol{D}_0, \eta) &= \mathbb{U}_e(\mathbf{I}_e(\boldsymbol{C}, \boldsymbol{D}_0), \eta); \\ \Upsilon(\boldsymbol{F}, \boldsymbol{D}_0, \theta) &= \mathbb{U}_\Upsilon(\mathbf{I}_\Upsilon(\boldsymbol{C}, \boldsymbol{D}_0), \theta); & \Gamma(\boldsymbol{F}, \boldsymbol{E}_0, \eta) &= \mathbb{U}_\Gamma(\mathbf{I}_\Gamma(\boldsymbol{C}, \boldsymbol{E}_0), \eta). \end{aligned} \tag{27}$$

Application of the chain rule into equation (11) or (19) permits of obtain the first Piola-Kirchhoff stress tensor $\boldsymbol{P}$, $\boldsymbol{D}_0$ or $\boldsymbol{E}_0$, and θ or η in terms of the derivatives of above invariant-based

potentials with respect to their arguments

$$
\begin{aligned}
&\boldsymbol{P}=\sum_{i=1}^{n}\Big(\partial_{I_{\Psi_i}}\mathbb{U}_{\Psi}\Big)\partial_{\boldsymbol{F}}I_{\Psi_i}; && \boldsymbol{D}_0=-\sum_{i=1}^{n}\Big(\partial_{I_{\Psi_i}}\mathbb{U}_{\Psi}\Big)\partial_{\boldsymbol{E}_0}I_{\Psi_i}; && \eta=-\partial_{\theta}\mathbb{U}_{\Psi};\\
&\boldsymbol{P}=\sum_{i=1}^{n}\Big(\partial_{I_{e_i}}\mathbb{U}_{e}\Big)\partial_{\boldsymbol{F}}I_{e_i}; && \boldsymbol{E}_0=\sum_{i=1}^{n}\Big(\partial_{I_{e_i}}\mathbb{U}_{e}\Big)\partial_{\boldsymbol{D}_0}I_{e_i}; && \theta=\partial_{\eta}\mathbb{U}_{e};\\
&\boldsymbol{P}=\sum_{i=1}^{n}\Big(\partial_{I_{\Upsilon_i}}\mathbb{U}_{\Upsilon}\Big)\partial_{\boldsymbol{F}}I_{\Upsilon_i}; && \boldsymbol{E}_0=\sum_{i=1}^{n}\Big(\partial_{I_{\Upsilon_i}}\mathbb{U}_{\Upsilon}\Big)\partial_{\boldsymbol{D}_0}I_{\Upsilon_i}; && \eta=-\partial_{\theta}\mathbb{U}_{\Upsilon};\\
&\boldsymbol{P}=\sum_{i=1}^{n}\Big(\partial_{I_{\Psi_i}}\mathbb{U}\Big)\partial_{\boldsymbol{F}}I_{\Psi_i}; && \boldsymbol{D}_0=-\sum_{i=1}^{n}\Big(\partial_{I_{\Gamma_i}}\mathbb{U}_{\Gamma}\Big)\partial_{\boldsymbol{E}_0}I_{\Gamma_i}; && \theta=\partial_{\eta}\mathbb{U}_{\Gamma}.
\end{aligned}
\tag{28}
$$

where n represents the number of invariants used, which will be specified in the forthcoming sections.

3.3.1. Electro-mechanical invariants for isotropy

For the case of isotropy, the invariants required to characterise this material symmetry group for the thermodynamical potentials depending on $\boldsymbol{E}_0$, namely $\Psi(\boldsymbol{F},\boldsymbol{E}_0,\theta)$ and $\Gamma(\boldsymbol{F},\boldsymbol{E}_0,\eta)$, and the first derivatives of the latter with respect to $\boldsymbol{F}$ and $\boldsymbol{E}_0$ (featuring in the definition of $\boldsymbol{P}$ and $\boldsymbol{D}_0$ in (28)) are

$$
\begin{aligned}
&I_{\Psi_1}:=\boldsymbol{F}:\boldsymbol{F}=\mathrm{tr}(\boldsymbol{C}), && \partial_{\boldsymbol{F}}I_{\Psi_1}=2\boldsymbol{F}, && \partial_{\boldsymbol{D}_0}I_{\Psi_1}=\boldsymbol{0},\\
&I_{\Psi_2}:=\boldsymbol{H}:\boldsymbol{H}=\mathrm{tr}(\mathrm{Cof}\boldsymbol{C}), && \partial_{\boldsymbol{F}}I_{\Psi_2}=2\boldsymbol{H}\times\boldsymbol{F}, && \partial_{\boldsymbol{E}_0}I_{\Psi_2}=\boldsymbol{0},\\
&I_{\Psi_3}:=J=(\det\boldsymbol{C})^{1/2}, && \partial_{\boldsymbol{F}}I_{\Psi_3}=\boldsymbol{H}, && \partial_{\boldsymbol{D}_0}I_{\Psi_3}=0,\\
&I_{\Psi_4}:=\boldsymbol{E}_0\cdot\boldsymbol{E}_0, && \partial_{\boldsymbol{F}}I_{\Psi_4}=\boldsymbol{0}, && \partial_{\boldsymbol{E}_0}I_{\Psi_4}=2\boldsymbol{E}_0,\\
&I_{\Psi_5}:=\boldsymbol{F}\boldsymbol{E}_0\cdot\boldsymbol{F}\boldsymbol{E}_0=\boldsymbol{E}_0\cdot\boldsymbol{C}\boldsymbol{E}_0, && \partial_{\boldsymbol{F}}I_{\Psi_5}=2\boldsymbol{F}\boldsymbol{E}_0\otimes\boldsymbol{E}_0, && \partial_{\boldsymbol{E}_0}I_{\Psi_5}=2\boldsymbol{C}\boldsymbol{E}_0,\\
&I_{\Psi_6}:=\boldsymbol{H}\boldsymbol{E}_0\cdot\boldsymbol{H}\boldsymbol{E}_0=\boldsymbol{E}_0\cdot\mathrm{Cof}\boldsymbol{C}\boldsymbol{E}_0, && \partial_{\boldsymbol{F}}I_{\Psi_6}=\Big(2\boldsymbol{H}\boldsymbol{E}_0\otimes\boldsymbol{E}_0\Big)\times\boldsymbol{F}, && \partial_{\boldsymbol{E}_0}I_{\Psi_6}=2\mathrm{Cof}\boldsymbol{C}\boldsymbol{E}_0.
\end{aligned}
\tag{29}
$$

with $I_{\Psi_i}=I_{\Gamma_i}$, for $i=\{1,\dots,5\}$. On the other hand, for the thermodynamical potentials depending on $\boldsymbol{D}_0$, namely $e(\boldsymbol{F},\boldsymbol{D}_0,\eta)$ and $\Upsilon(\boldsymbol{F},\boldsymbol{D}_0,\theta)$, the invariants and their first derivatives with respect to $\boldsymbol{F}$ and $\boldsymbol{D}_0$ (featuring in the definition of $\boldsymbol{P}$ and $\boldsymbol{E}_0$ in (28)) are the same as those in (29), where $\boldsymbol{E}_0$ has been replaced with $\boldsymbol{D}_0$, namely

$$
\begin{aligned}
&I_{e_1}:=\boldsymbol{F}:\boldsymbol{F}=\mathrm{tr}(\boldsymbol{C}), && \partial_{\boldsymbol{F}}I_{e_1}=2\boldsymbol{F}, && \partial_{\boldsymbol{D}_0}I_{e_1}=\boldsymbol{0},\\
&I_{e_2}:=\boldsymbol{H}:\boldsymbol{H}=\mathrm{tr}(\mathrm{Cof}\boldsymbol{C}), && \partial_{\boldsymbol{F}}I_{e_2}=2\boldsymbol{H}\times\boldsymbol{F}, && \partial_{\boldsymbol{D}_0}I_{e_2}=\boldsymbol{0},\\
&I_{e_3}:=J=(\det\boldsymbol{C})^{1/2}, && \partial_{\boldsymbol{F}}I_{e_3}=\boldsymbol{H}, && \partial_{\boldsymbol{D}_0}I_{e_3}=0,\\
&I_{e_4}:=\boldsymbol{D}_0\cdot\boldsymbol{D}_0, && \partial_{\boldsymbol{F}}I_{e_4}=\boldsymbol{0}, && \partial_{\boldsymbol{D}_0}I_{e_4}=2\boldsymbol{D}_0,\\
&I_{e_5}:=\boldsymbol{F}\boldsymbol{D}_0\cdot\boldsymbol{F}\boldsymbol{D}_0=\boldsymbol{D}_0\cdot\boldsymbol{C}\boldsymbol{D}_0, && \partial_{\boldsymbol{F}}I_{e_5}=2\boldsymbol{F}\boldsymbol{D}_0\otimes\boldsymbol{D}_0, && \partial_{\boldsymbol{D}_0}I_{e_5}=2\boldsymbol{C}\boldsymbol{D}_0,\\
&I_{e_6}:=\boldsymbol{H}\boldsymbol{D}_0\cdot\boldsymbol{H}\boldsymbol{D}_0=\boldsymbol{D}_0\cdot\mathrm{Cof}\boldsymbol{C}\boldsymbol{D}_0, && \partial_{\boldsymbol{F}}I_{e_6}=\Big(2\boldsymbol{H}\boldsymbol{D}_0\otimes\boldsymbol{D}_0\Big)\times\boldsymbol{F}, && \partial_{\boldsymbol{D}_0}I_{e_6}=2\mathrm{Cof}\boldsymbol{C}\boldsymbol{D}_0.
\end{aligned}
\tag{30}
$$

with $I_{e_i}=I_{\Upsilon_i}$, for $i=\{1,\dots,6\}$.

3.3.2. Electro-mechanical invariants for transverse isotropy

In the context of transverse isotropy, a preferred direction $\boldsymbol{N}$ emerges, perpendicular to the material's plane of isotropy, imparting anisotropic characteristics. Our focus is on the material symmetry group $\mathcal{D}_{\infty h}$ [32], where the structural tensor takes the form $\boldsymbol{N}\otimes\boldsymbol{N}$. This group is distinct from $\mathcal{C}_{\infty}$, also present in transversely isotropic materials, characterized by the structural

vector $\boldsymbol{N}$ and encompassing the potential for piezoelectricity. The $\mathcal{D}_{\infty h}$ group, beyond the invariants $\{I_1, I_2, I_3, I_4, I_5, I_6\}$ in (29), is distinguished by three additional invariants, which for the case of the thermodynamical potentials $\Psi(\boldsymbol{F}, \boldsymbol{E}_0, \theta)$ and $\Gamma(\boldsymbol{F}, \boldsymbol{E}_0, \eta)$ are detailed below

$$\begin{aligned}
&I_{\Psi_7} = \boldsymbol{F}\boldsymbol{N}\cdot\boldsymbol{F}\boldsymbol{N} = \mathrm{tr}\left(\boldsymbol{C}\boldsymbol{N}\otimes\boldsymbol{C}\right), && \partial_{\boldsymbol{F}} I_{\Psi_7} = 2\boldsymbol{F}\boldsymbol{N}\otimes\boldsymbol{N}, && \partial_{\boldsymbol{E}_0} I_{\Psi_7} = \boldsymbol{0},\\
&I_{\Psi_8} = \boldsymbol{H}\boldsymbol{N}\cdot\boldsymbol{H}\boldsymbol{N} = \mathrm{tr}(\mathrm{Cof}\boldsymbol{C}), && \partial_{\boldsymbol{F}} I_{\Psi_8} = 2\left(\boldsymbol{H}\boldsymbol{N}\otimes\boldsymbol{N}\right)\boldsymbol{\times}\boldsymbol{F}, && \partial_{\boldsymbol{E}_0} I_{\Psi_8} = \boldsymbol{0},\\
&I_{\Psi_9} = \left(\boldsymbol{E}_0\cdot\boldsymbol{N}\right)^2, && \partial_{\boldsymbol{F}} I_{\Psi_9} = \boldsymbol{0}, && \partial_{\boldsymbol{E}_0} I_{\Psi_9} = 2(\boldsymbol{E}_0\cdot\boldsymbol{N})\boldsymbol{N},
\end{aligned} \tag{31}$$

with $I_{\Psi_i} = I_{\Gamma_i}$, for $i = \{1, \ldots, 9\}$. On the other hand, for the thermodynamical potentials depending on $\boldsymbol{D}_0$, namely $e(\boldsymbol{F}, \boldsymbol{D}_0, \eta)$ and $\Upsilon(\boldsymbol{F}, \boldsymbol{D}_0, \theta)$, the invariants and their first derivatives with respect to $\boldsymbol{F}$ and $\boldsymbol{D}_0$ (featuring in the definition of $\boldsymbol{P}$ and $\boldsymbol{E}_0$ in (28)), in addition to those in (30), are equivalent to those in equation (31), replacing $\boldsymbol{E}_0$ with $\boldsymbol{D}_0$, namely

$$\begin{aligned}
&I_{e_7} = \boldsymbol{F}\boldsymbol{N}\cdot\boldsymbol{F}\boldsymbol{N} = \mathrm{tr}\left(\boldsymbol{C}\boldsymbol{N}\otimes\boldsymbol{C}\right), && \partial_{\boldsymbol{F}} I_{e_7} = 2\boldsymbol{F}\boldsymbol{N}\otimes\boldsymbol{N}, && \partial_{\boldsymbol{D}_0} I_{e_7} = \boldsymbol{0},\\
&I_{e_8} = \boldsymbol{H}\boldsymbol{N}\cdot\boldsymbol{H}\boldsymbol{N} = \mathrm{tr}(\mathrm{Cof}\boldsymbol{C}), && \partial_{\boldsymbol{F}} I_{e_8} = 2\left(\boldsymbol{H}\boldsymbol{N}\otimes\boldsymbol{N}\right)\boldsymbol{\times}\boldsymbol{F}, && \partial_{\boldsymbol{D}_0} I_{e_8} = \boldsymbol{0},\\
&I_{\Psi_9} = \left(\boldsymbol{D}_0\cdot\boldsymbol{N}\right)^2, && \partial_{\boldsymbol{F}} I_{e_9} = \boldsymbol{0}, && \partial_{\boldsymbol{D}_0} I_{e_9} = 2(\boldsymbol{D}_0\cdot\boldsymbol{N})\boldsymbol{N},
\end{aligned} \tag{32}$$

with $I_{e_i} = I_{\Upsilon_i}$, for $i = \{1, \ldots, 9\}$.

3.4. The ground truth thermo-electro-mechanical Helmholtz free energy free density

In this study, we will calibrate our neural network-based constitutive models using a series of in-silico datasets derived from various ground truth constitutive models. Each of these models will be formulated based on a Helmholtz free energy density that shares a common structural framework, as established by the seminal work of [65] in the domain of thermo-mechanics, and further extended by [51] in the context of thermo-electro-mechanics. Consequently, all ground truth models will be defined in accordance with the following decomposition:

$$\Psi\left(\boldsymbol{F}, \boldsymbol{E}_0, \theta\right) = \mathcal{F}(\theta)\Big(\Psi_m\left(\boldsymbol{F}\right) + \Psi_{em}\left(\boldsymbol{F}, \boldsymbol{E}_0\right)\Big) + \Psi_\theta(\theta) + \left(1 - \frac{\theta}{\theta_R}\right)\Gamma_R\left(J\right), \tag{33}$$

- The sum of $\Psi_m\left(\boldsymbol{F}\right)$ and $\Psi_{em}\left(\boldsymbol{F}, \boldsymbol{E}_0\right)$ corresponds with the Helmholtz free energy density in particular isothermal case when $\theta = \theta_R$.
- $\Gamma_R(J)$ corresponds with the thermodynamical potential $\Gamma(\boldsymbol{F}, \boldsymbol{E}_0, \eta)$ at the reference temperature, i.e. $\theta = \theta_R$. In general, Γ_R could be a function of both $\boldsymbol{F}$ and $\boldsymbol{E}_0$. However, following [65], we only allow for a dependence of Γ_R with respect to the volumetric part of $\boldsymbol{F}$ according to

  $$\Gamma_R(J) = \alpha_0\kappa_0(J-1)\theta_R, \tag{34}$$

  where α_0 and κ_0 refer to the thermal expansion coefficient and the bulk modulus of the material in the reference configuration.
- The function $\mathcal{F}(\theta)$ is introduced to incorporate a nonlinear dependence of stresses with respect to the thermal field. Following [65], we advocate for the following definition of $\mathcal{F}(\theta)$

  $$\mathcal{F}(\theta) = \left(\frac{\theta}{\theta_R} + g(\theta) - g(\theta)|_{\theta_R} + \partial_\theta g|_{\theta_R}\left(\theta_R - \theta\right)\right) \tag{35}$$

where $g(\theta)$ is a nonlinear function of θ. In this work, following [65], we have made use of the following definition for $g(\theta)$

$$g(\theta) = b\left(\frac{\theta}{\theta_R}\right)^a. \tag{36}$$

The nonlinearity of stresses with respect to the thermal field can indeed be observed computing the second derivative of $\boldsymbol{P}$ in equation (11) with respect to θ, yielding

$$\partial^2_{\theta\theta}\boldsymbol{P} = \mathcal{F}''(\theta)\Big(\partial_{\boldsymbol{F}}\Psi_m\left(\boldsymbol{F}\right) + \partial_{\boldsymbol{F}}\Psi_{em}\left(\boldsymbol{F},\boldsymbol{E}_0\right)\Big) \neq \boldsymbol{0} \iff \mathcal{F}''(\theta) \neq 0. \tag{37}$$

Provided that $\mathcal{F}''(\theta) = g''(\theta)$ is a nonlinear function, in general its second derivative with respect to θ would not vanish and hence, $\boldsymbol{P}$ will have a nonlinear character with respect to θ. Figure 3_a illustrates the nonlinear behaviour of $\boldsymbol{P}$ for various values of the coefficients a and b in the function $g(\theta)$ in (36), having fixed $\boldsymbol{F}$ and $\boldsymbol{E}_0$ according to

$$\boldsymbol{F} = \begin{bmatrix} 1.8 & 0 & 0 \\ 0 & 1 & 0 \\ 0 & 0 & 1/1.8 \end{bmatrix}; \qquad \boldsymbol{E}_0 = \boldsymbol{0}. \tag{38}$$

- The purely temperature dependent contribution $\Psi_\theta(\theta)$ is defined as

$$\Psi_\theta = c_{vR}\Big(\theta - \theta_R - \theta\log\frac{\theta}{\theta_R}\Big), \tag{39}$$

where c_{vR} represents the specific heat capacity at the reference configuration. At any other configuration, the specific heat capacity $c_v(\boldsymbol{F},\boldsymbol{E}_0,\theta)$ is obtained by means of equation (16), yielding

$$\begin{aligned} c_v(\boldsymbol{F},\boldsymbol{E}_0,\theta) &= -\theta\Big(\Psi_m\left(\boldsymbol{F}\right) + \Psi_{em}\left(\boldsymbol{F},\boldsymbol{E}_0\right)\Big)\mathcal{F}''(\theta) - \theta\partial^2_{\theta\theta}\Psi_\theta \\ &= -\theta\Big(\Psi_m\left(\boldsymbol{F}\right) + \Psi_{em}\left(\boldsymbol{F},\boldsymbol{E}_0\right)\Big)g''(\theta) + c_{vR}, \end{aligned} \tag{40}$$

where use of (35) has been made in (40). Substituting at the reference configuration, i.e. $\{\boldsymbol{F},\boldsymbol{E}_0,\theta\} = \{\boldsymbol{I},\boldsymbol{0},\theta_R\}$, the specific heat capacity coincides indeed with c_{vR}, i.e.

$$c_v|_{\boldsymbol{I},\boldsymbol{0},\theta_R} = -\theta_R \underbrace{\Big(\Psi_m\left(\boldsymbol{F}\right)|_{\boldsymbol{I}} + \Psi_{em}\left(\boldsymbol{F},\boldsymbol{E}_0\right)|_{\boldsymbol{I},\boldsymbol{0}}\Big)}_{=0} g''(\theta)|_{\theta_R} + c_{vR}, \tag{41}$$

where the isothermal electro-mechanical Helmholtz energy density (underbraced term) must vanish by construction in the reference configuration, hence obtaining $c_v|_{\boldsymbol{I},\boldsymbol{0},\theta_R} = c_{vR}$. It is worth noticing from equation (40) that the model advocated for allows for a nonlinear dependence of the specific heat capacity c_v with respect to the deformation and electric field, and also with respect to temperature. This combined nonlinear dependence is reflected in Figure 3_b, where the deformation gradient tensor $\boldsymbol{F}$ and electric field $\boldsymbol{E}_0$ have been fixed to the same values as in equation (38).

3.5. Specific forms of $\Psi_m(\boldsymbol{F})$ and $\Psi_{em}(\boldsymbol{F},\boldsymbol{E}_0)$

In the generic expression of the Helmholtz energy density, $\Psi(\boldsymbol{F},\boldsymbol{E}_0,\theta)$, as presented in equation (33), we have systematically defined all terms except for $\Psi_m(\boldsymbol{F})$ and $\Psi_{em}(\boldsymbol{F},\boldsymbol{E}_0)$. For these two potentials, we have explored a broad spectrum of models that characterize the constitutive behavior of ideal dielectric elastomers under isothermal conditions. Specifically, for the purely

Mechanical isothermal Helmholtz free energy Ψ_m	
Name of the model	Invariant representation
Mooney-Rivlin (MR)	$\mathbb{U}_\Psi = \frac{\mu_1}{2}\left(I_{\Psi_1}-3\right) + \frac{\mu_2}{2}\left(I_{\Psi_2}-3\right) - \left(\mu_1+2\mu_2\right)\ln\left(I_{\Psi_3}\right) + \frac{\lambda}{2}\left(I_{\Psi_3}-1\right)^2$

Parameter:	$\mu_1/\bar{\mu}$	$\mu_2/\bar{\mu}$	$\lambda/\bar{\mu}$
Value:	0.5	0.5	5

Quadratic MR (QMR)	$\mathbb{U}_\Psi = \frac{\mu_1}{2}\left(I_{\Psi_1}\right)^2 + \frac{\mu_2}{2}\left(I_{\Psi_2}\right)^2 - 6\left(\mu_1+2\mu_2\right)\ln\left(I_{\Psi_3}\right) + \frac{\lambda}{2}\left(I_{\Psi_3}-1\right)^2$

Parameter:	$\mu_1/\bar{\mu}$	$\mu_2/\bar{\mu}$	$\lambda/\bar{\mu}$
Value:	0.5	0.5	5

Gent (G)	$\mathbb{U}_\Psi = -\frac{\mu}{2}J_m \ln\left(1-\frac{I_{\Psi_1}-3}{J_m}\right) - \mu\ln\left(I_{\Psi_3}\right) + \frac{\lambda}{2}\left(I_{\Psi_3}-1\right)^2$

Parameter:	$\mu/\bar{\mu}$	J_m	$\lambda/\bar{\mu}$
Value:	1	19	5

Yeoh (Y)	$\mathbb{U}_\Psi = C_{10}\left(I_{\Psi_1}-3\right) + C_{20}\left(I_{\Psi_1}-3\right)^2 + C_{30}\left(I_{\Psi_1}-3\right)^3$ $-2C_{10}\ln\left(I_{\Psi_3}\right) + \frac{\lambda}{2}\left(I_{\Psi_3}-1\right)^2$

Parameter:	$C_{10}/\bar{\mu}$	$C_{20}/\bar{\mu}$	$C_{30}/\bar{\mu}$	$\lambda/\bar{\mu}$
Value:	1	1	1	5

Trans. Isotropy (TI)	$\mathbb{U}_\Psi = \frac{\mu_1}{2}\left(I_{\Psi_1}-3\right) + \frac{\mu_2}{2}\left(I_{\Psi_2}-3\right) - \left(\mu_1+2\mu_2+\mu_3\right)\ln\left(I_{\Psi_3}\right)$ $+\frac{\lambda}{2}\left(I_{\Psi_3}-1\right)^2 + \frac{\mu_3}{2\alpha}\Big(\left(I_{\Psi_6}\right)^\alpha - 1\Big) + \frac{\mu_3}{2\beta}\Big(\left(I_{\Psi_7}\right)^\beta - 1\Big)$

Parameter:	$\mu_1/\bar{\mu}$	$\mu_2/\bar{\mu}$	$\mu_3/\bar{\mu}$	λ	α	β	$\boldsymbol{N}$
Value:	0.5	0.5	7.5	5	2	2	$\frac{1}{\sqrt{3}}\begin{bmatrix}1 & 1 & 1\end{bmatrix}^T$

Table 1: The various models used for the isothermal mechanical contribution $\Psi_m(\boldsymbol{F})$ in (33). We have considered $\bar{\mu} = 10^5$ (Pa).

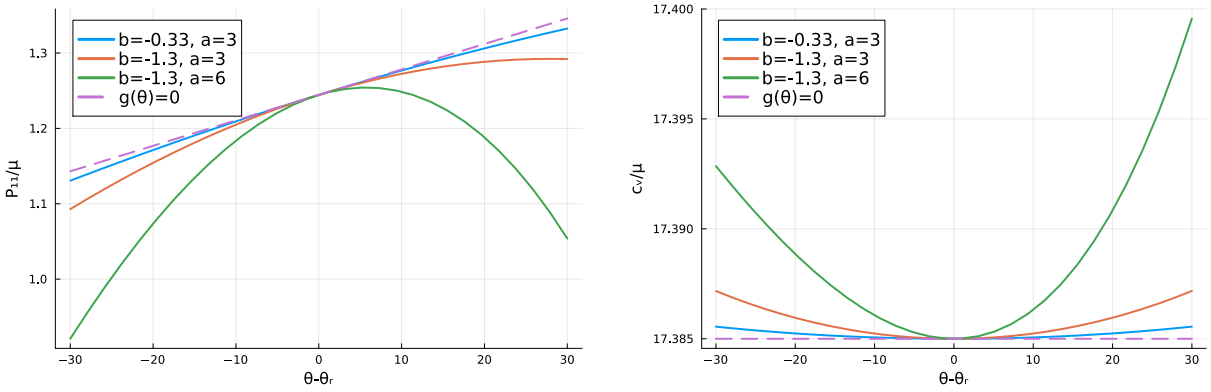

(a) (b)

Figure 3: a) Nonlinear behaviour of stress (component 11 of $\boldsymbol{P}$) with respect to temperature; b) Nonlinear behaviour of c_v with respect to θ. In both cases $\boldsymbol{F}$ and $\boldsymbol{E}_0$ have been fixed to the values given in (38) where the purely mechanical and electro-mechanical isothermal potential, Ψ_m and Ψ_{em} correspond with a Mooney-Rivlin model and an ideal dielectric elastomer model, respectively.

mechanical contribution $\Psi_m(\boldsymbol{F})$, we have examined various hyperelastic potentials listed in Table 1, which include: Mooney-Rivlin model; Quadratic Mooney-Rivlin model; Gent model; Yeoh model; Hyperelastic potentials for transverse isotropy. Table 1 presents the values of the material parameters employed in defining each of the aforementioned models.

With regards to the electro-mechanical contribution $\Psi_{em}(\boldsymbol{F}, \boldsymbol{E}_0)$, we have considered: Ideal dielectric elastomer; Model with electric saturation, employed by some authors to account for the saturation effects associated with hard inclusions that exhibit electric saturation. Both models and the material parameters used in their definition can be seen in Table 2.

Electro-mechanical isothermal Helmholtz free energy Ψ_{em}	
Name of the model	Invariant representation
Ideal dielectric (ID)	$\mathbb{U}_\Psi = -\frac{1}{2\varepsilon}\frac{I_{\Psi_5}}{I_{\Psi_3}}$
Parameter: ε	
Value: 1	
Electric Saturation (ES)	$\mathbb{U}_\Psi = -\frac{D_s^2}{\varepsilon I_{\Psi_3}} \log\left(\cosh\left(\frac{\varepsilon (I_{\Psi_5})^{1/2}}{D_s}\right)\right)$
Parameter: D_s	ε
Value: $0.6\sqrt{\bar{\mu}\bar{\varepsilon}}$	1

Table 2: The two models used for the isothermal electro-mechanical contribution $\Psi_{em}(\boldsymbol{F}, \boldsymbol{E}_0)$ in (33). We have considered $\bar{\varepsilon} = 4\varepsilon_0$, with $\varepsilon_0 = 8.85 \times 10^{-12}$ (F/m).

4. Physics-augmented neural networks constitutive models

In the preceding section, we introduced the general form of the analytical Helmholtz free energy density, which serves as the foundation for generating in-silico data in this section. The primary goal here is to generate such data with Helmholtz free energy densities that are decomposed as per equation (33), depending on $\boldsymbol{F}, \boldsymbol{E}_0, \theta$. This approach aims to facilitate the construction of neural network surrogates with the capability to depend on the sets $\{\boldsymbol{F}, \boldsymbol{E}_0, \theta\}$, $\{\boldsymbol{F}, \boldsymbol{D}_0, \eta\}$, $\{\boldsymbol{F}, \boldsymbol{D}_0, \theta\}$, or $\{\boldsymbol{F}, \boldsymbol{E}_0, \eta\}$, as outlined in Section 3.2. These surrogates are consistently denoted as Ψ_{nn}, e_{nn}, Υ_{nn}, or Γ_{nn}, respectively, in alignment with the potentials described in Section 3.2.

Crucially, to ensure compliance with fundamental physical principles, such as material frame indifference and material symmetry, we follow an invariant formulation for these potentials, as detailed in Section 3.3. All of this is mathematically encapsulated in equation (42), i.e

Ground truth model in equation (33)	Family of data-driven neural network thermodynamical potentials
$\Psi(\boldsymbol{F}, \boldsymbol{E}_0, \theta)$	$\begin{cases} \Psi_{nn}(\boldsymbol{F}, \boldsymbol{E}_0, \theta, \boldsymbol{\mathcal{W}}) = \mathbb{U}_{\Psi\, nn}\left(I_{\Psi_1}, \ldots, I_{\Psi_{n_{\text{inv}}}}, \theta\right) \\ e_{nn}(\boldsymbol{F}, \boldsymbol{D}_0, \eta, \boldsymbol{\mathcal{W}}) = \mathbb{U}_{e\, nn}\left(I_{e_1}, \ldots, I_{e_{n_{\text{inv}}}}, \eta\right) \\ \Upsilon_{nn}(\boldsymbol{F}, \boldsymbol{D}_0, \theta, \boldsymbol{\mathcal{W}}) = \mathbb{U}_{\Upsilon\, nn}\left(I_{\Upsilon_1}, \ldots, I_{\Upsilon_{n_{\text{inv}}}}, \theta\right) \\ \Gamma_{nn}(\boldsymbol{F}, \boldsymbol{E}_0, \eta, \boldsymbol{\mathcal{W}}) = \mathbb{U}_{\Gamma\, nn}\left(I_{\Gamma_1}, \ldots, I_{\Gamma_{n_{\text{inv}}}}, \eta\right) \end{cases}$

(42)

In equation (42), $\boldsymbol{\mathcal{W}}$ represents the parameters of the neural network, which encompass

$$\boldsymbol{\mathcal{W}} = \left\{\boldsymbol{W}_1, \ldots, \boldsymbol{W}_{n_{L+1}}, \boldsymbol{b}_1, \ldots, \boldsymbol{b}_{n_{L+1}}\right\}, \tag{43}$$

where $\boldsymbol{W}_i$ and $\boldsymbol{b}_i$ represent the weights and biases associated with layer i. As standard in neural networks, for an architecture with n_L hidden layers, the inputs $\boldsymbol{A}_h$ of layer h is obtained through the following expression

$$\boldsymbol{A}_h = \sigma_h\left(\boldsymbol{W}_h \boldsymbol{A}_{h-1} + \boldsymbol{b}_h\right); \qquad h = \{1, \ldots, n_{L+1}\}, \tag{44}$$

where

$$\boldsymbol{W}_h \in \mathbb{R}^{n_h \times n_{h-1}}; \qquad \boldsymbol{b}_h \in \mathbb{R}^{n_h}, \tag{45}$$

with

$$n_0 = n_{\text{inv}} + 1; \qquad n_{L+1} = 1, \tag{46}$$

where $n_{\text{inv}} = 6$ or $n_{\text{inv}} = 9$ for isotropy or transverse isotropy, respectively (see Sections 3.3.1 and 3.3.2). Furthermore, the vectors $\boldsymbol{A}_h$, for $h = n_L + 1$ represents the predicted neural network model whereas for $h = 0$, it represents the input of the model, namely

$$\begin{aligned}
\boldsymbol{A}_{n_L+1} &= \Psi_{nn}(\boldsymbol{F}, \boldsymbol{E}_0, \theta, \boldsymbol{\mathcal{W}}); & \boldsymbol{A}_0 &= \begin{bmatrix} I_{\Psi_1} & I_{\Psi_2} & \ldots & I_{\Psi_n} & \theta \end{bmatrix}; \\
\boldsymbol{A}_{n_L+1} &= e_{nn}(\boldsymbol{F}, \boldsymbol{D}_0, \eta, \boldsymbol{\mathcal{W}}); & \boldsymbol{A}_0 &= \begin{bmatrix} I_{e_1} & I_{e_2} & \ldots & I_{e_n} & \eta \end{bmatrix}; \\
\boldsymbol{A}_{n_L+1} &= \Upsilon_{nn}(\boldsymbol{F}, \boldsymbol{D}_0, \theta, \boldsymbol{\mathcal{W}}); & \boldsymbol{A}_0 &= \begin{bmatrix} I_{\Upsilon_1} & I_{\Upsilon_2} & \ldots & I_{\Upsilon_n} & \theta \end{bmatrix}; \\
\boldsymbol{A}_{n_L+1} &= \Gamma_{nn}(\boldsymbol{F}, \boldsymbol{E}_0, \eta, \boldsymbol{\mathcal{W}}); & \boldsymbol{A}_0 &= \begin{bmatrix} I_{\Gamma_1} & I_{\Gamma_2} & \ldots & I_{\Gamma_n} & \eta \end{bmatrix}.
\end{aligned} \tag{47}$$

Notice that indeed, the fact that $n_L + 1$=1 means is due to the fact that the output of the neural network model is the energy density function, which is a scalar. In addition, σ_h represents the activation function of layer h. In our work we have made use of Softplus activation functions for the hidden layers, whilst for the last (output) layer we have made use of the identity function, namely

$$\sigma_h(x) = \log\left(1 + e^x\right), \; h = \{1, \ldots, n_L\}; \qquad \sigma_{n_{L+1}}(x) = x. \tag{48}$$

4.1. Sobolev-type calibration strategy 1

We have proposed two different calibration strategies that will be described in the forthcoming sections. We begin by describing the fundamental aspects of this strategy.

4.1.1. Fundamental aspects of the strategy

In this approach, four distinct types of neural network models, namely $\Psi_{nn}(\boldsymbol{F}, \boldsymbol{E}_0, \theta, \boldsymbol{\mathcal{W}})$, $e_{nn}(\boldsymbol{F}, \boldsymbol{D}_0, \eta, \boldsymbol{\mathcal{W}})$, $\Upsilon_{nn}(\boldsymbol{F}, \boldsymbol{D}_0, \theta, \boldsymbol{\mathcal{W}})$ or $\Gamma_{nn}(\boldsymbol{F}, \boldsymbol{E}_0, \eta, \boldsymbol{\mathcal{W}})$, are developed with the specific objective of minimising the discrepancy between:

- the derivatives $\{\partial_{\boldsymbol{F}}\Psi_{nn}, -\partial_{\boldsymbol{E}_0}\Psi_{nn}, -\partial_\theta\Psi_{nn}\}$ and $\{\boldsymbol{P}, \boldsymbol{D}_0, \eta\} := \{\partial_{\boldsymbol{F}}\Psi, -\partial_{\boldsymbol{E}_0}\Psi, -\partial_\theta\Psi\}$
- the derivatives $\{\partial_{\boldsymbol{F}}e_{nn}, \partial_{\boldsymbol{D}_0}e_{nn}, \partial_\eta e_{nn}\}$ and $\{\boldsymbol{P}, \boldsymbol{E}_0, \theta\} := \{\partial_{\boldsymbol{F}}\Psi, \boldsymbol{E}_0, \theta\}$
- the derivatives $\{\partial_{\boldsymbol{F}}\Upsilon_{nn}, \partial_{\boldsymbol{D}_0}\Upsilon_{nn}, -\partial_\theta\Upsilon_{nn}\}$ and $\{\boldsymbol{P}, \boldsymbol{E}_0, \eta\} := \{\partial_{\boldsymbol{F}}\Psi, \boldsymbol{E}_0, -\partial_\eta\Psi\}$
- the derivatives $\{\partial_{\boldsymbol{F}}\Gamma_{nn}, -\partial_{\boldsymbol{E}_0}\Gamma_{nn}, \partial_\eta\Gamma_{nn}\}$ and $\{\boldsymbol{P}, \boldsymbol{D}_0, \theta\} := \{\partial_{\boldsymbol{F}}\Psi, -\partial_{\boldsymbol{E}_0}\Psi, \theta\}$

showcasing that, regardless of the neural network surrogate employed, the underlying ground truth model remains a Helmholtz free energy density $\Psi(\boldsymbol{F}, \boldsymbol{E}_0, \theta)$ as formulated in equation (33). This is illustrated schematically in Figure 4. To accomplish this objective, we define the corresponding Sobolev-type loss functions, with their specific expressions provided in Table 3.

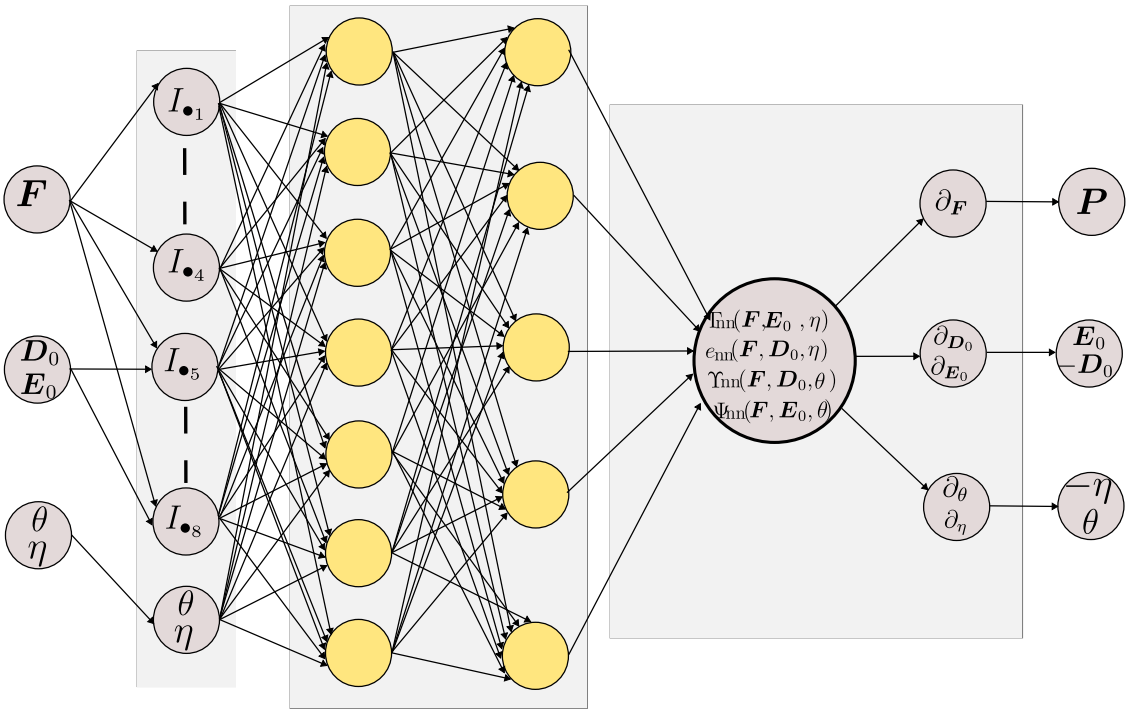

Figure 4: Simplified structure of the neural network architecture used for calibration of the four neural network-based surrogate potentials i.e. Ψ_{nn}, e_{nn}, Υ_{nn} or Γ_{nn}, for the case of Sobolev-type training strategy 1.

4.1.2. Polyconvexity of neural network-based potentials

Sections 3.1 and 3.2 described the desired convexity/convexity conditions that the four possible neural network-based thermodynamical potentials, namely $\Psi(\boldsymbol{F}, \boldsymbol{E}_0, \theta)$, $e\boldsymbol{F}, \boldsymbol{D}_0, \eta)$, $\Upsilon(\boldsymbol{F}, \boldsymbol{D}_0, \theta)$ or $\Gamma(\boldsymbol{F}, \boldsymbol{E}_0, \theta)$ should satisfy. Enforcing simultaneous convexity and concavity across multiple physics, as required for the three potentials $\Psi(\boldsymbol{F}, \boldsymbol{E}_0, \theta)$, $\Upsilon(\boldsymbol{F}, \boldsymbol{D}_0, \theta)$ or $\Gamma(\boldsymbol{F}, \boldsymbol{E}_0, \theta)$, presents a complex challenge. This difficulty arises whether the model is derived from a phenomenological

	$\mathcal{L}(\boldsymbol{\mathcal{W}})$	
Ψ_{nn}	$\beta_1 \frac{\sum_{i=1}^{n_\mathrm{d}} \left\|\partial_{\boldsymbol{F}}\Psi^i - \partial_{\boldsymbol{F}}\Psi_{nn}(\boldsymbol{X}^i,\boldsymbol{\mathcal{W}})\right\|^2}{\sum_{i=1}^{n_\mathrm{d}} \left\|\partial_{\boldsymbol{F}}\Psi^i\right\|^2} + \beta_2 \frac{\sum_{i=1}^{n_\mathrm{d}} \left\|\partial_{\boldsymbol{E}_0}\Psi^i - \partial_{\boldsymbol{E}_0}\Psi_{nn}(\boldsymbol{X}^i,\boldsymbol{\mathcal{W}})\right\|^2}{\sum_{i=1}^{n_\mathrm{d}} \left\|\partial_{\boldsymbol{E}_0}\Psi^i\right\|^2} + \beta_3 \frac{\sum_{i=1}^{n_\mathrm{d}} \left(\partial_\theta\Psi^i - \partial_\theta\Psi_{nn}(\boldsymbol{X}^i,\boldsymbol{\mathcal{W}})\right)^2}{\sum_{i=1}^{n_\mathrm{d}} \left(\partial_\theta\Psi^i\right)^2}$	$\boldsymbol{X}^i = \{\boldsymbol{F}^i, \boldsymbol{E}_0^i, \theta^i\}$
e_{nn}	$\beta_1 \frac{\sum_{i=1}^{n_\mathrm{d}} \left\|\partial_{\boldsymbol{F}}\Psi^i - \partial_{\boldsymbol{F}}e_{nn}(\boldsymbol{X}^i,\boldsymbol{\mathcal{W}})\right\|^2}{\sum_{i=1}^{n_\mathrm{d}} \left\|\partial_{\boldsymbol{F}}\Psi^i\right\|^2} + \beta_2 \frac{\sum_{i=1}^{n_\mathrm{d}} \left\|\boldsymbol{E}_0^i - \partial_{\boldsymbol{D}_0}e_{nn}(\boldsymbol{X}^i,\boldsymbol{\mathcal{W}})\right\|^2}{\sum_{i=1}^{n_\mathrm{d}} \left\|\boldsymbol{E}_0^i\right\|^2} + \beta_3 \frac{\sum_{i=1}^{n_\mathrm{d}} \left(\theta^i - \partial_\eta e_{nn}(\boldsymbol{X}^i,\boldsymbol{\mathcal{W}})\right)^2}{\sum_{i=1}^{n_\mathrm{d}} \left(\theta^i\right)^2}$	$\boldsymbol{X}^i = \{\boldsymbol{F}^i, -\partial_{\boldsymbol{E}_0}\Psi^i, -\partial_\theta\Psi^i\}$
Υ_{nn}	$\frac{\sum_{i=1}^{n_\mathrm{d}} \left\|\partial_{\boldsymbol{F}}\Psi^i - \partial_{\boldsymbol{F}}\Upsilon_{nn}(\boldsymbol{X}^i,\boldsymbol{\mathcal{W}})\right\|^2}{\sum_{i=1}^{n_\mathrm{d}} \left\|\partial_{\boldsymbol{F}}\Psi^i\right\|^2} + \frac{\sum_{i=1}^{n_\mathrm{d}} \left\|\boldsymbol{E}_0^i - \partial_{\boldsymbol{D}_0}\Upsilon_{nn}(\boldsymbol{X}^i,\boldsymbol{\mathcal{W}})\right\|^2}{\sum_{i=1}^{n_\mathrm{d}} \left\|\boldsymbol{E}_0^i\right\|^2} + \frac{\sum_{i=1}^{n_\mathrm{d}} \left(\partial_\theta\Psi^i - \partial_\theta\Upsilon_{nn}(\boldsymbol{X}^i,\boldsymbol{\mathcal{W}})\right)^2}{\sum_{i=1}^{n_\mathrm{d}} \left(\partial_\theta\Psi^i\right)^2}$	$\boldsymbol{X}^i = \{\boldsymbol{F}^i, -\partial_{\boldsymbol{E}_0}\Psi^i, \theta^i\}$
Γ_{nn}	$\frac{\sum_{i=1}^{n_\mathrm{d}} \left\|\partial_{\boldsymbol{F}}\Psi^i - \partial_{\boldsymbol{F}}\Gamma_{nn}(\boldsymbol{X}^i,\boldsymbol{\mathcal{W}})\right\|^2}{\sum_{i=1}^{n_\mathrm{d}} \left\|\partial_{\boldsymbol{F}}\Psi^i\right\|^2} + \frac{\sum_{i=1}^{n_\mathrm{d}} \left\|\partial_{\boldsymbol{E}_0}\Psi^i - \partial_{\boldsymbol{E}_0}\Gamma_{nn}(\boldsymbol{X}^i,\boldsymbol{\mathcal{W}})\right\|^2}{\sum_{i=1}^{n_\mathrm{d}} \left\|\partial_{\boldsymbol{E}_0}\Psi^i\right\|^2} + \frac{\sum_{i=1}^{n_\mathrm{d}} \left(\theta^i - \partial_\eta\Gamma_{nn}(\boldsymbol{X}^i,\boldsymbol{\mathcal{W}})\right)^2}{\sum_{i=1}^{n_\mathrm{d}} \left(\theta^i\right)^2}$	$\boldsymbol{X}^i = \{\boldsymbol{F}^i, \boldsymbol{E}_0^i, -\partial_\theta\Psi^i\}$

Table 3: Loss functions $\mathcal{L}(\boldsymbol{\mathcal{W}})$ used for the calibration of the various type of neural network-based surrogate potentials, i.e. Ψ_{nn}, e_{nn}, Υ_{nn} or Γ_{nn}, for the case of Sobolev-type training strategy 1. All the potentials have been calibrated with data obtained from Helmholtz free energy density ground truth models, i.e. Ψ. The index i represents in-silico data number i, and n_d the number of data used for calibration.

explicit representation or constructuted using neural network frameworks. However, the direct imposition of convexity exclusively, or more specifically, polyconvexity in the sense of equation (24), proves to be more tractable. Building on the work of [40] and extending it from electro-mechanics to the thermo-electro-mechanical context, a sufficient condition to ensure polyconvexity of the neural network-based potential $e_{nn}(\boldsymbol{F}, \boldsymbol{D}_0, \eta)$ is, provided that the invariants $\{I_{e_1}, \ldots, I_{e_{n_{inv}}}\}$ are polyconvex (invariants in equations (30) and (32) are indeed polyconvex), the positiveness of the weights $\boldsymbol{W}_h$ and the monotonically increasing nature of the activation functions, namely

$$(\boldsymbol{W}_h)_{ij} > 0; \qquad \sigma_h'(x) > 0, \forall x; \qquad h = \{1, \ldots, n_{L+1}\}\,. \tag{49}$$

Notice that the first condition can be imposed as a penalty term in the objective function, leading to the augmented objective function $\widetilde{\mathcal{L}}(\boldsymbol{\mathcal{W}})$ defined as

$$\widetilde{\mathcal{L}}(\boldsymbol{\mathcal{W}}) = \mathcal{L}(\boldsymbol{\mathcal{W}}) + \frac{\kappa}{2} \sum_i \left(\min\left((\boldsymbol{\mathcal{W}}_v)_i, 0 \right) \right)^2. \tag{50}$$

where $\mathcal{L}(\boldsymbol{\mathcal{W}})$ is defined as in Table 3, $\boldsymbol{\mathcal{W}}_v$ represents the concatenation of all vectorized weights $\boldsymbol{\mathcal{W}}_h$, $h = \{1, \ldots, n_{L+1}\}$, and κ, the penalty parameter. Furthermore, notice that increasing monotonicity is satisfied by the activation functions chosen in equation (48). In this work, we will explore the accuracy of neural network-based $e_{nn}(\boldsymbol{F}, \boldsymbol{D}_0, \eta)$ potentials with and without the additional penalty term enforcing the polyconvexity condition. This will be futher discussed in Section 6.1.4.

Remark 1. It is important to emphasize that the main scope of this paper is not on enforcing polyconvexity. However, just as a demonstration, we have explored how our framework can realize polyconvexity just for one of the four potentials, specifically the one depending upon $\{\boldsymbol{F}, \boldsymbol{D}_0, \eta\}$, specially convenient for the imposition of polyconvexity across the three physics involved.

Notice however that other authors [28] have explored (in the field of thermo-elasticity) how, through careful design the neural network, mixed convexity (for the mechanical field) and concavity conditions (for the thermal field, i.e. θ) can *a priori* be imposed.

4.2. Sobolev-type calibration strategy 2

The calibration approach outlined in Section 4.1, referred to as calibration strategy 1, is characterised by its remarkable flexibility—enabling the calibration of four distinct types of thermodynamic potentials—and its robustness, as demonstrated in the numerical examples section. However, this approach can be subject to criticism when applied to scenarios involving data generated in real-world conditions, as opposed to an in-silico process. While calibration strategy 1 is well-suited for data generated in-silico, as is the case in this study, its applicability may be severely limited when dealing with laboratory-derived data. The primary challenge arises from the requirement for data across six quantities: $\{\boldsymbol{F}, \boldsymbol{E}_0, \theta, \boldsymbol{P}, \boldsymbol{D}_0, \eta\}$. Of these, entropy ($\eta$) cannot be directly measured in a laboratory setting, which significantly impairs the feasibility of this calibration strategy in practical, real-world scenarios.

To address this limitation, we have developed an alternative strategy that can be applied to both in-silico and experimentally generated data. The key aspect of this approach lies in substituting the only non-measurable field within $\{\boldsymbol{F}, \boldsymbol{E}_0, \theta, \boldsymbol{P}, \boldsymbol{D}_0, \eta\}$, namely η, with other thermophysical properties that can be directly measured in a laboratory setting. This modification enhances the versatility of the calibration process, making it applicable to real-world experimental data as well as computationally generated scenarios. A suitable physical property to replace η is the specific heat capacity c_v (see equation (16)).

As discussed in Section 3.4, specifically for the generic Helmholtz free energy density considered in this study, c_v may exhibit a nonlinear dependence on the fields $\{\boldsymbol{F}, \boldsymbol{E}_0, \theta\}$. Therefore, we could consider incorporating data values for c_v at a set of points $\mathcal{G}_{c_v} = \{\boldsymbol{X}^1, \dots, \boldsymbol{X}^{n_{c_v}}\}$, which includes the reference configuration $\boldsymbol{X}^1 = \{\boldsymbol{I}, \boldsymbol{0}, \theta_R\}$ as well as other possible scenarios $\boldsymbol{X}^i = \{\boldsymbol{F}^i, \boldsymbol{E}_0^i, \theta^i\}$, with n_{c_v} the number of data points within the set $\mathcal{G}_{c_v}$. However, the available experimental data for c_v, is typically limited to the reference configuration. To better align with conditions more reflective of the experimental setup, we choose to include only the specific heat capacity c_v data corresponding to the reference configuration, i.e., $\mathcal{G}_{c_v} = \boldsymbol{X}^1$. Additionally, while entropy η cannot be directly measured, it is known to vanish in the reference configuration (see equation (14)). Thus, this condition can also be incorporated into the calibration strategy.

Notice that this new approach introduces notable differences in the calibration of the potentials that do depend on θ (i.e $\Psi_{nn}(\boldsymbol{F}, \boldsymbol{E}_0, \theta)$ and $\Upsilon_{nn}(\boldsymbol{F}, \boldsymbol{D}_0, \theta)$) and those which depend on η (i.e $e_{nn}(\boldsymbol{F}, \boldsymbol{D}_0, \eta)$ and $\Gamma_{nn}(\boldsymbol{F}, \boldsymbol{E}_0, \eta)$). The main difference resides in the fact that temperature is data which can be measured and therefore, is available in the calibration (for $\Psi_{nn}(\boldsymbol{F}, \boldsymbol{E}_0, \theta)$ and $\Upsilon_{nn}(\boldsymbol{F}, \boldsymbol{D}_0, \theta)$). However, we assume in this approach that the entropy η is not measurable and therefore, not readily available. Consequently, the potentials $e_{nn}(\boldsymbol{F}, \boldsymbol{D}_0, \eta)$ and $\Gamma_{nn}(\boldsymbol{F}, \boldsymbol{E}_0, \eta)$ must be calibrated in the absence of any information or data regarding the third argument, η. This inherent limitation necessitates a distinct treatment for the calibration strategy, differentiating between those potentials that depend on θ (namely, $\Psi_{nn}(\boldsymbol{F}, \boldsymbol{E}_0, \theta)$ and $\Upsilon_{nn}(\boldsymbol{F}, \boldsymbol{D}_0, \theta)$) and those that depend on η ($e_{nn}(\boldsymbol{F}, \boldsymbol{D}_0, \eta)$ and $\Gamma_{nn}(\boldsymbol{F}, \boldsymbol{E}_0, \eta)$).

4.2.1. Mathematical formulation of the strategy: potentials depending upon θ

For the temperature dependent potentials, i.e. $\Psi_{nn}(\boldsymbol{F}, \boldsymbol{E}_0, \theta, \boldsymbol{\mathcal{W}})$ and $\Upsilon_{nn}(\boldsymbol{F}, \boldsymbol{D}_0, \theta, \boldsymbol{\mathcal{W}})$, this alternative and more physically oriented calibration approach, the specific objective is to minimise the discrepancy between:

- Ψ_{nn}
  - the derivatives $\{\partial_{\boldsymbol{F}}\Psi_{nn}, -\partial_{\boldsymbol{E}_0}\Psi_{nn}\}$ and $\{\boldsymbol{P}, \boldsymbol{D}_0\} := \{\partial_{\boldsymbol{F}}\Psi, -\partial_{\boldsymbol{E}_0}\Psi\}$
  - the fields $\{-\theta\partial^2_{\theta\theta}\Psi_{nn}, -\partial_\theta\Psi_{nn}|_{\boldsymbol{I},\boldsymbol{0},\theta_R}\}$ and $\{c_v, \eta|_{\boldsymbol{I},\boldsymbol{0},\theta_R}\} := \{-\theta\partial^2_{\theta\theta}\Psi, -\partial_\theta\Psi|_{\boldsymbol{I},\boldsymbol{0},\theta_R}\}$
  - $\{\boldsymbol{F}, \boldsymbol{E}_0, \theta\}$ are data
- Υ_{nn}
  - the derivatives $\{\partial_{\boldsymbol{F}}\Upsilon_{nn}, \partial_{\boldsymbol{D}_0}\Upsilon_{nn}\}$ and $\{\boldsymbol{P}, \boldsymbol{E}_0\} := \{\partial_{\boldsymbol{F}}\Psi, \boldsymbol{E}_0\}$
  - the fields $\{-\theta\partial^2_{\theta\theta}\Upsilon_{nn}, -\partial_\theta\Upsilon_{nn}|_{\boldsymbol{I},\boldsymbol{0},\theta_R}\}$ and $\{c_v, \eta|_{\boldsymbol{I},\boldsymbol{0},\theta_R}\} := \{-\theta\partial^2_{\theta\theta}\Psi, -\partial_\theta\Psi|_{\boldsymbol{I},\boldsymbol{0},\theta_R}\}$
  - $\{\boldsymbol{F}, \boldsymbol{D}_0, \theta\}$ are data

This is illustrated schematically in Figure 5. Notice that, unlike in the preceeding calibration strategy, the unavailability of η prevents in to minimise the difference between θ and the derivatives of the two potentials with respect to θ, namely $-\partial_\theta \Psi_{nn}$ and $-\partial_\theta \Upsilon_{nn}$. Instead, we have incorporated c_v and $\partial_\theta \Psi_{nn}|_{\boldsymbol{I},\boldsymbol{0},\theta_R}$ (or $\partial_\theta \Upsilon_{nn}|_{\boldsymbol{I},\boldsymbol{0},\theta_R}$) in the minimisation problem. This is reflected in the loss function observed in Table 4.

	$\mathcal{L}(\boldsymbol{\mathcal{W}})$	
Ψ_{nn}	$\beta_1 \frac{\sum_{i=1}^{n_\mathrm{d}} \lvert\lvert \partial_{\boldsymbol{F}} \Psi^i - \partial_{\boldsymbol{F}} \Psi_{nn}(\boldsymbol{X}^i, \boldsymbol{\mathcal{W}}) \rvert\rvert^2}{\sum_{i=1}^{n_\mathrm{d}} \lvert\lvert \partial_{\boldsymbol{F}} \Psi^i \rvert\rvert^2} + \beta_2 \frac{\sum_{i=1}^{n_\mathrm{d}} \lvert\lvert \partial_{\boldsymbol{E}_0} \Psi^i - \partial_{\boldsymbol{E}_0} \Psi_{nn}(\boldsymbol{X}^i, \boldsymbol{\mathcal{W}}) \rvert\rvert^2}{\sum_{i=1}^{n_\mathrm{d}} \lvert\lvert \partial_{\boldsymbol{E}_0} \Psi^i \rvert\rvert}$ $+ \beta_3 \frac{\sum_{i=1}^{n_{c_v}} \left(\theta^i \partial^2_{\theta\theta} \Psi^i - \theta \partial^2_{\theta\theta} \Psi_{nn}(\boldsymbol{X}^i, \boldsymbol{\mathcal{W}}) \right)^2}{\sum_{i=1}^{n_\mathrm{d}} \left(\theta^i \partial^2_{\theta\theta} \Psi^i \right)^2} + \beta_4 \left(\partial_\theta \Psi_{nn}(\boldsymbol{X}^1, \boldsymbol{\mathcal{W}}) \big|_{\boldsymbol{I},\boldsymbol{0},\theta_R} \right)^2$	$\boldsymbol{X}^i = \{\boldsymbol{F}^i, \boldsymbol{E}_0^i, \theta^i\}$
Υ_{nn}	$\beta_1 \frac{\sum_{i=1}^{n_\mathrm{d}} \lvert\lvert \partial_{\boldsymbol{F}} \Psi^i - \partial_{\boldsymbol{F}} \Upsilon_{nn}(\boldsymbol{X}^i, \boldsymbol{\mathcal{W}}) \rvert\rvert^2}{\sum_{i=1}^{n_\mathrm{d}} \lvert\lvert \partial_{\boldsymbol{F}} \Psi^i \rvert\rvert^2} + \beta_2 \frac{\sum_{i=1}^{n_\mathrm{d}} \lvert\lvert \boldsymbol{E}_0^i - \partial_{\boldsymbol{D}_0} \Upsilon_{nn}(\boldsymbol{X}^i, \boldsymbol{\mathcal{W}}) \rvert\rvert^2}{\sum_{i=1}^{n_\mathrm{d}} \lvert\lvert \boldsymbol{E}_0^i \rvert\rvert^2}$ $+ \beta_3 \frac{\sum_{i=1}^{n_{c_v}} \left(\theta^i \partial^2_{\theta\theta} \Psi^i - \theta \partial^2_{\theta\theta} \Upsilon_{nn}(\boldsymbol{X}^i, \boldsymbol{\mathcal{W}}) \right)^2}{\sum_{i=1}^{n_\mathrm{d}} \left(\theta^i \partial^2_{\theta\theta} \Psi^i \right)^2} + \beta_4 \left(\partial_\theta \Upsilon_{nn}(\boldsymbol{X}^1, \boldsymbol{\mathcal{W}}) \big|_{\boldsymbol{I},\boldsymbol{0},\theta_R} \right)^2$	$\boldsymbol{X}^i = \{\boldsymbol{F}^i, -\partial_{\boldsymbol{E}_0} \Psi^i, \theta^i\}$

Table 4: Loss functions $\mathcal{L}(\boldsymbol{\mathcal{W}})$ used for the calibration of θ-based neural network-based surrogate potentials, i.e. Ψ_{nn}, Υ_{nn}, for the case of Sobolev-type training strategy 2 described in Section 4.2.1. All the potentials have been calibrated with data obtained from Helmholtz free energy density ground truth models, i.e. Ψ. The index i represents in-silico data number i, and n_d the number of data used for calibration, whereas n_{c_v} represents the number of data used for the measurement/evaluation of c_v.

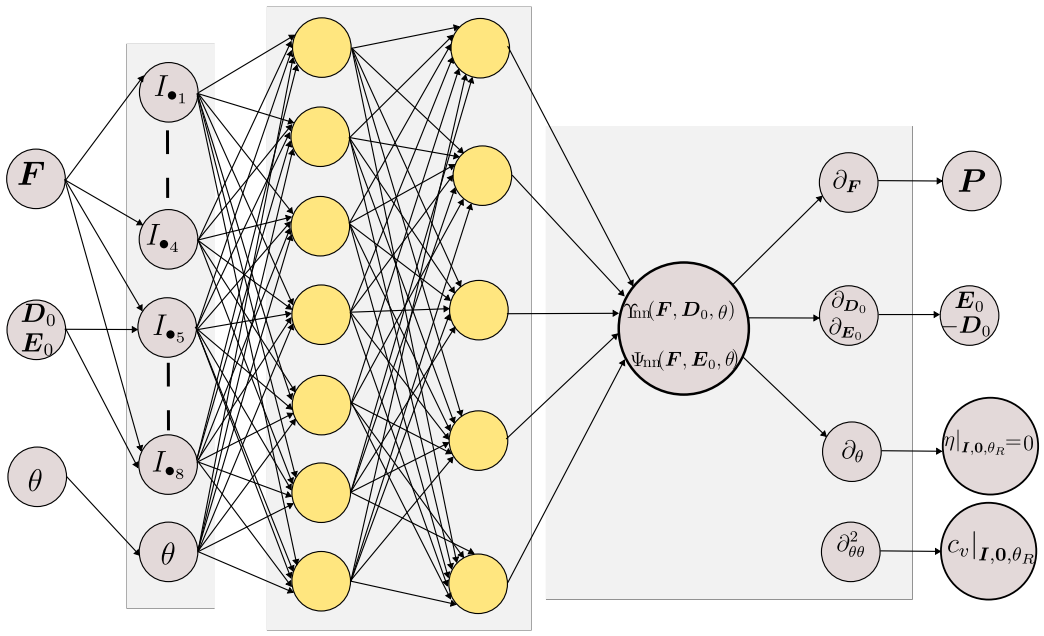

Figure 5: Simplified structure of the neural network architecture used for calibration of the θ-based network-based surrogate potentials i.e. Ψ_{nn}, Υ_{nn}, for the case of Sobolev-type training strategy 2 in Section 4.2.1.

Remark 2. We consider the realistic and common scenario where the heat capacity is only known at the reference state. Despite this apparent limitation, the model can effectively capture the nonlinear dependencies of stress and electric displacement fields on temperature, deformation,

and the electric field. For example, in the context of thermoelasticity (without accounting for electric physics), Reference [28] demonstrates that stresses can be accurately modeled without explicitly incorporating thermal-related fields in the loss function (i.e., $\partial_\theta \Psi$ is excluded during calibration). Consequently, the dependence of stresses on $\boldsymbol{F}$ and $\boldsymbol{\theta}$ is accurately approximated.

After calibration, given $\{\boldsymbol{F}, \boldsymbol{E}_0, \theta\}$, the model should provide precise predictions for $\{\partial_{\boldsymbol{F}} \Psi_{nn}, \partial_{\boldsymbol{E}_0} \Psi_{nn}\}$. However, the thermal dynamics might not be fully captured. For instance, the term $\theta\dot{\eta}$ in the energy conservation equation (see equation (5)) could be inaccurately modeled. Expanding the time derivative $\dot{\eta}$ for a thermodynamic potential $\Psi(\boldsymbol{F}, \boldsymbol{E}_0, \theta)$ gives:

$$\dot{\eta} = -(\dot{\partial_\theta \Psi}) = -\partial^2 \theta \boldsymbol{F} \Psi : \dot{\boldsymbol{F}} - \partial^2 \theta \boldsymbol{E}_0 \Psi \cdot \dot{\boldsymbol{E}} 0 - \partial^2 \theta \theta \Psi : \dot{\theta}. \tag{51}$$

Clearly, accurately modeling the time evolution of $\dot{\eta}$ requires more information than just the heat capacity at the reference state, defined as $c_v|_{\boldsymbol{I},\boldsymbol{0},\theta_R} := -\left(\theta \partial^2_{\theta\theta} \Psi\right)\Big|_{\boldsymbol{I},\boldsymbol{0},\theta_R}$.

4.2.2. Mathematical formulation of the strategy: potentials depending upon η

For the two η-based potentials, specifically $e_{nn}(\boldsymbol{F}, \boldsymbol{D}_0, \eta)$ and $\Gamma_{nn}(\boldsymbol{F}, \boldsymbol{E}_0, \eta)$, the second calibration strategy introduces a distinct differentiation compared to the θ-based potentials discussed in Section 4.2.1. The key distinction lies in the fact that one of the inputs to these potentials, the entropy η, is not directly available from the given data. Instead, what is provided is the temperature, which corresponds to the derivative of both potentials with respect to η. Consequently, η must be determined implicitly through the nonlinear relationships presented in the third column of the first and third rows of equation (19). This relationship can be mathematically reformulated as:

$$\begin{aligned} &\text{Given } \{\boldsymbol{F}, \boldsymbol{D}_0, \theta\}\text{, solve } \eta \text{ from: } \theta = \partial_\eta e_{nn}(\boldsymbol{F}, \boldsymbol{D}_0, \eta); \\ &\text{Given } \{\boldsymbol{F}, \boldsymbol{E}_0, \theta\}\text{, solve } \eta \text{ from: } \theta = \partial_\eta \Gamma_{nn}(\boldsymbol{F}, \boldsymbol{E}_0, \eta). \end{aligned} \tag{52}$$

For these entropy-based dependent potentials, i.e. $e_{nn}(\boldsymbol{F}, \boldsymbol{D}_0, \eta, \boldsymbol{\mathcal{W}})$ and $\Gamma_{nn}(\boldsymbol{F}, \boldsymbol{E}_0, \eta, \boldsymbol{\mathcal{W}})$, this alternative and more physically oriented calibration approach, the specific objective is to satisfy the implicit relationship in (52) whilst minimizing the discrepancy between:

- e_{nn} $\begin{cases} \text{the derivatives } \{\partial_{\boldsymbol{F}} e_{nn}, \partial_{\boldsymbol{D}_0} e_{nn}, \partial_\eta e_{nn}\} \text{ and } \{\boldsymbol{P}, \boldsymbol{E}_0, \theta\} := \{\partial_{\boldsymbol{F}} \Psi, \boldsymbol{E}_0, \theta\} \\ \text{the field } \dfrac{\theta}{\partial^2_{\theta\theta} e} \text{ and } c_v := -\theta \Psi^2_{\theta\theta} \\ \{\boldsymbol{F}, \boldsymbol{D}_0\} \text{ are data} \\ \eta \text{ is not data and it is obtained implicitly from } \theta = \partial_\eta e_{nn}(\boldsymbol{F}, \boldsymbol{D}_0, \eta) \end{cases}$

- Γ_{nn} $\begin{cases} \text{the derivatives } \{\partial_{\boldsymbol{F}} \Gamma_{nn}, -\partial_{\boldsymbol{E}_0} \Gamma_{nn}, \partial_\eta \Gamma_{nn}\} \text{ and } \{\boldsymbol{P}, \boldsymbol{D}_0, \theta\} := \{\partial_{\boldsymbol{F}} \Psi, -\partial_{\boldsymbol{E}_0} \Psi, \theta\} \\ \text{the field } \dfrac{\theta}{\partial^2_{\theta\theta} \Gamma} \text{ and } c_v := -\theta \Psi^2_{\theta\theta} \\ \{\boldsymbol{F}, \boldsymbol{D}_0\} \text{ are data} \\ \eta \text{ is not data and it is obtained implicitly from } \theta = \partial_\eta \Gamma_{nn}(\boldsymbol{F}, \boldsymbol{E}_0, \eta) \end{cases}$

A second distinguishing feature of the second calibration approach applied to η-based potentials again arises from the fact that one of the inputs, specifically η, is not directly available from the data set. In particular, when solving, for example, using a Newton-Raphson numerical scheme to iteratively resolve equation (52), certain convexity and stability conditions must be satisfied to ensure the existence of a solution. These conditions are inherently embedded within equation (21), necessitating the convexity of both potentials e_{nn} and Γ_{nn} with respect to η, namely:

$$\partial^2_{\eta\eta} e_{nn}(\boldsymbol{F}, \boldsymbol{D}_0, \eta) > 0; \qquad \partial^2_{\eta\eta} \Gamma_{nn}(\boldsymbol{F}, \boldsymbol{E}_0, \eta) > 0. \tag{53}$$

We found that the numerical solution of (52) benefits from the imposition of the condition in the reference configuration in equation (20), namely

$$\partial_\eta e(\boldsymbol{F}, \boldsymbol{D}_0, \eta)|_{\boldsymbol{I},\boldsymbol{0},0} = \theta_R; \qquad \partial_\eta \Gamma(\boldsymbol{F}, \boldsymbol{E}_0, \eta)|_{\boldsymbol{I},\boldsymbol{0},0} = \theta_R. \tag{54}$$

To inherently satisfy both conditions (54) and (53) within the neural network-based potentials e_{nn} and Γ_{nn}, we propose the formulation of modified potentials, denoted as $\widetilde{e}_{nn}$ and $\widetilde{\Gamma}_{nn}$.

$$\begin{aligned} \widetilde{e}_{nn}(\boldsymbol{F}, \boldsymbol{D}_0, \eta) &= \underbrace{e_{nn}(\boldsymbol{F}, \boldsymbol{D}_0, \eta)}_{\text{Neural network model}} + \underbrace{\left(\theta_R - \partial_\eta e_{nn}(\boldsymbol{F}, \boldsymbol{D}_0, \eta)|_{\boldsymbol{I},\boldsymbol{0},0}\right)\eta}_{\text{Condition enforcement in reference conf.}} + \underbrace{\alpha_{\text{stb}} \frac{\theta_R}{2c_{vR}} \eta^2}_{\text{Stabilizing term}}; \\ \widetilde{\Gamma}_{nn}(\boldsymbol{F}, \boldsymbol{E}_0, \eta) &= \underbrace{\Gamma_{nn}(\boldsymbol{F}, \boldsymbol{E}_0, \eta)}_{\text{Neural network model}} + \underbrace{\left(\theta_R - \partial_\eta \Gamma_{nn}(\boldsymbol{F}, \boldsymbol{D}_0, \eta)|_{\boldsymbol{I},\boldsymbol{0},0}\right)\eta}_{\text{Condition enforcement in reference conf.}} + \underbrace{\alpha_{\text{stb}} \frac{\theta_R}{2c_{vR}} \eta^2}_{\text{Stabilizing term}}. \end{aligned} \tag{55}$$

In fact, evaluation of the first and second derivative with respect to η for both modified potentials in (55) yields

$$\partial_\eta \Rightarrow \begin{cases} \partial_\eta \widetilde{e}_{nn}(\boldsymbol{F}, \boldsymbol{D}_0, \eta) = \partial_\eta e_{nn}(\boldsymbol{F}, \boldsymbol{D}_0, \eta) + \theta_R - \partial_\eta e_{nn}(\boldsymbol{F}, \boldsymbol{D}_0, \eta)|_{\boldsymbol{I},\boldsymbol{0},0} + \alpha_{\text{stb}} \dfrac{\theta_R}{c_{vR}} \eta; \\ \partial_\eta \widetilde{\Gamma}_{nn}(\boldsymbol{F}, \boldsymbol{E}_0, \eta) = \partial_\eta \Gamma_{nn}(\boldsymbol{F}, \boldsymbol{E}_0, \eta) + \theta_R - \partial_\eta \Gamma_{nn}(\boldsymbol{F}, \boldsymbol{E}_0, \eta)|_{\boldsymbol{I},\boldsymbol{0},0} + \alpha_{\text{stb}} \dfrac{\theta_R}{c_{vR}} \eta; \end{cases}$$

$$\partial^2_{\eta\eta} \Rightarrow \begin{cases} \partial^2_{\eta\eta} \widetilde{e}_{nn}(\boldsymbol{F}, \boldsymbol{D}_0, \eta) = \partial^2_{\eta\eta} e_{nn}(\boldsymbol{F}, \boldsymbol{D}_0, \eta) + \underbrace{\alpha_{\text{stb}} \dfrac{\theta_R}{c_{vR}}}_{>0}; \\ \partial^2_{\eta\eta} \widetilde{\Gamma}_{nn}(\boldsymbol{F}, \boldsymbol{E}_0, \eta) = \partial^2_{\eta\eta} \Gamma_{nn}(\boldsymbol{F}, \boldsymbol{E}_0, \eta) + \underbrace{\alpha_{\text{stb}} \dfrac{\theta_R}{c_{vR}}}_{>0}. \end{cases} \tag{56}$$

Clearly, evaluation of the first derivative in (56) in the reference configuration for both potentials leads to the satisfaction of the condition in equation (54), namely

$$\begin{aligned} \partial_\eta \widetilde{e}_{nn}(\boldsymbol{F}, \boldsymbol{D}_0, \eta)|_{\boldsymbol{I},\boldsymbol{0},0} &= \partial_\eta e_{nn}(\boldsymbol{F}, \boldsymbol{D}_0, \eta)|_{\boldsymbol{I},\boldsymbol{0},0} + \theta_R - \partial_\eta e_{nn}(\boldsymbol{F}, \boldsymbol{D}_0, \eta)|_{\boldsymbol{I},\boldsymbol{0},0} = \theta_R; \\ \partial_\eta \widetilde{\Gamma}_{nn}(\boldsymbol{F}, \boldsymbol{E}_0, \eta)\Big|_{\boldsymbol{I},\boldsymbol{0},0} &= \partial_\eta \Gamma_{nn}(\boldsymbol{F}, \boldsymbol{E}_0, \eta)|_{\boldsymbol{I},\boldsymbol{0},0} + \theta_R - \partial_\eta \Gamma_{nn}(\boldsymbol{F}, \boldsymbol{E}_0, \eta)|_{\boldsymbol{I},\boldsymbol{0},0} = \theta_R. \end{aligned} \tag{57}$$

To examine the second derivative in (56), it becomes evident that whilst the second term is positive, there is no guarantee that the overall derivative, specifically $\partial^2_{\eta\eta} \widetilde{e}_{nn}(\boldsymbol{F}, \boldsymbol{D}0, \eta)$ and $\partial^2_{\eta\eta} \widetilde{\Gamma}_{nn}(\boldsymbol{F}, \boldsymbol{E}0, \eta)$, will be positive. The positivity of these derivatives is contingent upon the chosen value of the stabilizing parameter α_{stb}. Based on our empirical observations, we have determined that setting $\alpha_{\text{stb}} = 0.25$ suffices to prevent numerical instabilities during the solution of equation (52).

The calibration method for the η-based potentials outlined above is depicted schematically in Figure 6. To achieve the primary goal of this calibration approach, we define the associated Sobolev-type loss functions, with their specific formulations detailed in Table 5.

4.2.3. In-silico data generation strategy

In this section, we briefly described the procedure used for generating synthetic data for both calibration strategies, summarised in Algorithm 1. The generation of deformation gradient tensors (step 1 in Algorithm 1) and electric fields $\boldsymbol{E}_0$ or electric displacement fields $\boldsymbol{D}_0$ (step 2 in Algorithm 1) is entirely the same as for strategy 1 in Algorithm 1. The steps followed in the data generation procedure for both calibration strategies is summarised below:

Data generation strategy 1:

- For θ-based potentials, i.e. $\Psi_{nn}(\boldsymbol{F}, \boldsymbol{E}_0, \theta)$ or $\Upsilon_{nn}(\boldsymbol{F}, \boldsymbol{D}_0, \theta)$, fields $\{\boldsymbol{F}, \boldsymbol{E}_0, \theta\}$ or $\{\boldsymbol{F}, \boldsymbol{D}_0, \theta\}$, respectively, are generated as input data according to Algorithm 1. Evaluation of the model permits then to synthetically generate the work conjugate fields $\{\boldsymbol{P}, \boldsymbol{D}_0, \eta\}$ or $\{\boldsymbol{P}, \boldsymbol{E}_0, \eta\}$, respectively, as output variables.

- For η-based potentials, i.e. $e(\boldsymbol{F}, \boldsymbol{D}_0, \eta)$ and $\Gamma(\boldsymbol{F}, \boldsymbol{E}_0, \eta)$, the process is the opposite: $\{\boldsymbol{F}, \boldsymbol{D}_0, \eta\}$ or $\{\boldsymbol{F}, \boldsymbol{E}_0, \eta\}$, respectively, are generated as input data according to Algorithm 1. Evaluation of the model permits then to synthetically generate the work conjugate fields $\{\boldsymbol{P}, \boldsymbol{E}_0, \theta\}$ or $\{\boldsymbol{P}, \boldsymbol{D}_0, \theta\}$, respectively, as output variables.

Data generation strategy 2:

	$\mathcal{L}(\boldsymbol{\mathcal{W}})$	
e_{nn}	$\beta_1 \frac{\sum_{i=1}^{n_\mathrm{d}} \lvert\lvert \partial_{\boldsymbol{F}} \Psi^i - \partial_{\boldsymbol{F}} e_{nn}(\boldsymbol{X}^i, \boldsymbol{\mathcal{W}}) \rvert\rvert^2}{\sum_{i=1}^{n_\mathrm{d}} \lvert\lvert \partial_{\boldsymbol{F}} \Psi^i \rvert\rvert^2} + \beta_2 \frac{\sum_{i=1}^{n_\mathrm{d}} \lvert\lvert \boldsymbol{E}_0^i - \partial_{\boldsymbol{D}_0} e_{nn}(\boldsymbol{X}^i, \boldsymbol{\mathcal{W}}) \rvert\rvert^2}{\sum_{i=1}^{n_\mathrm{d}} \lvert\lvert \boldsymbol{E}_0^i \rvert\rvert^2} + \beta_3 \frac{\sum_{i=1}^{n_\mathrm{d}} \left(\theta^i - \partial_\eta e_{nn}(\boldsymbol{X}^i, \boldsymbol{\mathcal{W}}) \right)^2}{\sum_{i=1}^{n_\mathrm{d}} \left(\theta^i \right)^2}$	$\boldsymbol{X}^i = \{\boldsymbol{F}^i, -\partial_{\boldsymbol{E}_0} \Psi^i, -\partial_\theta \Psi^i\}$
Γ_{nn}	$\beta_1 \frac{\sum_{i=1}^{n_\mathrm{d}} \lvert\lvert \partial_{\boldsymbol{F}} \Psi^i - \partial_{\boldsymbol{F}} \Gamma_{nn}(\boldsymbol{X}^i, \boldsymbol{\mathcal{W}}) \rvert\rvert^2}{\sum_{i=1}^{n_\mathrm{d}} \lvert\lvert \partial_{\boldsymbol{F}} \Psi^i \rvert\rvert^2} + \beta_2 \frac{\sum_{i=1}^{n_\mathrm{d}} \lvert\lvert \partial_{\boldsymbol{E}_0} \Psi^i - \partial_{\boldsymbol{E}_0} \Gamma_{nn}(\boldsymbol{X}^i, \boldsymbol{\mathcal{W}}) \rvert\rvert^2}{\sum_{i=1}^{n_\mathrm{d}} \lvert\lvert \partial_{\boldsymbol{E}_0} \Psi^i \rvert\rvert^2} + \beta_3 \frac{\sum_{i=1}^{n_\mathrm{d}} \left(\theta^i - \partial_\eta \Gamma_{nn}(\boldsymbol{X}^i, \boldsymbol{\mathcal{W}}) \right)^2}{\sum_{i=1}^{n_\mathrm{d}} \left(\theta^i \right)^2}$	$\boldsymbol{X}^i = \{\boldsymbol{F}^i, \boldsymbol{E}_0^i, -\partial_\theta \Psi^i\}$

Table 5: Loss functions $\mathcal{L}(\boldsymbol{\mathcal{W}})$ used for the calibration of η-based neural network-based surrogate potentials, i.e. e_{nn}, Γ_{nn}, for the case of Sobolev-type training strategy 2 described in Section 4.2.2. All the potentials have been calibrated with data obtained from Helmholtz free energy density ground truth models, i.e. Ψ. The index i represents in-silico data number i, and n_d the number of data used for calibration, whereas n_{c_v} represents the number of data used for the measurement/evaluation of c_v.

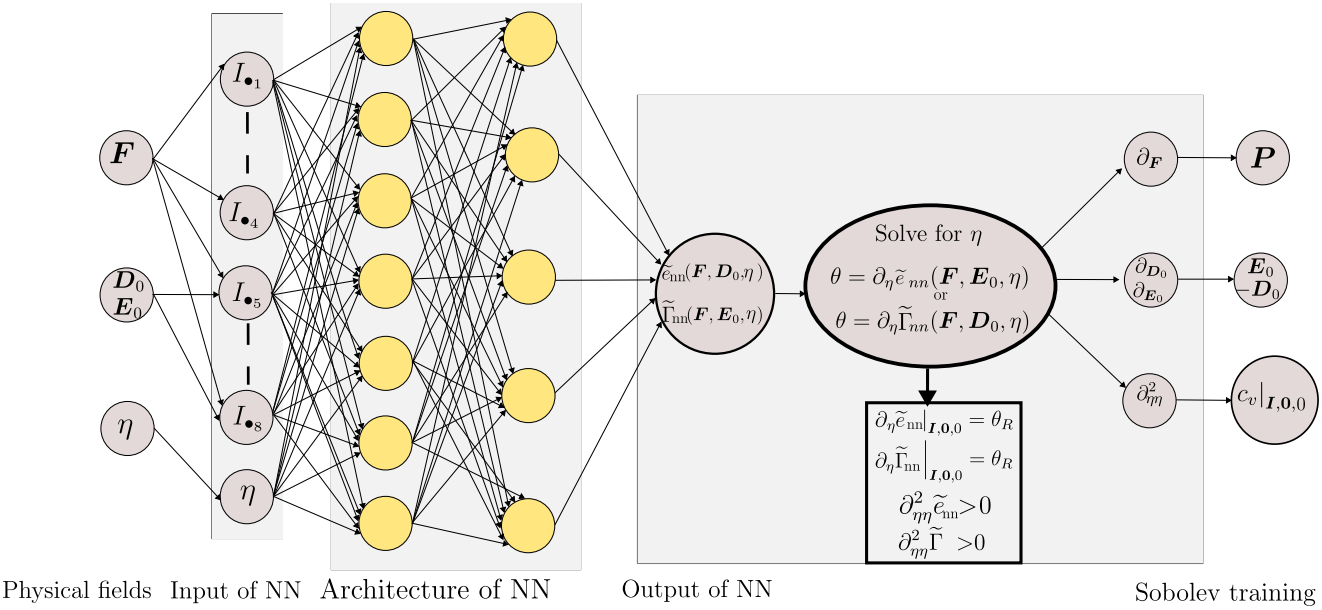

Figure 6: Simplified structure of the neural network architecture used for calibration of the η-based network-based surrogate potentials i.e. e_{nn}, Γ_{nn}, for the case of Sobolev-type training strategy 2 in Section 4.2.2. Enforcement of conditions (53) and (54) is carried out through the modifications in equation (55).

- For θ-based potentials, i.e. $\Psi_{nn}(\boldsymbol{F}, \boldsymbol{E}_0, \theta)$ or $\Upsilon_{nn}(\boldsymbol{F}, \boldsymbol{D}_0, \theta)$, data for fields $\{\boldsymbol{F}, \boldsymbol{E}_0, \theta\}$ or $\{\boldsymbol{F}, \boldsymbol{D}_0, \theta\}$, respectively, are generated as input data according to Algorithm 1. Then, the fields $\{\boldsymbol{P}, \boldsymbol{D}_0\}$ or $\{\boldsymbol{P}, \boldsymbol{E}_0\}$ (generated as synthetic data through direct evaluation of the analytical model or through experiments), respectively, are considered as output variables. The entropy field η is discarded (for synthetic approaches) or directly not available (for experimental procedures). In addition, data for the specific heat capacity c_v is needed (see Section 4.2.1).

- For η-based potentials, i.e. $e(\boldsymbol{F}, \boldsymbol{D}_0, \eta)$ and $\Gamma(\boldsymbol{F}, \boldsymbol{E}_0, \eta)$, data for fields $\{\boldsymbol{F}, \boldsymbol{D}_0, \theta\}$ or $\{\boldsymbol{F}, \boldsymbol{E}_0, \theta\}$, respectively, are generated according to Algorithm 1. Out of the three fields, only two $\{\boldsymbol{F}, \boldsymbol{D}_0\}$ or $\{\boldsymbol{F}, \boldsymbol{E}_0\}$, respectively, are considered to be input variables. The third field, namely θ, is used to solve implicitly the entropy field η according to (52). Then, the fields $\{\boldsymbol{P}, \boldsymbol{D}_0\}$ or $\{\boldsymbol{P}, \boldsymbol{E}_0\}$ (generated as synthetic data through direct evaluation of the analytical model or through experiments), respectively, are considered as output variables in conjunction with θ. In addition, data for the specific heat capacity c_v is needed (see Section 4.2.1).

Table 6 biefly summarizes the main features of both calibration strategies described in Sections 4.1 and 4.2 in terms of their: (i) known inputs; (ii) objective or variables to be predicted; (iii) need to satisfy implicit equations; (iv) applicability to either in-silico or real lab scenarios.

		Calibration Strategy 1	Calibration Strategy 2
Known input	θ-based	$\{\boldsymbol{F}, \bullet, \theta\}$	$\{\boldsymbol{F}, \bullet, \theta\}$
	η-based	$\{\boldsymbol{F}, \bullet, \eta\}$	$\{\boldsymbol{F}, \bullet\}$, η unknown
Objective/prediction	θ-based	$\{\partial_{\boldsymbol{F}}\psi, \partial_{\bullet}\psi, \partial_{\theta}\psi\}$	$\{\partial_{\boldsymbol{F}}\psi, \partial_{\bullet}\psi, c_v\vert_{\boldsymbol{I},\boldsymbol{0},\theta_R}\}$
	η-based	$\{\partial_{\boldsymbol{F}}\psi, \partial_{\bullet}\psi, \partial_{\eta}\psi\}$	$\{\partial_{\boldsymbol{F}}\psi, \partial_{\bullet}\psi, c_v\vert_{\boldsymbol{I},\boldsymbol{0},\theta_R}\}$,
Implicit equations	θ-based	None	None
	η-based	None	Given θ get η from $\theta = \partial_{\eta}\psi$
In-silico vs lab applicability	θ-based	In-silico	Both
	η-based	In-silico	Both

Table 6: Summary of main features associated with calibration strategies 1 and 2 described in Sections 4.1 and 4.2 for θ or η-based potentials. The function ψ has been used to cover the four possible potentials $\{\Psi, e, \Gamma, \Upsilon\}$, whilst the symbol $\bullet$ refers to either $\boldsymbol{E}_0$ or $\boldsymbol{D}_0$.

5. Finite element implementation of nonlinear thermo-electro-mechanics

5.1. Continuum formulation

An objective of this study is to integrate neural network-based potentials, calibrated using the strategies outlined in Section 4, into a finite element computational framework for the numerical modeling of the governing equations presented in (3), (4) and (5). It is assumed that, irrespective of the chosen thermodynamic potential—whether it be $\Psi(\boldsymbol{F}, \boldsymbol{E}_0, \theta)$, $e(\boldsymbol{F}, \boldsymbol{D}_0, \eta)$, $\Gamma(\boldsymbol{F}, \boldsymbol{E}_0, \eta)$, or $\Upsilon(\boldsymbol{F}, \boldsymbol{D}_0, \theta)$—the corresponding Helmholtz potential, $\Psi(\boldsymbol{F}, \boldsymbol{E}_0, \theta)$, can always be derived via an appropriate Legendre transformation (as shown in equation (18)). Based on this, the weak forms of the governing equations (3), (4) and (5) can be formulated as follows:

$$
\begin{aligned}
\mathcal{W}_{\boldsymbol{\phi}} &= \int_{\mathcal{B}_0} \rho_0 \dot{\boldsymbol{v}} \cdot \boldsymbol{w}_{\boldsymbol{\phi}}\, dV + \int_{\mathcal{B}_0} \partial_{\boldsymbol{F}} \Psi : \partial_{\boldsymbol{X}} \boldsymbol{w}_{\boldsymbol{\phi}}\, dV - \int_{\mathcal{B}_0} \boldsymbol{f}_0 \cdot \boldsymbol{w}_{\boldsymbol{\phi}}\, dV - \int_{\partial_{\boldsymbol{t}}\mathcal{B}_0} \boldsymbol{t}_0 \cdot \boldsymbol{w}_{\boldsymbol{\phi}}\, dA = 0; \\
\mathcal{W}_{\varphi} &= -\int_{\mathcal{B}_0} \partial_{\boldsymbol{D}_0} \Psi \cdot \partial_{\boldsymbol{X}} w_{\varphi}\, dV + \int_{\mathcal{B}_0} \rho_0^e w_{\varphi}\, dV + \int_{\partial_{\omega}\mathcal{B}_0} \omega_0^e \cdot w_{\varphi}\, dA = 0; \\
\mathcal{W}_{\theta} &= -\int_{\mathcal{B}_0} \theta(\partial_{\theta}\dot{\Psi}) w_{\theta}\, dV - \int_{\mathcal{B}_0} \boldsymbol{Q}_{\theta} \cdot \boldsymbol{\nabla}_0 w_{\theta}\, dV - \int_{\mathcal{B}_0} R_{\theta} w_{\theta}\, dV - \int_{\partial_Q \mathcal{B}_0} Q_{\theta} w_{\theta}\, dA = 0,
\end{aligned}
\tag{58}
$$

where $\{\boldsymbol{\phi}, \varphi, \theta\} \in \mathbb{V}^{\boldsymbol{\phi}} \times \mathbb{V}^{\varphi} \times \mathbb{V}^{\theta}$ and $\{\boldsymbol{w}_{\boldsymbol{\phi}}, w_{\varphi}, w_{\theta}\} \in \mathbb{V}_0^{\boldsymbol{\phi}} \times \mathbb{V}_0^{\varphi} \times \mathbb{V}_0^{\theta}$, with

$$
\begin{aligned}
\mathbb{V}^{\boldsymbol{\phi}} &= \left\{ \boldsymbol{\phi} : \mathcal{B}_0 \to \mathbb{R}^3; \quad (\boldsymbol{\phi})_i \in H^1(\mathcal{B}_0) \right\}; & \mathbb{V}_0^{\boldsymbol{\phi}} &= \left\{ \forall \boldsymbol{\phi} \in \mathbb{V}^{\boldsymbol{\phi}}; \quad \boldsymbol{\phi} = \boldsymbol{0} \text{ on } \partial_{\boldsymbol{\phi}}\mathcal{B}_0 \right\}; \\
\mathbb{V}^{\varphi} &= \left\{ \varphi : \mathcal{B}_0 \to \mathbb{R}; \quad \varphi \in H^1(\mathcal{B}_0) \right\}; & \mathbb{V}_0^{\varphi} &= \left\{ \forall \varphi \in \mathbb{V}^{\varphi}; \quad \varphi = 0 \text{ on } \partial_{\varphi}\mathcal{B}_0 \right\}; \\
\mathbb{V}^{\theta} &= \left\{ \theta : \mathcal{B}_0 \to \mathbb{R}; \quad \theta \in H^1(\mathcal{B}_0) \right\}; & \mathbb{V}_0^{\theta} &= \left\{ \forall \theta \in \mathbb{V}^{\theta}; \quad \theta = 0 \text{ on } \partial_{\theta}\mathcal{B}_0 \right\}.
\end{aligned}
\tag{59}
$$

As standard in finite elements, the domain $\mathcal{B}_0$ described in Section 2.1 and representing a thermo-electro-elastic continuum is sub-divided into a finite set of non-overlapping elements $e \in \mathbb{E}$ such that

$$
\mathcal{B}_0 \approx \mathcal{B}_0^h = \bigcup_{e \in \mathbb{E}} \mathcal{B}_0^e. \tag{60}
$$

The unknown fields $\{\boldsymbol{\phi}, \varphi, \theta\}$ in the weak forms $\mathcal{W}_{\boldsymbol{\phi}}$, $\mathcal{W}_{\varphi}$ and $\mathcal{W}_{\theta}$ in (58) are discretised employing the following functional spaces $\mathbb{V}^{\boldsymbol{\phi}^h} \times \mathbb{V}^{\varphi^h} \times \mathbb{V}^{\theta^h}$ defined as

$$
\begin{aligned}
\mathbb{V}^{\boldsymbol{\phi}^h} &= \{ \boldsymbol{\phi} \in \mathbb{V}^{\boldsymbol{\phi}}; \quad \boldsymbol{\phi}^h\big|_{\mathcal{B}_0^e} = \sum_{a=1}^{n_{\text{node}}^{\boldsymbol{\phi}}} N_a^{\boldsymbol{\phi}} \boldsymbol{\phi}_a \}; \qquad \mathbb{V}^{\varphi^h} = \{ \varphi \in \mathbb{V}^{\varphi}; \quad \varphi^h\big|_{\mathcal{B}_0^e} = \sum_{a=1}^{n_{\text{node}}^{\varphi}} N_a^{\varphi} \varphi_a \}; \\
\mathbb{V}^{\theta^h} &= \{ \theta \in \mathbb{V}^{\theta}; \quad \theta^h\big|_{\mathcal{B}_0^e} = \sum_{a=1}^{n_{\text{node}}^{\theta}} N_a^{\theta} \theta_a \},
\end{aligned}
\tag{61}
$$

where for any field $\boldsymbol{\mathcal{Y}} \in \{\boldsymbol{\phi}, \varphi, \theta\}$, $n_{\text{node}}^{\boldsymbol{\mathcal{Y}}}$ denotes the number of nodes per element of the discretisation associated with the field $\boldsymbol{\mathcal{Y}}$ and $N_a^{\boldsymbol{\mathcal{Y}}} : \mathcal{B}_0^e \to \mathbb{R}$, the a^{th} shape function used for the interpolation of $\boldsymbol{\mathcal{Y}}$. In addition, $\boldsymbol{\mathcal{Y}}_a$ represents the value of the field $\boldsymbol{\mathcal{Y}}$ at the a^{th} node of a given finite element. Similarly, following a Bubnov-Galerkin approach, the functional spaces for the test functions $\{\boldsymbol{w}_{\boldsymbol{\phi}}, w_{\varphi}, w_{\theta}\} \in \mathbb{V}_0^{\boldsymbol{\phi}^h} \times \mathbb{V}_0^{\varphi^h} \times \mathbb{V}_0^{\theta^h}$ are defined as

$$
\begin{aligned}
\mathbb{V}_0^{\boldsymbol{\phi}^h} &= \left\{ \forall \boldsymbol{\phi} \in \mathbb{V}^{\boldsymbol{\phi}^h}; \quad \boldsymbol{\phi} = \boldsymbol{0} \text{ on } \partial_{\boldsymbol{\phi}}\mathcal{B}_0 \right\}; \qquad \mathbb{V}_0^{\varphi^h} = \left\{ \forall \varphi \in \mathbb{V}^{\varphi^h}; \quad \varphi = 0 \text{ on } \partial_{\varphi}\mathcal{B}_0 \right\}; \\
\mathbb{V}_0^{\theta^h} &= \left\{ \forall \theta \in \mathbb{V}^{\theta^h}; \quad \theta = 0 \text{ on } \partial_{\theta}\mathcal{B}_0 \right\}.
\end{aligned}
\tag{62}
$$

We have made use of a mid point time integrator where the time derivatives $\dot{\boldsymbol{v}}$ and $\dot{\eta}$ are replaced by the discrete counterparts according to

$$
\dot{\boldsymbol{v}} = \frac{\Delta \boldsymbol{v}}{\Delta t}; \qquad \dot{\eta} = \frac{\Delta \eta}{\Delta t}, \tag{63}
$$

where

$$
\Delta \boldsymbol{v} = \boldsymbol{v} - \boldsymbol{v}_n; \qquad \Delta \eta = \eta - \eta_n, \tag{64}
$$

where $\bullet_n$ stands for the value of a field $\bullet$ in the previous time step, and with Δt the time step size used for the discretization. Furthermore, the velocity field is related with the deformed mapping $\boldsymbol{\phi}$ through the following relationship

$$
\frac{\Delta \boldsymbol{\phi}}{\Delta t} = \boldsymbol{v}_{n+1/2} \tag{65}
$$

where, for any field $\bullet$, $\bullet_{n+1/2}$ stands for

$$\bullet_{n+1/2} = \bullet + \bullet_n. \tag{66}$$

Hence, from equation (65) it is possible to re-express $\boldsymbol{v}_{n+1}$ as

$$\boldsymbol{v}_{n+1} = 2\frac{\Delta\boldsymbol{\phi}}{\Delta t} - \boldsymbol{v}_n, \tag{67}$$

Introduction of (67) into the expression for $\dot{\boldsymbol{v}}$ in (63), featuring in the inertial term in the weak form $\mathcal{W}_{\boldsymbol{\phi}}$ for conservation of linear momentum equation in (58) (see for instance Reference [25]), permits to re-express $\dot{\boldsymbol{v}}$ as

$$\dot{\boldsymbol{v}} = \frac{\boldsymbol{v}_{n+1} - \boldsymbol{v}_n}{\Delta t} = 2\left(\frac{\Delta\boldsymbol{\phi}}{\Delta t^2} - \frac{\boldsymbol{v}_n}{\Delta t}\right). \tag{68}$$

Consideration of the functional spaces for $\{\boldsymbol{\phi}, \varphi, \theta\}$ and $\{\boldsymbol{w}_{\boldsymbol{\phi}}, w_\varphi, w_\theta\}$ in (61) and (62) enables to obtain the semi-discrete version of $\{\mathcal{W}_{\boldsymbol{\phi}}, \mathcal{W}_\varphi, \mathcal{W}_\theta\}$ in (58) in terms of their associated elemental residual contributions, namely

$$\mathcal{W}_{\boldsymbol{\phi}} = \sum_{e=1}^{N} \boldsymbol{w}_{\boldsymbol{\phi}_a} \cdot \boldsymbol{R}^{\boldsymbol{\phi}}_{a,e}; \qquad \mathcal{W}_\varphi = \sum_{e=1}^{N} w_{\varphi_a} \cdot \boldsymbol{R}^{\varphi}_{a,e}; \qquad \mathcal{W}_\theta = \sum_{e=1}^{N} w_{\theta a} R^{\theta}_{a,e}, \tag{69}$$

where N denotes the number of elements for the underlying discretisation. The residual contributions $\boldsymbol{R}^{\boldsymbol{\phi}}_{a,e}$ and $R^{\theta}_{a,e}$ can be expressed as[4]

$$\begin{aligned}
\boldsymbol{R}^{\boldsymbol{\phi}}_{a,e} &= \int_{\mathcal{B}^e_0} \rho_0 N^a_{\boldsymbol{\phi}} \left(2\frac{\Delta\boldsymbol{\phi}}{\Delta t^2} - 2\frac{\boldsymbol{v}_n}{\Delta t}\right) dV + \int_{\mathcal{B}^e_0} \left(\partial_{\boldsymbol{F}}\Psi\right)_{n+1/2} \boldsymbol{\nabla}_0 N^{\boldsymbol{\phi}}_a \, dV - \int_{\mathcal{B}^e_0} N^{\boldsymbol{\phi}}_a \boldsymbol{f}_{0_{n+1/2}} \, dV; \\
\boldsymbol{R}^{\varphi}_{a,e} &= -\int_{\mathcal{B}^e_0} \left(\partial_{\boldsymbol{E}_0}\Psi\right)_{n+1/2} \boldsymbol{\nabla}_0 N^{\varphi}_a \, dV + \int_{\mathcal{B}^e_0} N^{\varphi}_a \rho^e_{0_{n+1/2}} \, dV; \\
R^{\theta}_{a,e} &= -\int_{\mathcal{B}_0} \frac{\theta_{n+1/2}\Delta\left(\partial_\theta\Psi\right)}{\Delta t} N^{\theta}_a \, dV - \int_{\mathcal{B}_0} \boldsymbol{Q}_{n+1/2} \cdot \boldsymbol{\nabla}_0 N^{\theta}_a \, dV - \int_{\mathcal{B}_0} R_{\theta n+1/2} N^{\theta}_a \, dV.
\end{aligned} \tag{70}$$

where use of equation (63) has been made of in the inertial term of the residual $\boldsymbol{R}^{\boldsymbol{\phi}}_{a,e}$ in $(70)_a$. A consistent linearisation of the nonlinear residual contributions (70) has been used in this work. Some details of this linearization can be found in the subsequent section.

5.1.1. Relationship between first and second derivatives of $\Psi(\boldsymbol{F}, \boldsymbol{E}_0, \theta)$ and alternative potentials

The coupled weak forms presented in equation (58) and their residuals in (70) are expressed in terms of the derivatives of the Helmholtz potential, $\Psi(\boldsymbol{F}, \boldsymbol{E}_0, \theta)$. However, the fundamental thermodynamic potential governing the constitutive model can alternatively be one of the three other thermodynamic potentials: $e(\boldsymbol{F}, \boldsymbol{D}_0, \eta)$, $\Gamma(\boldsymbol{F}, \boldsymbol{E}_0, \eta)$, or $\Upsilon(\boldsymbol{F}, \boldsymbol{D}_0, \theta)$. In such cases, the derivatives in (58) and (70), specifically $\{\partial_{\boldsymbol{F}}\Psi, \partial_{\boldsymbol{E}_0}\Psi, \partial_\theta\Psi\}$, must be redefined in terms of these alternative potentials. This is accomplished through the appropriate Legendre transformation (refer to (18)).

This transformation is not only essential for obtaining the first derivatives but is also crucial for deriving the second derivatives of $\Psi(\boldsymbol{F}, \boldsymbol{E}_0, \theta)$, i.e., the components of its Hessian, when the primary thermodynamic potential is either $e(\boldsymbol{F}, \boldsymbol{D}_0, \eta)$, $\Gamma(\boldsymbol{F}, \boldsymbol{E}_0, \eta)$, or $\Upsilon(\boldsymbol{F}, \boldsymbol{D}_0, \theta)$. The following sections will detail the procedures for relating both the first derivatives of $\Psi(\boldsymbol{F}, \boldsymbol{E}_0, \theta)$ and the components of its Hessian to their respective counterparts in the potentials $e(\boldsymbol{F}, \boldsymbol{D}_0, \eta)$, $\Gamma(\boldsymbol{F}, \boldsymbol{E}_0, \eta)$, or $\Upsilon(\boldsymbol{F}, \boldsymbol{D}_0, \theta)$.

[4]For simplicity, the external contributions on the boundary of the continuum and associated with $\boldsymbol{t}_0$ and Q_θ have not been included in (70).

5.1.2. Potential Υ

In this case we consider the case when the underlying thermo-electro-mechanical constitutive model is $\Upsilon(\boldsymbol{F}, \boldsymbol{D}_0, \theta)$. The Legendre transformation in equation $(18)_b$ implies that the field $\boldsymbol{D}_0 := -\partial_{\boldsymbol{E}_0}\Psi$ must be considered as a function of the fields $\{\boldsymbol{F}, \boldsymbol{E}_0, \theta\}$, namely

$$\Upsilon = \Upsilon\left(\boldsymbol{F}, \boldsymbol{D}_0(\boldsymbol{F}, \boldsymbol{E}_0, \theta), \theta\right), \tag{71}$$

and then, $\boldsymbol{D}_0 := -\partial_{\boldsymbol{E}_0}\Psi$ is implicitly solved from this equation

$$\boldsymbol{E}_0 = \partial_{\boldsymbol{D}_0}\Upsilon\left(\boldsymbol{F}, \boldsymbol{D}_0(\boldsymbol{F}, \boldsymbol{E}_0, \theta), \theta\right). \tag{72}$$

Once $\boldsymbol{D}_0 := -\partial_{\boldsymbol{E}_0}\Psi$ is obtained, $\boldsymbol{P} := \partial_{\boldsymbol{F}}\Psi$ and $\eta := -\partial_\theta\Psi$ can be obtained as

$$\begin{aligned} \partial_{\boldsymbol{F}}\Psi\left(\boldsymbol{F}, \boldsymbol{E}_0, \theta\right) &= \partial_{\boldsymbol{F}}\Upsilon\left(\boldsymbol{F}, \boldsymbol{D}_0(\boldsymbol{F}, \boldsymbol{E}_0, \theta), \theta\right); \\ \partial_\theta\Psi\left(\boldsymbol{F}, \boldsymbol{E}_0, \theta\right) &= \partial_\theta\Upsilon\left(\boldsymbol{F}, \boldsymbol{D}_0(\boldsymbol{F}, \boldsymbol{E}_0, \theta), \theta\right). \end{aligned} \tag{73}$$

The components of the Hessian operator of $\Psi(\boldsymbol{F}, \boldsymbol{E}_0, \theta)$, needed for the consistent linearization of (70) can then be related to the components of the Hessian operator of Υ by considering $\boldsymbol{D}_0$ as a function of $\{\boldsymbol{F}, \boldsymbol{E}_0, \theta\}$, as in (71), yielding the following relationships

$$\begin{aligned} &\partial^2_{\boldsymbol{F}\boldsymbol{F}}\Psi = \partial^2_{\boldsymbol{F}\boldsymbol{F}}\Upsilon - \partial^2_{\boldsymbol{F}\boldsymbol{D}_0}\Upsilon\cdot\partial_{\boldsymbol{E}_0\boldsymbol{F}}\Psi; && \partial^2_{\boldsymbol{F}\boldsymbol{E}_0}\Psi = -\partial^2_{\boldsymbol{F}\boldsymbol{D}_0}\Upsilon\cdot\partial_{\boldsymbol{E}_0\boldsymbol{E}_0}\Psi; && \partial^2_{\boldsymbol{F}\theta}\Psi = \partial^2_{\boldsymbol{F}\theta}\Upsilon - \partial^2_{\boldsymbol{F}\boldsymbol{D}_0}\Upsilon\cdot\partial_{\boldsymbol{E}_0\theta}\Psi; \\ &\partial^2_{\boldsymbol{E}_0\boldsymbol{F}}\Psi = \left(\partial^2_{\boldsymbol{E}_0\boldsymbol{F}}\Psi\right)^T; && \partial^2_{\boldsymbol{E}_0\boldsymbol{E}_0}\Psi = -\left(\partial^2_{\boldsymbol{D}_0\boldsymbol{D}_0}\Upsilon\right)^{-1}; && \partial^2_{\boldsymbol{E}_0\theta}\Psi = \left(\partial^2_{\theta\boldsymbol{E}_0}\Psi\right)^T; \\ &\partial^2_{\theta\boldsymbol{F}}\Psi = \left(\partial^2_{\theta\boldsymbol{F}}\Psi\right)^T; && \partial^2_{\theta\boldsymbol{E}_0}\Psi = -\partial^2_{\theta\boldsymbol{D}_0}\Upsilon\cdot\partial_{\boldsymbol{E}_0\boldsymbol{E}_0}\Psi; && \partial^2_{\theta\theta}\Psi = \partial^2_{\theta\theta}\Upsilon - \partial^2_{\theta\boldsymbol{D}_0}\Upsilon\cdot\partial_{\boldsymbol{E}_0\theta}\Psi. \end{aligned} \tag{74}$$

5.1.3. Potential Γ

Let us know consider the case when the underlying thermo-electro-mechanical constitutive model is $\Gamma(\boldsymbol{F}, \boldsymbol{E}_0, \eta)$. In this case, the Legendre transformation in equation $(18)_c$ implies that the field $\eta := -\partial_\theta\Psi$ must be considered as a function of the fields $\{\boldsymbol{F}, \boldsymbol{E}_0, \theta\}$, namely

$$\Gamma = \Gamma\left(\boldsymbol{F}, \boldsymbol{E}_0, \eta(\boldsymbol{F}, \boldsymbol{E}_0, \theta)\right), \tag{75}$$

and then, $\eta := -\partial_\theta\Psi$ is implicitly solved from this equation

$$\theta = \partial_\theta\Gamma\left(\boldsymbol{F}, \boldsymbol{E}_0, \eta(\boldsymbol{F}, \boldsymbol{E}_0, \theta)\right). \tag{76}$$

Once $\eta := -\partial_\theta\Psi$ is obtained, $\boldsymbol{P} = \partial_{\boldsymbol{F}}\Psi$ and $\boldsymbol{D}_0 = -\partial_{\boldsymbol{E}_0}\Psi$ can be obtained as

$$\begin{aligned} \partial_{\boldsymbol{F}}\Psi\left(\boldsymbol{F}, \boldsymbol{E}_0, \theta\right) &= \partial_{\boldsymbol{F}}\Gamma\left(\boldsymbol{F}, \boldsymbol{D}_0, \eta(\boldsymbol{F}, \boldsymbol{E}_0, \theta)\right); \\ \partial_{\boldsymbol{E}_0}\Psi\left(\boldsymbol{F}, \boldsymbol{E}_0, \theta\right) &= \partial_{\boldsymbol{E}_0}\Gamma\left(\boldsymbol{F}, \boldsymbol{D}_0, \eta(\boldsymbol{F}, \boldsymbol{E}_0, \theta)\right). \end{aligned} \tag{77}$$

The components of the Hessian operator of $\Psi(\boldsymbol{F}, \boldsymbol{E}_0, \theta)$, needed for the consistent linearization of (70) can then be related to the components of the Hessian operator of Γ by considering η as a function of $\{\boldsymbol{F}, \boldsymbol{E}_0, \theta\}$, as in (75), yielding the following relationships

$$\begin{aligned} &\partial^2_{\boldsymbol{F}\boldsymbol{F}}\Psi = \partial^2_{\boldsymbol{F}\boldsymbol{F}}\Gamma - \partial^2_{\boldsymbol{F}\eta}\Gamma\cdot\partial_{\theta\boldsymbol{F}}\Psi; && \partial^2_{\boldsymbol{F}\boldsymbol{E}_0}\Psi = \partial^2_{\boldsymbol{F}\boldsymbol{E}_0}\Gamma - \partial^2_{\boldsymbol{F}\eta}\Gamma\cdot\partial_{\theta\boldsymbol{E}_0}\Psi; && \partial^2_{\boldsymbol{F}\theta}\Psi = -\partial^2_{\boldsymbol{F}\eta}\Gamma\cdot\partial_{\theta\theta}\Psi; \\ &\partial^2_{\boldsymbol{E}_0\boldsymbol{F}}\Psi = \left(\partial^2_{\boldsymbol{E}_0\boldsymbol{F}}\Psi\right)^T; && \partial^2_{\boldsymbol{E}_0\boldsymbol{E}_0}\Psi = -\partial^2_{\boldsymbol{E}_0\boldsymbol{E}_0}\Gamma - \partial^2_{\boldsymbol{E}_0\eta}\Gamma\cdot\partial_{\theta\boldsymbol{E}_0}\Psi; && \partial^2_{\boldsymbol{E}_0\theta}\Psi = -\partial^2_{\boldsymbol{E}_0\eta}\Gamma\cdot\partial_{\theta\theta}\Psi; \\ &\partial^2_{\theta\boldsymbol{F}}\Psi = \left(\partial^2_{\theta\boldsymbol{F}}\Psi\right)^T; && \partial^2_{\theta\boldsymbol{E}_0}\Psi = \left(\partial^2_{\boldsymbol{E}_0\theta}\Psi\right)^T; && \partial^2_{\theta\theta}\Psi = -\left(\partial^2_{\eta\eta}\Gamma\right)^{-1}. \end{aligned} \tag{78}$$

5.1.4. Potential e

Finally, let us consider the case when the underlying thermo-electro-mechanical constitutive model is $e(\boldsymbol{F}, \boldsymbol{D}_0, \eta)$. In this case, the Legendre transformation in equation $(18)_a$ implies that both fields $\boldsymbol{D}_0 := -\partial_{\boldsymbol{E}_0}\Psi$ and $\eta := -\partial_\theta \Psi$ must be considered as functions of the fields $\{\boldsymbol{F}, \boldsymbol{E}_0, \theta\}$, namely

$$e = e\left(\boldsymbol{F}, \boldsymbol{D}_0(\boldsymbol{F}, \boldsymbol{E}_0, \theta), \eta(\boldsymbol{F}, \boldsymbol{E}_0, \theta)\right), \tag{79}$$

and then, $\boldsymbol{D}_0 := -\partial_{\boldsymbol{E}_0}\Psi$ and $\eta := -\partial_\theta \Psi$ are simultaneously implicitly solved from these equations

$$\begin{aligned} \boldsymbol{E}_0 &= \partial_{\boldsymbol{D}_0} e\left(\boldsymbol{F}, \boldsymbol{D}_0(\boldsymbol{F}, \boldsymbol{E}_0, \theta), \eta(\boldsymbol{F}, \boldsymbol{E}_0, \theta)\right); \\ \theta &= \partial_\eta e\left(\boldsymbol{F}, \boldsymbol{D}_0(\boldsymbol{F}, \boldsymbol{E}_0, \theta), \eta(\boldsymbol{F}, \boldsymbol{E}_0, \theta)\right). \end{aligned} \tag{80}$$

Once $\boldsymbol{D}_0 := -\partial_{\boldsymbol{E}_0}\Psi$ and $\eta := -\partial_\theta \Psi$ are obtained, $\boldsymbol{P} = \partial_{\boldsymbol{F}}\Psi$ can be obtained as

$$\partial_{\boldsymbol{F}}\Psi\left(\boldsymbol{F}, \boldsymbol{E}_0, \theta\right) = \partial_{\boldsymbol{F}} e\left(\boldsymbol{F}, \boldsymbol{D}_0(\boldsymbol{F}, \boldsymbol{E}_0, \theta), \eta(\boldsymbol{F}, \boldsymbol{E}_0, \theta)\right). \tag{81}$$

The components of the Hessian operator of $\Psi(\boldsymbol{F}, \boldsymbol{E}_0, \theta)$, needed for the consistent linearization of (70) can then be related to the components of the Hessian operator of e by considering $\boldsymbol{D}_0$ and η as functions of $\{\boldsymbol{F}, \boldsymbol{E}_0, \theta\}$, as in (79), yielding the following relationships

$$\begin{aligned} &\partial^2_{\boldsymbol{F}\boldsymbol{F}}\Psi = \partial^2_{\boldsymbol{F}\boldsymbol{F}} e - \partial^2_{\boldsymbol{F}\boldsymbol{D}_0} e \cdot \partial_{\boldsymbol{E}_0\boldsymbol{F}}\Psi - \partial^2_{\boldsymbol{F}\eta} e \cdot \partial_{\theta\boldsymbol{F}}\Psi; \qquad && \partial^2_{\boldsymbol{F}\boldsymbol{E}_0}\Psi = -\partial^2_{\boldsymbol{F}\boldsymbol{D}_0} e \cdot \partial_{\boldsymbol{E}_0\boldsymbol{E}_0}\Psi - \partial^2_{\boldsymbol{F}\eta} e \cdot \partial_{\theta\boldsymbol{E}_0}\Psi; \\ &\partial^2_{\boldsymbol{F}\theta}\Psi = -\partial^2_{\boldsymbol{F}\boldsymbol{D}_0} e \cdot \partial_{\boldsymbol{E}_0\theta}\Psi - \partial^2_{\boldsymbol{F}\eta} e \cdot \partial_{\theta\theta}\Psi; && \partial^2_{\boldsymbol{E}_0\boldsymbol{F}}\Psi = \left(\partial^2_{\boldsymbol{F}\boldsymbol{E}_0}\Psi\right)^T; \\ &\partial^2_{\theta\boldsymbol{F}}\Psi = \left(\partial^2_{\boldsymbol{F}\theta}\Psi\right)^T; && \begin{bmatrix} \partial^2_{\boldsymbol{E}_0\boldsymbol{E}_0}\Psi & \partial^2_{\boldsymbol{E}_0\theta}\Psi \\ \partial^2_{\theta\boldsymbol{E}_0}\Psi & \partial^2_{\theta\theta}\Psi \end{bmatrix} = -\begin{bmatrix} \partial^2_{\boldsymbol{D}_0\boldsymbol{D}_0} e & \partial^2_{\boldsymbol{D}_0\eta} e \\ \partial^2_{\eta\boldsymbol{D}_0} e & \partial^2_{\eta\eta} e \end{bmatrix}^{-1}. \end{aligned} \tag{82}$$

6. Calibration and validation of the thermodynamic potentials

This section presents the calibration results for various types of neural network-based thermodynamic potentials, namely Ψ_{nn}, e_{nn}, Γ_{nn} and Υ_{nn}, calibrated according to both calibration strategies described in Sections 4.1 and 4.2.

6.1. Calibration strategy 1

We begin showing the calibration results by using Sobolev-type calibration strategy 1.

6.1.1. Neural network architecture's influence: Ψ_{nn} Neural Network-based ground truth models

The objective of this preliminary study is to investigate a specific neural network-based thermodynamic potential, namely $\Psi_{nn}(\boldsymbol{F}, \boldsymbol{E}_0, \theta)$. Our focus is to assess how variations in the neural network architecture influence the accuracy of the potential's calibration. The network architecture is characterised by the number of hidden layers, n_L, and an equal number of neurons per layer, denoted as n_n. By varying these parameters, we track the R^2 values of the second-order derivatives of the potential–R^2 in the derivatives of the potential, namely $R^2(\partial^2_{\boldsymbol{F}}\Psi_{nn})$, $R^2(\partial^2_{\boldsymbol{E}_0}\Psi_{nn})$ and $R^2(\partial^2_\theta \Psi_{nn})$–for both training and testing datasets. It is important to note that the training data, used for calibrating the potential across all architectures, constitutes 20% of the testing dataset.

Table 7 shows the results obtained for the calibrated models Ψ_{nn}, not only across different neural network architectures but also when employing the various models described in Section 3.5. These models represent both the purely mechanical and electro-mechanical contributions of the ground truth Helmholtz strain energy model used for the calibration of all the potentials (see equation (33)). The results obtained in this table indicate that in general, the optimisation

	n_L (number of hidden layers)	2	4
	n_n (neurons per layer)	8	8
MR/ID	$R^2(\partial_{\boldsymbol{F}}\Psi)$	0.988246	0.999850
	$R^2(\partial_{\boldsymbol{E}_0}\Psi)$	0.993956	0.999989
	$R^2(\partial_\theta\Psi)$	0.999955	0.999998
QMR/ID	$R^2(\partial_{\boldsymbol{F}}\Psi)$	0.999701	0.999948
	$R^2(\partial_{\boldsymbol{E}_0}\Psi)$	0.999974	0.999978
	$R^2(\partial_\theta\Psi)$	0.999964	0.999998
Y/ID	$R^2(\partial_{\boldsymbol{F}}\Psi)$	0.999834	0.999918
	$R^2(\partial_{\boldsymbol{E}_0}\Psi)$	0.999973	0.999943
	$R^2(\partial_\theta\Psi)$	0.999737	0.999956
G/ID	$R^2(\partial_{\boldsymbol{F}}\Psi)$	0.999776	0.999045
	$R^2(\partial_{\boldsymbol{E}_0}\Psi)$	0.999941	0.999896
	$R^2(\partial_\theta\Psi)$	0.999940	0.999989
TI/ID	$R^2(\partial_{\boldsymbol{F}}\Psi)$	0.997358	0.999601
	$R^2(\partial_{\boldsymbol{E}_0}\Psi)$	0.99975103	0.999920
	$R^2(\partial_\theta\Psi)$	0.9997285	0.999980
MR/ES	$R^2(\partial_{\boldsymbol{F}}\Psi)$	0.998902	0.999889
	$R^2(\partial_{\boldsymbol{E}_0}\Psi)$	0.999758	0.999932
	$R^2(\partial_\theta\Psi)$	0.999989	0.999998

Table 7: **Calibration Strategy 1**. Values of the $R^2(\partial_{\boldsymbol{F}}\Psi)$, $R^2(\partial_{\boldsymbol{E}_0}\Psi)$ and $R^2(\partial_\theta\Psi)$ obtained in the calibration of Ψ_{nn} (hence using the training dataset) using the purely mechanical (in red) and electro-mechanical (in blue) contributions of the ground truth Helmholtz strain energy model used for the calibration.

algorithm used for the calibration of the models (Adam algorithm with a learning rate of 0.001) attains a very satisfactory local minimum.

Importantly, the calibrated models $\Psi_{nn}(\boldsymbol{F}, \boldsymbol{E}_0, \theta)$ have been evaluated against an independent dataset not included in the original training set. This larger dataset, referred to as the test dataset, has been used to assess the performance of the neural network-based potentials calibrated for all ground truth models considered, utilizing a specific neural network architecture. In this study, we have focused on models comprising four hidden layers with eight neurons per layer. The correlation results, presented in Figure 7, demonstrate the calibrated models' robust capability to accurately predict the responses of the ground truth models across a significantly broader dataset than the training set.

We have conducted additional testing of the calibrated models in scenarios beyond those included in the training set. It is important to note that both the training and testing sets were generated using a similar in-silico data generation strategy, as outlined in Appendix A and based on the methodology of [43], in which the deformation gradient tensor and the electric field are defined according to

$$\boldsymbol{F} = \begin{bmatrix} \lambda & \gamma & 0 \\ 0 & \lambda & 0 \\ 0 & 0 & 1/\lambda^2 \end{bmatrix}; \; 1 \leq \lambda \leq 1.5; \; 0 \leq \gamma \leq 0.5 \qquad \boldsymbol{E}_0 = \begin{bmatrix} \alpha \\ \alpha \\ 0 \end{bmatrix} \; 0 \leq \alpha \leq 1.5\sqrt{\frac{\bar{\mu}}{\bar{\varepsilon}}}. \tag{83}$$

The objective is to assess the agreement between the derivatives of the calibrated model, $\Psi_{nn}(\boldsymbol{F}, \boldsymbol{E}_0, \theta)$, and those of the ground truth model across various temperature values for the specified experimental setup. Figure 8 illustrates this comparison, focusing on the neural network-based potential $\Psi_{nn}(\boldsymbol{F}, \boldsymbol{E}_0, \theta)$ and a single ground truth constitutive model. The figure demonstrates a remarkable alignment between the calibrated and ground truth models, highlighting the calibrated model's capacity to accurately predict the ground truth response, even in scenarios outside its training domain.

6.1.2. Generalization results for physically motivated training datasets

In addition to the training and testing datasets generated following the strategy outlined in Section Appendix A and the methodology described in [43], this section examines the generalization performance of the neural network potential when the training data aligns more closely with experimental conditions typically encountered in laboratory settings. Specifically, we consider a parameterization of the deformation gradient tensor, $\boldsymbol{F}$, that corresponds to uniaxial combined with shear, and biaxial loading scenarios. These cases are defined as:

$$\begin{aligned} \boldsymbol{F}_{\text{uniaxial/shear}} &= J^{-1/3} \begin{bmatrix} \lambda & 0 & 0 \\ \gamma & \lambda & 0 \\ 0 & 0 & 1/\lambda^2 \end{bmatrix}; \; 1 \leq \lambda \leq 1.5; \; 0 \leq \gamma \leq 0.5 \; 0.8 \leq J \leq 1.2 \\ \boldsymbol{F}_{\text{biaxial}} &= J^{-1/3} \begin{bmatrix} 0 & \lambda & 0 & 0 \\ & \lambda & 0 & \\ 0 & 0 & 1/\lambda^2 & \end{bmatrix}; \; 1 \leq \lambda \leq 1.5; \; 0.8 \leq J \leq 1.2 \end{aligned} \tag{84}$$

considering 5 different values of λ, γ and J in the above parametrization. In addition, the electric field $\boldsymbol{E}_0$ has been parametrized for training according to

$$\boldsymbol{E}_0 = \alpha \boldsymbol{n}_{\boldsymbol{E}_0}; \quad 0 \leq \alpha \leq 2.2\sqrt{\frac{\bar{\mu}}{\bar{\varepsilon}}}. \tag{85}$$

where we have considered 5 possible values for the norm of the electric field α and five possible unitary orientations $\boldsymbol{n}_{\boldsymbol{E}_0}$. Furthermore, we have considered 10 values of θ such that

$$\theta_R - 60 \leq \theta \leq \theta_R + 60 \tag{86}$$

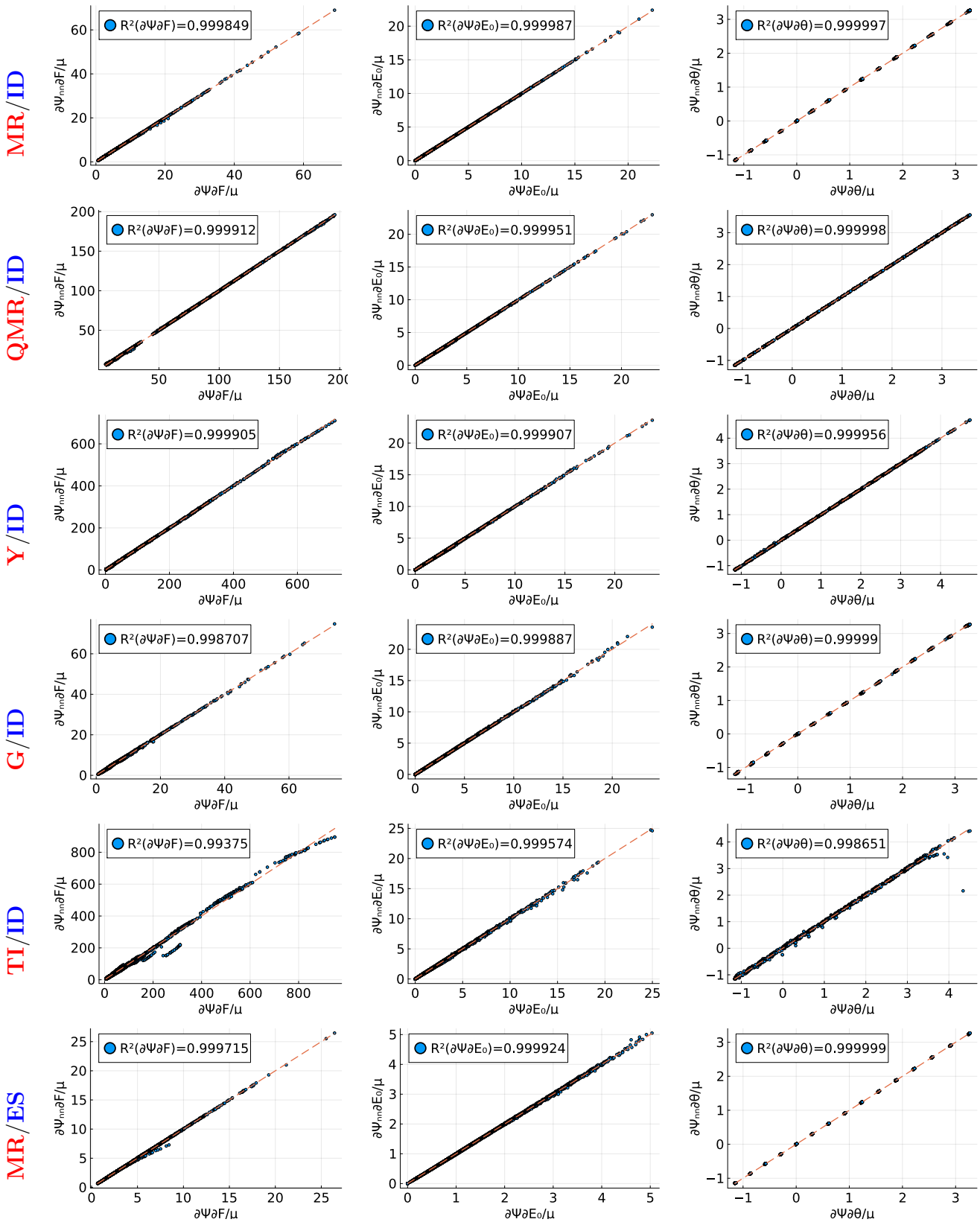

Figure 7: **Calibration Strategy 1**. Correlation of prediction $\{\partial_{\boldsymbol{F}}\Psi_{nn}, \partial_{\boldsymbol{E}_0}\Psi_{nn}, \partial_\theta\Psi_{nn}\}$ and testing data $\{\partial_{\boldsymbol{F}}\Psi, \partial_{\boldsymbol{E}_0}\Psi, \partial_\theta\Psi\}$ using the purely mechanical (in red) and electro-mechanical (in blue) contributions of the ground truth Helmholtz strain energy model used for the calibration. The training data represents a subset of the testing data containing the 20% of the data in the latter. In all cases we have considered an architecture of 4 hidden layers and 8 neurons per layer.

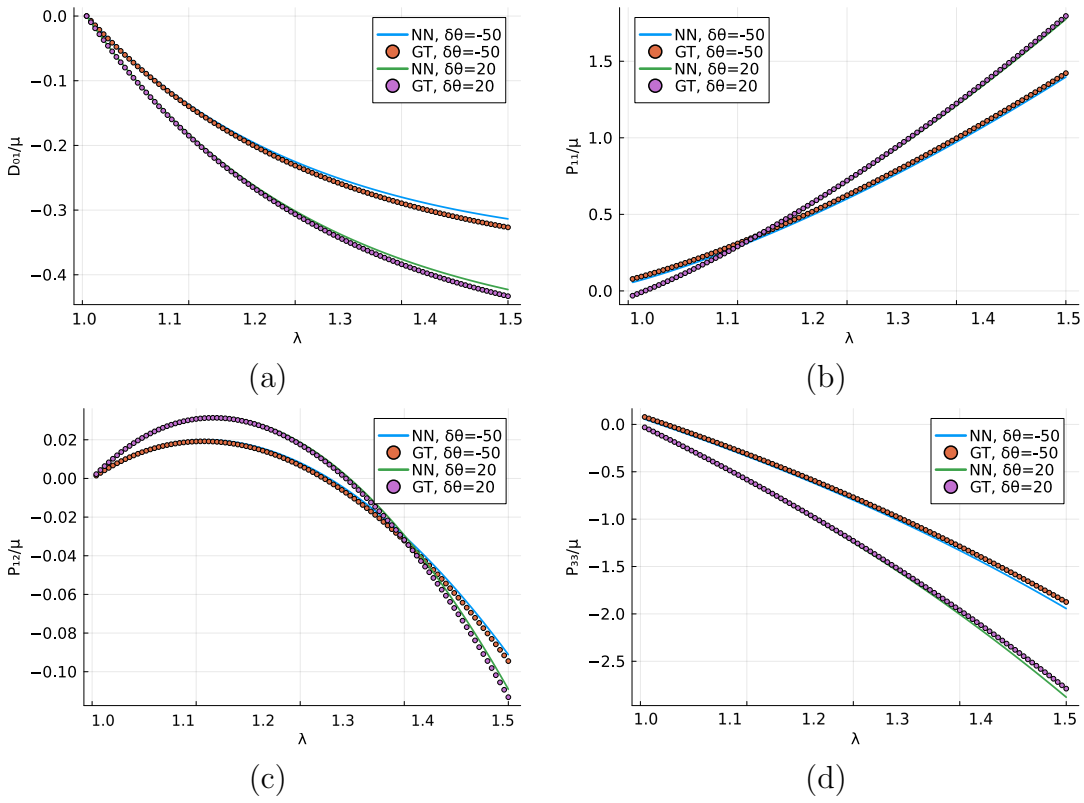

Figure 8: **Calibration Strategy 1**. Prediction of calibrated model $\Psi_{nn}(\boldsymbol{F}, \boldsymbol{E}_0, \theta)$ and ground truth model across various temperature values for the experimental setup in (83). The ground truth model $\Psi(\boldsymbol{F}, \boldsymbol{E}_0, \theta)$ considers a Mooney-Rivlin model for the mechanical contribution, i.e. Ψ_m and an ideal dielectric model for the electro-mechanical contribution, i.e. Ψ_{em} (see (33)). Architecture with 4 hidden layers and 8 neurons per layer.

Finally, we limit the training dataset to include 1000 points. We have considered the case where the ground truth model consideres a Mooney-Rivlin model for the mechanical contribution, i.e. Ψ_m and an ideal dielectric model for the electro-mechanical contribution, i.e. Ψ_{em} (see (33)). We have tested the generalization capabilities of the neural network model, by considering a different testing data set to that considered in equations (84)-(86). For that, we consider the following parametrization of $\boldsymbol{F}$ (where the shear component is now prescribed in the component 13 of $\boldsymbol{F}$, instead of in the component 12 as in equation (84)) and $\boldsymbol{E}_0$

$$\boldsymbol{F} = \begin{bmatrix} \lambda & 0 & 0 \\ 0 & \lambda & 0 \\ \gamma & 0 & 1/\lambda^2 \end{bmatrix}; \; 1 \leq \lambda \leq 1.5; \; 0 \leq \gamma \leq 0.5 \qquad \boldsymbol{E}_0 = \alpha \begin{bmatrix} 1 \\ 1 \\ 0 \end{bmatrix} \; 0 \leq \alpha \leq 1.5\sqrt{\frac{\bar{\mu}}{\bar{\varepsilon}}}. \tag{87}$$

where the direction $\begin{bmatrix} 1 & 1 & 0 \end{bmatrix}^T$ was not considered in the training dataset. Taking this into account, the neural network model's response on the testing dataset, defined by equation (87), demonstrates good agreement with the response of the underlying ground truth model for two temperature values outside the range included in the training data.

6.1.3. Generalization results for all the thermodynamical potentials

In the previous section, we focused exclusively on the calibration of Helmholtz-type neural network-based potentials, specifically $\Psi_{nn}(\boldsymbol{F}, \boldsymbol{E}_0, \theta)$. The objective of this section, however, is to demonstrate that, while we have primarily considered a Helmholtz-type ground truth potential $\Psi(\boldsymbol{F}, \boldsymbol{E}_0, \theta)$, we can successfully calibrate neural network-based potentials corresponding to alternative formulations, namely $e_{nn}(\boldsymbol{F}, \boldsymbol{D}_0, \eta)$, $\Upsilon_{nn}(\boldsymbol{F}, \boldsymbol{D}_0, \theta)$ and $\Gamma_{nn}(\boldsymbol{F}, \boldsymbol{E}_0, \eta)$, as outlined in Section 4.1.1. In order to illustrate this capability, we consider the following case:

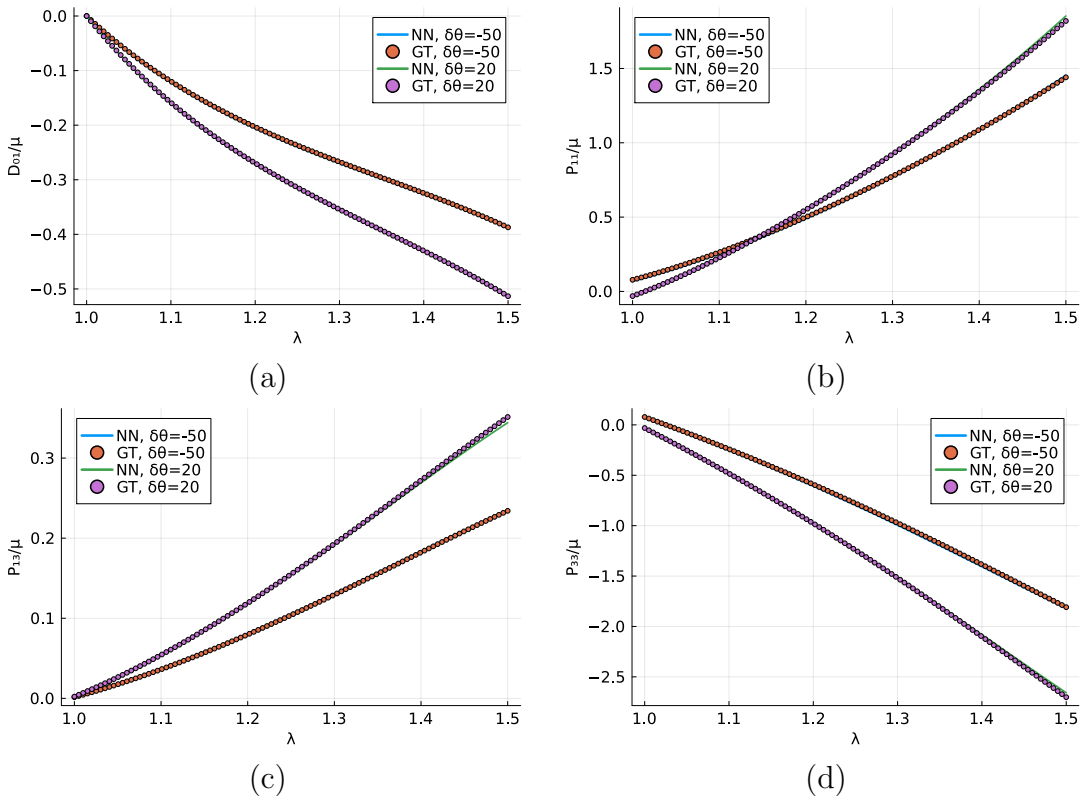

Figure 9: **Calibration Strategy 1**. Prediction of calibrated model $\Psi_{nn}(\boldsymbol{F}, \boldsymbol{E}_0, \theta)$ and ground truth model across various temperature values for the experimental setup in (83). The ground truth model $\Psi(\boldsymbol{F}, \boldsymbol{E}_0, \theta)$ considers a Mooney-Rivlin model for the mechanical contribution, i.e. Ψ_m and an ideal dielectric model for the electromechanical contribution, i.e. Ψ_{em} (see (33)). Architecture with 4 hidden layers and 8 neurons per layer.

- Fixed neural network architecture with 4 hidden layers and 8 neurons.
- Ground truth model with Ψ_m corresponding with a Mooney-Rivlin model and Ψ_{em} with an ideal dielectric model (see (33)).

Under such scenario, Figure 10 presents the correlation results for the test dataset, which is larger than the training dataset, for the four potentials, namely $\Psi_{nn}(\boldsymbol{F}, \boldsymbol{E}_0, \theta)$, $e_{nn}(\boldsymbol{F}, \boldsymbol{D}_0, \eta)$, $\Upsilon_{nn}(\boldsymbol{F}, \boldsymbol{D}_0, \theta)$ and $\Gamma_{nn}(\boldsymbol{F}, \boldsymbol{E}_0, \eta)$. The figure demonstrates an excellent agreement between the predictions made by the calibrated potentials and the ground truth model, confirming the reliability of the calibrated models in predicting the behavior of the ground truth.

6.1.4. Polyconvex calibration

The aim of this section is to evaluate the accuracy of polyconvex neural network-based potentials defined in the thermodynamic potential $e_{nn}(\boldsymbol{F}, \boldsymbol{D}_0, \eta)$. As discussed in Section 4.1.2, polyconvexity of $e_{nn}(\boldsymbol{F}, \boldsymbol{D}_0, \eta)$ is enforced through the augmented loss function described in equation (50). While polyconvex functions generally offer less flexibility compared to their non-polyconvex counterparts, Figure 11 demonstrates a reasonably good agreement with the ground truth model, which consists of a Mooney-Rivlin model for Ψ_m and an ideal dielectric model for Ψ_{em} (see (33)). This result was achieved using a neural network architecture with 4 hidden layers and 8 neurons, as depicted in Figure 11.

The absence of a *perfect* agreement evidenced by the polyconvex neural network-based model in Figure 11 (specially in the prediction of $\partial_{\boldsymbol{F}} e$) could be explained due to the fact that the neural network-based model is indeed polyconvex with respect to the set of variables $\{\boldsymbol{F}, \boldsymbol{H}, J, \boldsymbol{D}_0, \boldsymbol{d}, \eta\}$. However, the underlying ground truth model depends on the variables $\{\boldsymbol{F}, \boldsymbol{H}, J, \boldsymbol{E}_0, \theta\}$ (see equation (33)) and there is no guarantee that even rank-one convexity with respect to the mechan-

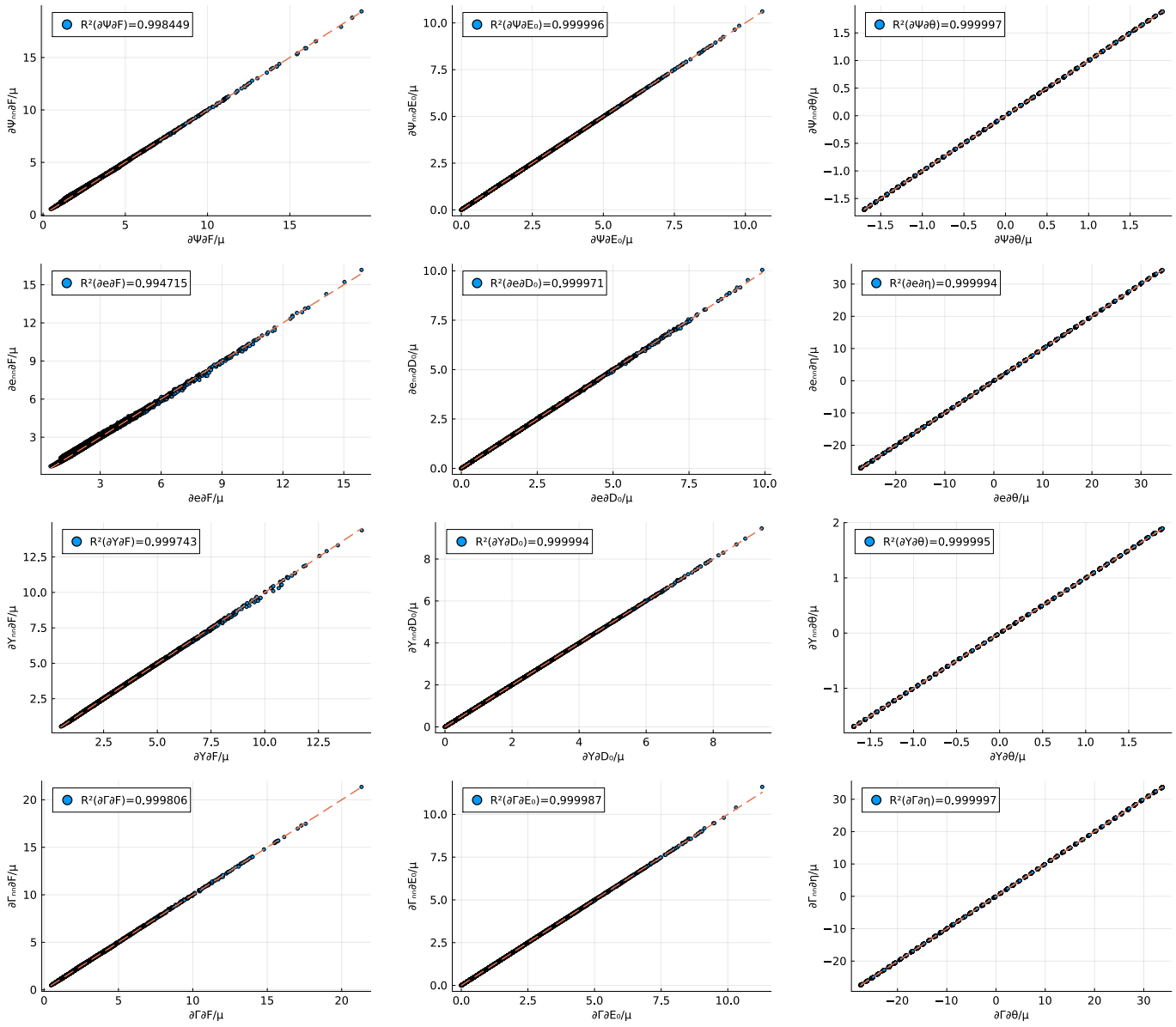

Figure 10: **Calibration Strategy 1**. Correlation of prediction $\{\partial_{\boldsymbol{F}}\Psi_{nn}, \partial_{\boldsymbol{E}_0}\Psi_{nn}, \partial_\theta\Psi_{nn}\}$, $\{\partial_{\boldsymbol{F}}e_{nn}, \partial_{\boldsymbol{D}_0}e_{nn}, \partial_\eta e_{nn}\}$, $\{\partial_{\boldsymbol{F}}\Upsilon_{nn}, \partial_{\boldsymbol{D}_0}\Upsilon_{nn}, \partial_\theta\Upsilon_{nn}\}$ and $\{\partial_{\boldsymbol{F}}\Gamma_{nn}, \partial_{\boldsymbol{E}_0}\Gamma_{nn}, \partial_\eta\Gamma_{nn}\}$ and their testing data counterparts. In all cases we have considered an architecture of 4 hidden layers and 8 neurons per layer.

ical physics holds for all values of θ. A similar challenge arises when attempting to replicate the homogenized behavior of rank-one laminates—whether in finite-strain mechanics or electro-mechanics—using polyconvex neural networks (refer to [37]). Since the underlying ground truth model is not inherently polyconvex, polyconvex neural network models are unable to perfectly capture its behaviour.

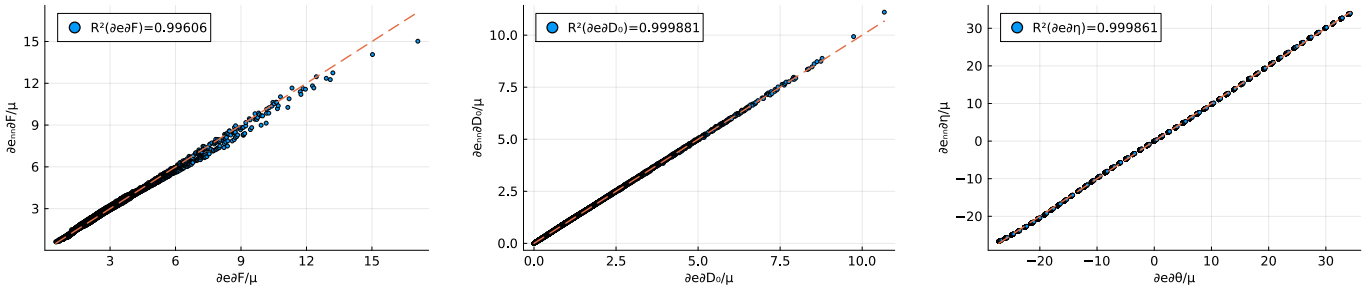

Figure 11: **Calibration Strategy 1**. Correlation of prediction $\{\partial_{\boldsymbol{F}} e_{nn}, \partial_{\boldsymbol{D}_0} e_{nn}, \partial_\eta e_{nn}\}$ and the testing data counterpart $\{\partial_{\boldsymbol{F}} e, \partial_{\boldsymbol{D}_0} e, \partial_\eta e\}$ (obtained through appropriate Legendre transformation of the derivatives of $\Psi(\boldsymbol{F}, \boldsymbol{E}_0, \theta)$). Polyconvexity of e_{nn} has been imposed according to the strategy described in Section 4.1.2. Fixed architecture with 4 hidden layers and 8 neurons. The ground truth model comprises a Mooney-Rivlin model for Ψ_m and ideal dielectric model for Ψ_{em} (see (33)).

The results presented in Figure 11 were obtained using a penalty parameter value of $\kappa = 10$. For this particular value, the polyconvexity constraint in (50) is almost satisfied, as evidenced by the ratio between the largest negative and the largest positive weights in the neural network. Specifically, the ratio is defined as

$$\lambda_W = \frac{\min\Big(\min(\boldsymbol{\mathcal{W}}_v), 0\Big)}{\max(\boldsymbol{\mathcal{W}}_v)} \tag{88}$$

For this configuration, we find that $\lambda_W \approx -10^{-4}$. Increasing the penalty parameter κ generally enhances the likelihood of satisfying the polyconvexity condition, as it enforces the weights of the neural network to remain positive. Conversely, using smaller values of κ relaxes the polyconvexity constraint, which may lead to a greater violation of the condition but potentially higher prediction accuracy. This effect is particularly pronounced when the underlying ground truth model does not exhibit polyconvexity, as previously discussed. The interplay between these factors can be observed in Figure 12. It is important to note that in all tests conducted, the value of κ remained constant throughout the entire optimization process. Implementing a more advanced continuation strategy, where κ is updated adaptively during the optimization, could further improve the satisfaction of the polyconvexity/weight positivity constraints.

6.2. Calibration strategy 2: θ-based potentials

The objective of this study is to demonstrate the accuracy and flexibility of the calibration strategy 2 for neural network-based potentials that depend upon θ, namely $\Psi_{nn}(\boldsymbol{F}, \boldsymbol{E}_0, \theta)$ and $\Upsilon_{nn}(\boldsymbol{F}, \boldsymbol{D}_0, \theta)$, described in Section 4.2.1. We will consider though only the case of $\Psi_{nn}(\boldsymbol{F}, \boldsymbol{E}_0, \theta)$. For a fixed neural network architecture of 4 hidden layers and 8 neurons, the objective is to assess the performance of the neural network-based potentials calibrated for all ground truth models considered. The correlation results, presented in Figure 13, demonstrate the calibrated models' robust capability to accurately predict the responses of the ground truth models across a significantly broader dataset than the training set.

Furthermore, we have considered the same unseen (by the training set) experimental set up described in equation (83) in order to further test the prediction capabilities of the calibrated

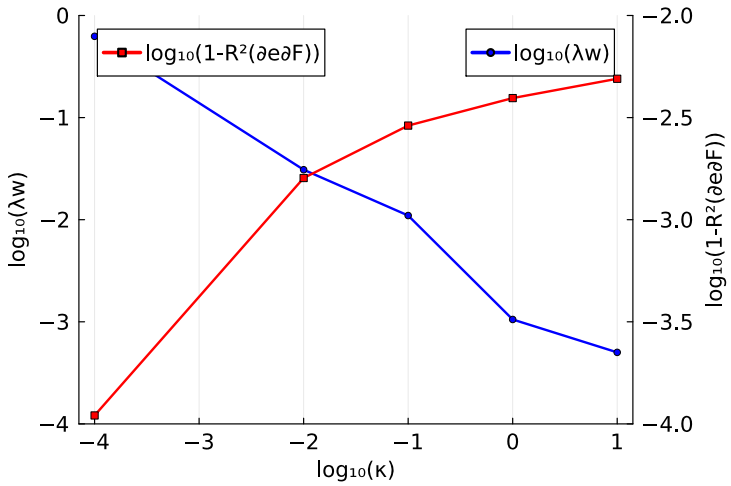

Figure 12: **Calibration Strategy 1**. Influence of the penalty parameter κ (see equation (50)) on: (i) the accuracy of the correlation of the prediction for $\partial_{\boldsymbol{F}} e$ (corresponding with the red curve and the right axis); (ii) the satisfaction of polyconvexity, encapsulated by the indicator λ_W (see equation (88)). Notice that $\log_{10}(1 - R^2(\partial_{\boldsymbol{F}} e))$ informs about the number of 9's in the decimal representation of $R^2(\partial_{\boldsymbol{F}} e)$.

neural network models in data not contemplated in the training. The results of this prediction are shown in Figure 14 exclusively for the case where the ground truth model comprises a Mooney-Rivlin model for Ψ_m and an ideal dielectric model for Ψ_{em}, demonstrating a remarkable alignment between the calibrated and ground truth models, highlighting the calibrated model's capacity to accurately predict the ground truth response, even in scenarios ouside its training domain.

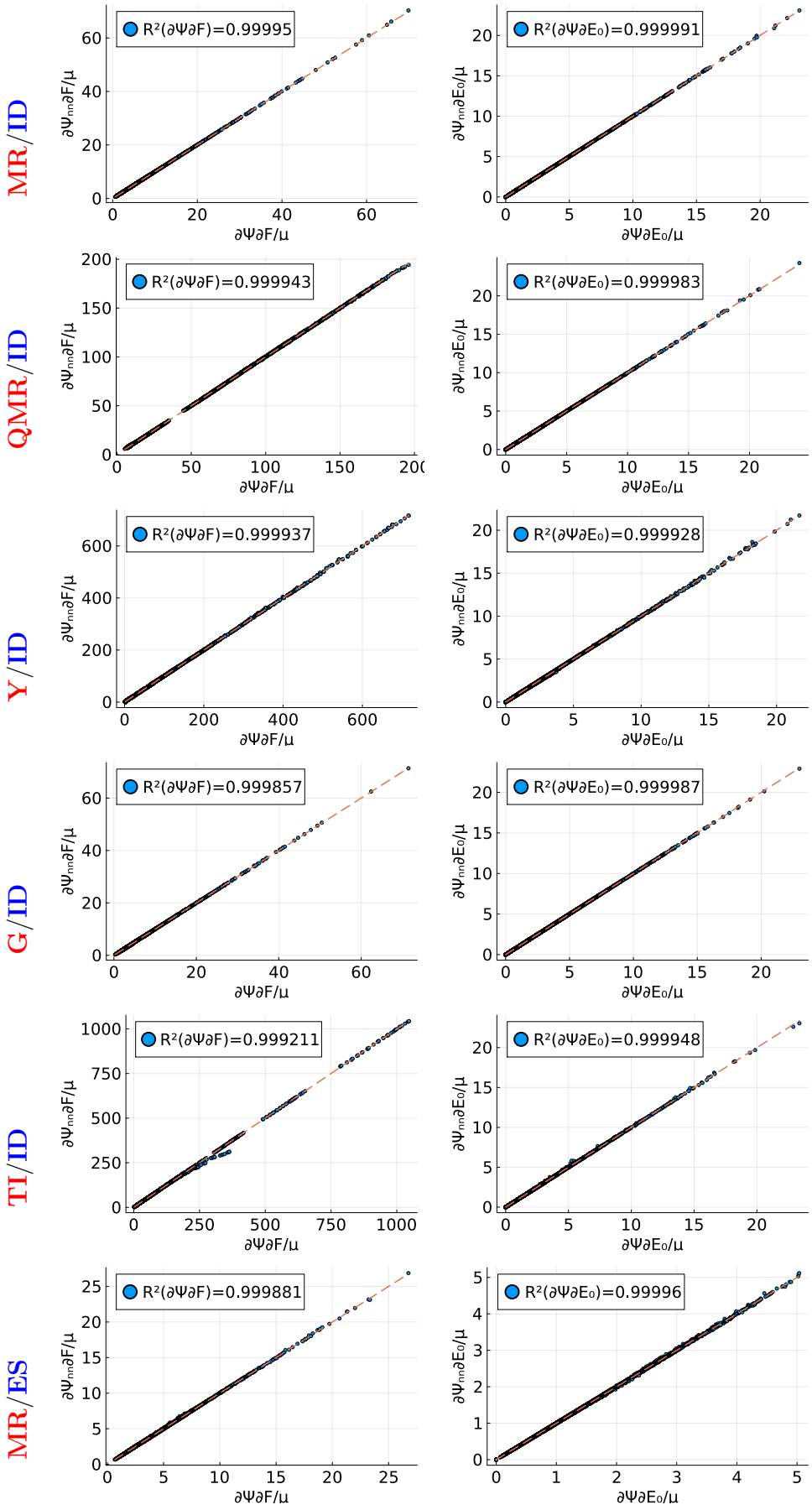

Figure 13: **Calibration Strategy 2: θ-based potentials**. Correlation of prediction $\{\partial_{\boldsymbol{F}}\Psi_{nn}, \partial_{\boldsymbol{E}_0}\Psi_{nn}\}$ and testing data $\{\partial_{\boldsymbol{F}}\Psi, \partial_{\boldsymbol{E}_0}\Psi\}$ using the purely mechanical (in red) and electro-mechanical (in blue) contributions of the ground truth Helmholtz strain energy model used for the calibration. The training data represents a subset of the testing data containing the 20% of the data in the latter. In all cases we have considered an architecture of 4 hidden layers and 8 neurons per layer.

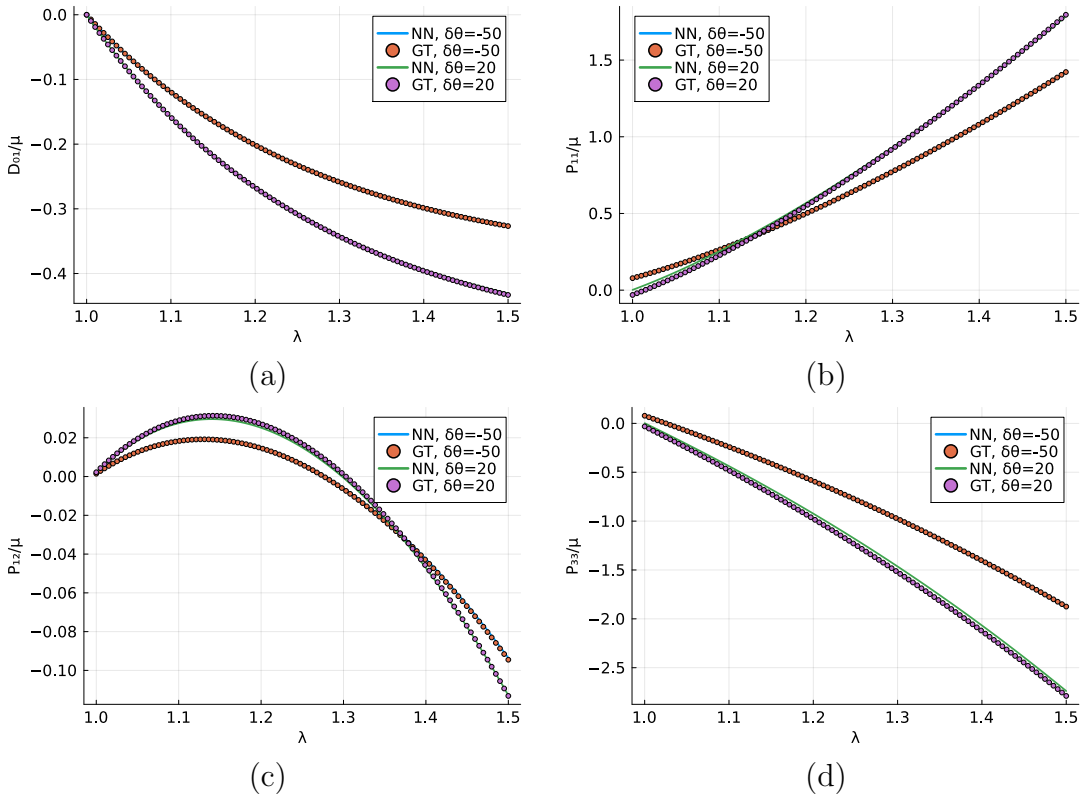

Figure 14: **Calibration Strategy 2: θ-based potentials**. Prediction of calibrated model $\Psi_{nn}(\boldsymbol{F}, \boldsymbol{E}_0, \theta)$ and ground truth model across various temperature values for the experimental setup in (83). The ground truth model $\Psi(\boldsymbol{F}, \boldsymbol{E}_0, \theta)$ considers a Mooney-Rivlin model for the mechanical contribution, i.e. Ψ_m and an ideal dielectric model for the electro-mechanical contribution, i.e. Ψ_{em} (see (33)). Architecture with 4 hidden layers and 8 neurons per layer.

6.3. Calibration strategy 2: η-based potentials

In this section we proceed for the calibration of η-based potentials, namely $e_{nn}(\boldsymbol{F}, \boldsymbol{D}_0, \eta)$ and $\Gamma_{nn}(\boldsymbol{F}, \boldsymbol{E}_0, \eta)$ according to the calibration strategy 2 outlined in Section 4.2.2. Specifically, we will consider only potentials of the form $e_{nn}(\boldsymbol{F}, \boldsymbol{D}_0, \eta)$. For a fixed architecture of 4 hidden layers and 8 neurons, considering only one ground truth model (comprising a Mooney-Rivlin model for Ψ_m and ideal dielectric for Ψ_{em}), the objective is to asses the ability to predict the response of the ground truth model.

The correlation results presented in Figure 15 demonstrate the calibrated model's robust capability to accurately predict the responses of the ground truth models across a significantly broader dataset than the training set.

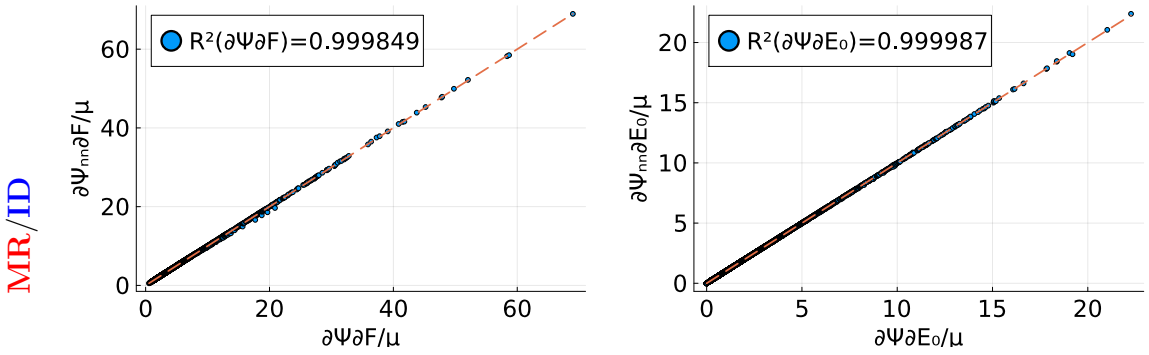

Figure 15: **Calibration Strategy 2: η-based potentials**. Correlation of prediction $\{\partial_{\boldsymbol{F}} e_{nn}, \partial_{\boldsymbol{D}_0} e_{nn}\}$ and testing data $\{\partial_{\boldsymbol{F}} e, \partial_{\boldsymbol{D}_0} e\}$ using a Mooney-Rivlin model (in red) for Ψ_m and ideal dielectric model (in blue) for Ψ_{em} for ground truth Helmholtz strain energy model used for the calibration (see (33)). The training data represents a subset of the testing data containing the 20% of the data in the latter. Architecture of 4 layers and 8 neurons per layer.

Remark 3. Notice that Figures 13-15 do not include predictions of the neural network-based models for their derivatives with respect to either θ or η. The underlying reason is that these neural network models have been calibrated using **Calibration Strategy 2**, where data for η are unavailable. For θ-based potentials, θ serves as the input, and the derivative of the potential is given by $\partial_\theta \Psi_{nn} = -\eta$ or $\partial_\theta \Upsilon_{nn} = -\eta$. However, since data for η are unavailable, the prediction of η cannot be directly compared to (unavailable) data. In contrast, for η-based potentials, the relationship $\partial_\eta e_{nn} = \theta$ or $\partial_\eta \Gamma_{nn} = \theta$ is satisfied exactly (as stated in equation (52)). This means that the prediction is inherently accurate, not only during training but also for any test data point, because it is enforced by construction. That is the reason why plots of predictions of temperature or entropy derivatives do not make sense for this approach.

6.4. Finite element numerical experiments

The objective of this example is to test the accuracy of thermo-electro-mechanical neural network models in the context of complex finite element simulations. For that purpose, we will make use of an example explored previously by the authors in [26]. This example considers a dielectric plate with a heating spot and its geometry and boundary conditions are depicted in Figure 16. With regards to the finite element discretization employed, it comprises $100 \times 100 \times 2$ quadratic hexahedral elements for the discretization of the three fields $\{\boldsymbol{\phi}, \varphi, \theta\}$, yielding a total of 1 1010 025 degrees of freedom. The following time dependent electric potential Dirichlet boundary conditions (see Figure 16) are employed

$$\varphi_1 = 0; \qquad \varphi_2 = 0.3 \times \begin{cases} \sin\left(\dfrac{\pi t}{2}\right) & \text{for } t \leq 1\,\text{s} \\ 1 & \text{for } t > 1\,\text{s} \end{cases} \text{(V)}. \tag{89}$$

Furthermore, we consider the following sinusoidal heat flux $\mathcal{Q}_\theta$ applied in the circled region of Figure 16, with value

$$\mathcal{Q}_\theta = \frac{X}{A_0} f(t); \qquad f(t) = \begin{cases} \sin\left(\dfrac{\pi t}{2}\right) & \text{for } t \leq 1\,\text{s} \\ 0 & \text{for } t > 1\,\text{s} \end{cases} \text{(W/m}^2\text{)}. \tag{90}$$

where $A_0 = \pi r^2$, $r = 2.5$.

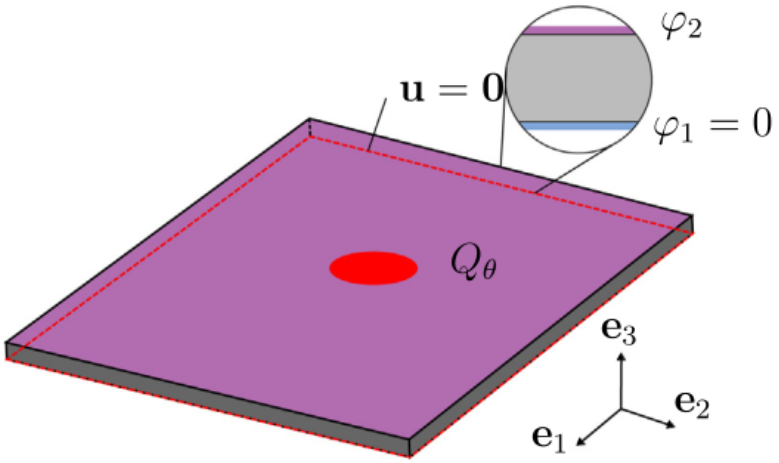

Figure 16: **FEM numerical example**. Geometry ($100 \times 100 \times 1$) and boundary conditions. Mechanical boundary conditions (left) where $\boldsymbol{u}(X_1 = 0, X_2, X_3 = 0) = \boldsymbol{u}(X_1 = 100, X_2, X_3 = 0) = \boldsymbol{u}(X_1, X_2 = 0, X_3 = 0) = \boldsymbol{u}(X_1, X_2 = 100, X_3 = 0) = 0$ and applied electric potentials φ_1, φ_2 (mid) corresponding to (89) and heat flow $\mathcal{Q}_\theta$ (right) corresponding to (90).

We simulated this problem using the Helmholtz potential $\Psi(\boldsymbol{F}, \boldsymbol{E}_0, \theta)$ as the ground truth model, where the mechanical contribution Ψ_m follows a Yeoh model and the dielectric contribution Ψ_{em} is modeled as ideal, as described in equation (33). Additionally, the problem was simulated using the Helmholtz neural network-based potential, $\Psi_{nn}(\boldsymbol{F}, \boldsymbol{E}_0, \theta)$, to analyze the agreement between the simulations from both models. It is worth noting that alternative calibrated potentials, such as $e_{nn}(\boldsymbol{F}, \boldsymbol{D}_0, \eta)$, $\Upsilon_{nn}(\boldsymbol{F}, \boldsymbol{E}_0, \eta)$, or $\Gamma_{nn}(\boldsymbol{F}, \boldsymbol{D}_0, \theta)$, could have been used instead. The results for both models are shown in Figure 17, 18 and 19, illustrating the time evolution of deformed configuration of both models, and showing a good agreement between both ground truth and neural network models in terms of displacements, stresses (the hydrostatic pressure $p = \frac{1}{3} J^{-1} \boldsymbol{P}\boldsymbol{F}^T$ is shown) and one of the components of the electric displacement field $\boldsymbol{D}_0$.

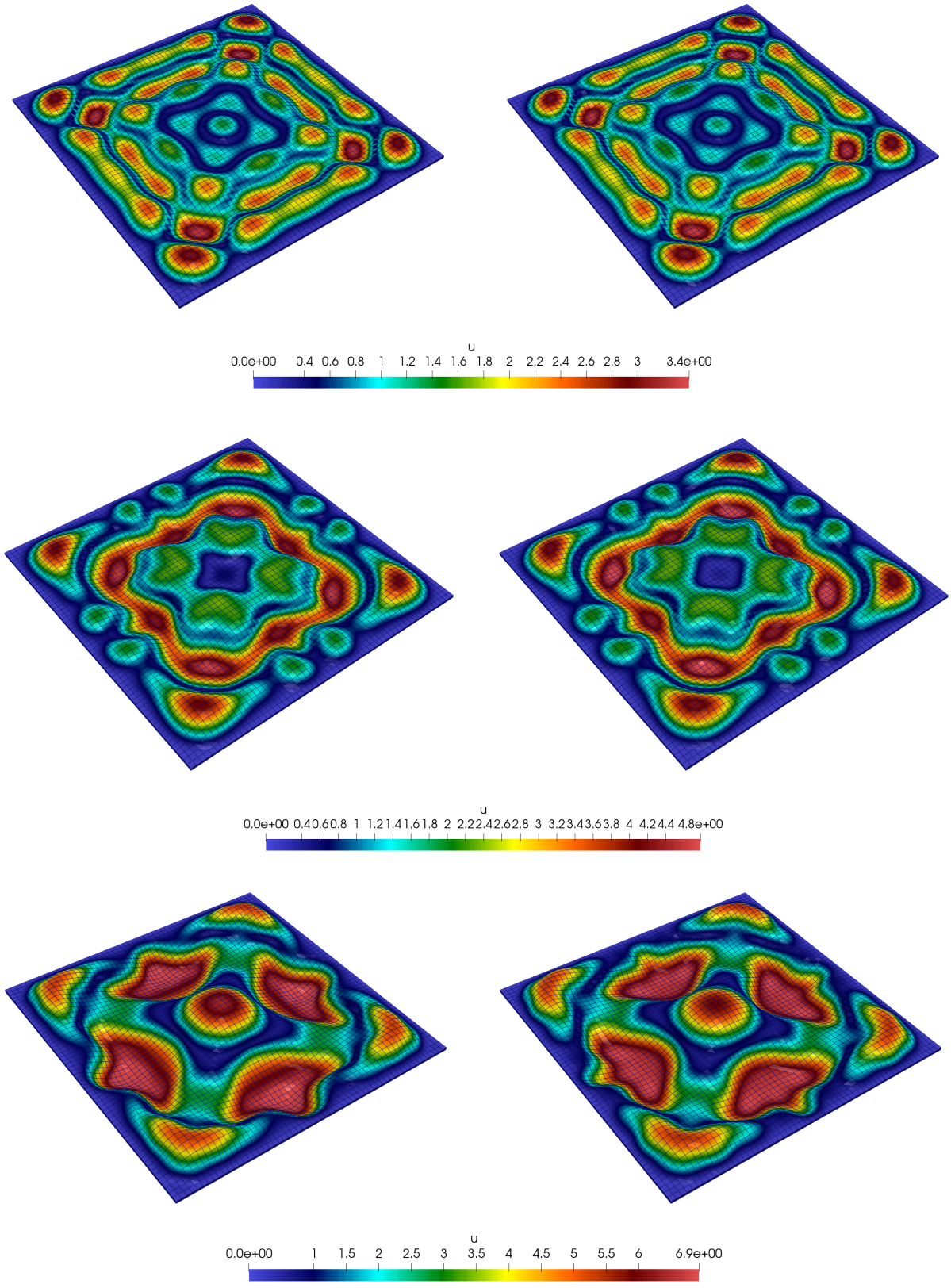

Figure 17: **FEM numerical example**. Left: ground truth model; Right: neural network-based model. Deformed configuration and contour plot of $||\boldsymbol{u}||$ for time steps: $t = 0.7$ (s); $t = 0.9$ (s); $t = 1.1$ (s).

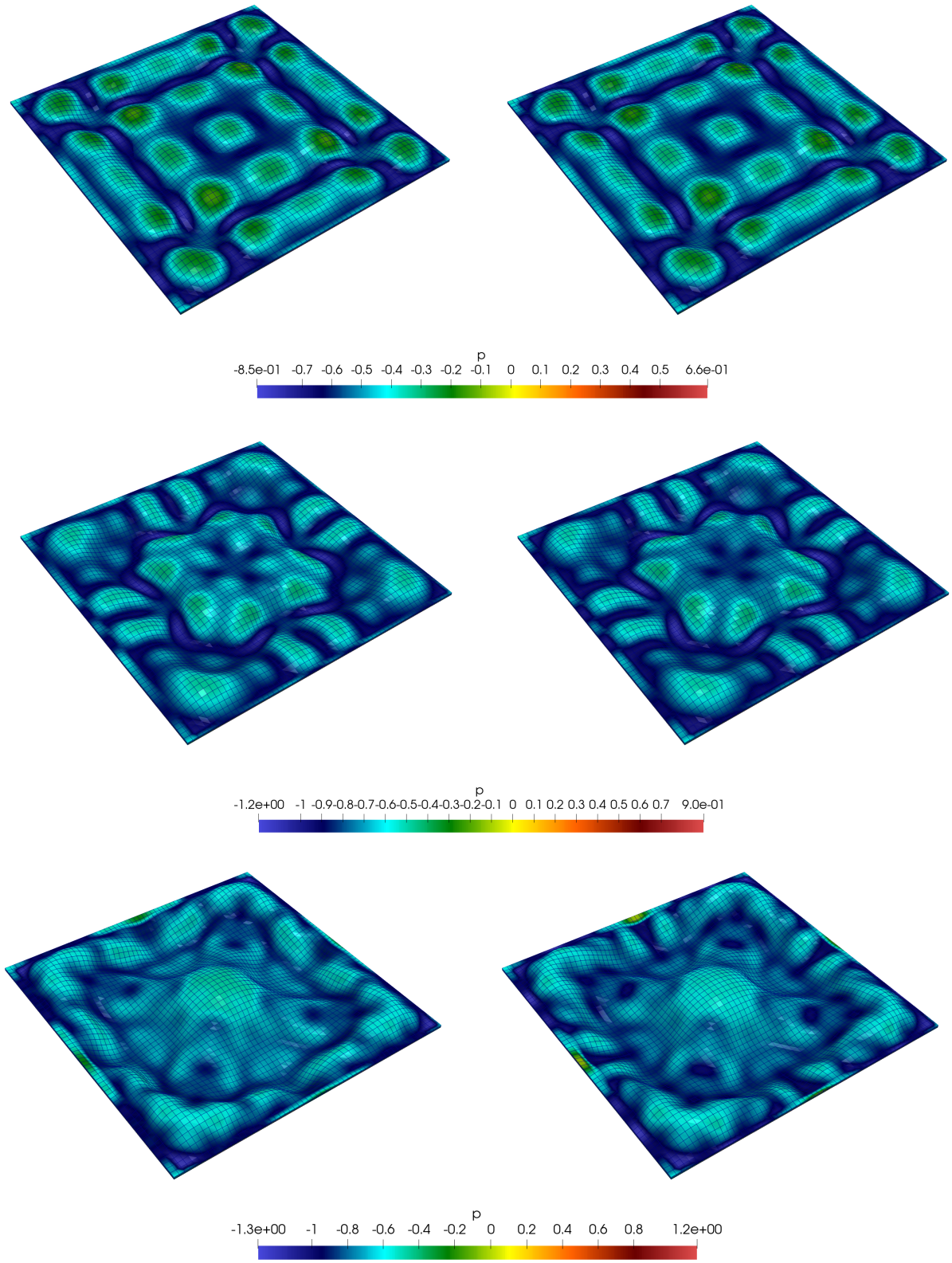

Figure 18: **FEM numerical example**. Left: ground truth model; Right: neural network-based model. Deformed configuration and contour plot of hydrostatic pressure p for time steps: $t = 0.7$ (s); $t = 0.9$ (s); $t = 1.1$ (s).

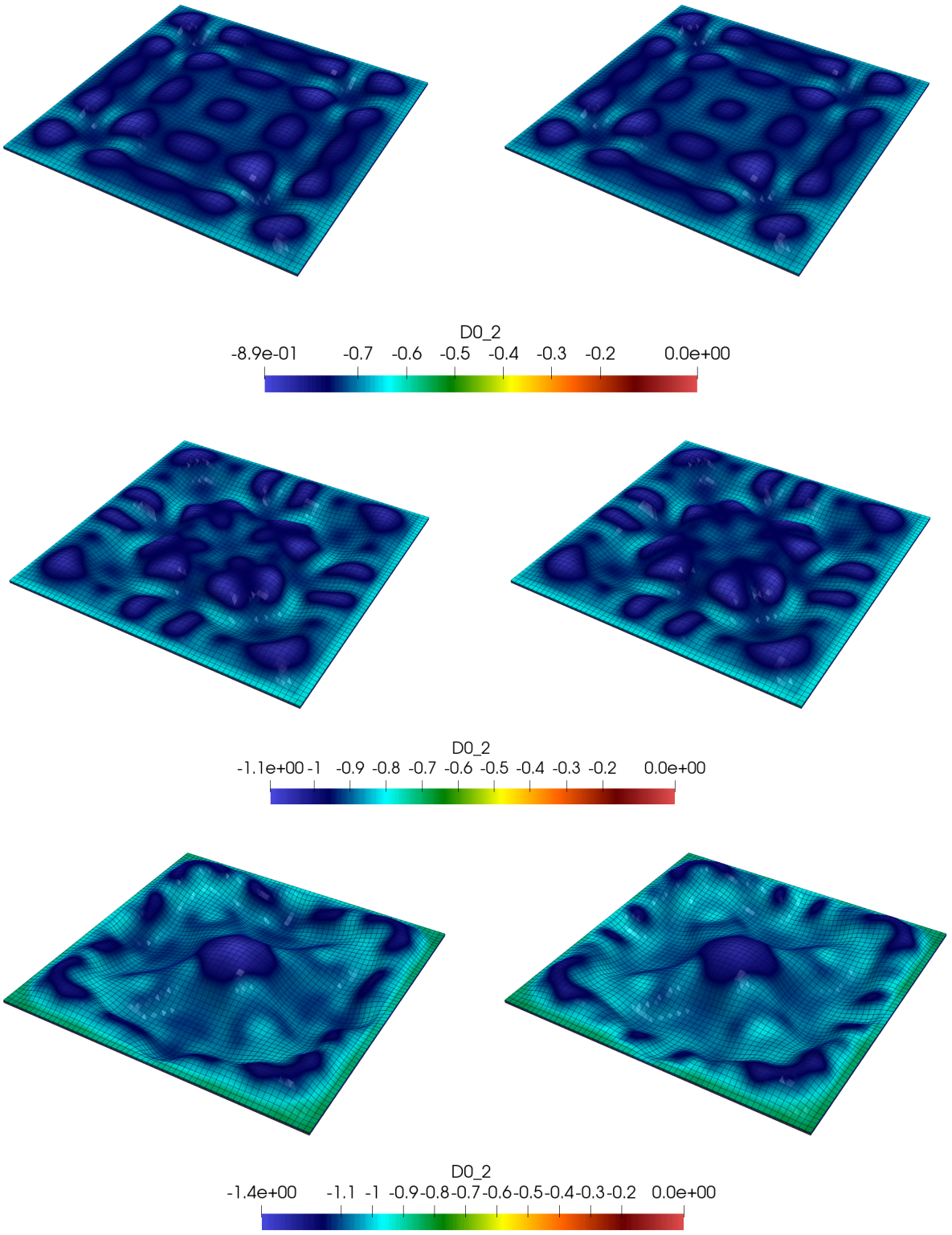

Figure 19: **FEM numerical example**. Left: ground truth model; Right: neural network-based model. Deformed configuration and contour plot of $(\boldsymbol{D}_0)_2$ for time steps: $t = 0.7$ (s); $t = 0.9$ (s); $t = 1.1$ (s).

7. Conclusions

This manuscript has presented a neural network-based constitutive modeling framework for thermo-electro-mechanically coupled materials at finite strains. The proposed framework has demonstrated significant flexibility, enabling the calibration of neural network-based constitutive models with different input forms, such as $\Psi_{nn}(\boldsymbol{F}, \boldsymbol{E}_0, \theta)$, $e_{nn}(\boldsymbol{F}, \boldsymbol{D}_0, \eta)$, $\Upsilon_{nn}(\boldsymbol{F}, \boldsymbol{E}_0, \eta)$, or $\Gamma_{nn}(\boldsymbol{F}, \boldsymbol{D}_0, \theta)$. All models adhere to physical and material symmetry principles by utilizing the appropriate set of isotropic or anisotropic invariants—depending on the material symmetry group of the underlying ground truth potential—for the respective input fields: $\{\boldsymbol{F}, \boldsymbol{E}_0, \theta\}$, $\{\boldsymbol{F}, \boldsymbol{D}_0, \eta\}$, $\{\boldsymbol{F}, \boldsymbol{E}_0, \eta\}$, or $\{\boldsymbol{F}, \boldsymbol{D}_0, \theta\}$.

Two distinct calibration strategies have been introduced. The first, particularly suitable for in-silico data generation, minimises the derivatives of the various potentials, such as $\Psi_{nn}(\boldsymbol{F}, \boldsymbol{E}_0, \theta)$, $e_{nn}(\boldsymbol{F}, \boldsymbol{D}_0, \eta)$, $\Upsilon_{nn}(\boldsymbol{F}, \boldsymbol{E}_0, \eta)$, or $\Gamma_{nn}(\boldsymbol{F}, \boldsymbol{D}_0, \theta)$, with respect to their ground truth counterparts, necessitating the use of appropriate Legendre transformations on the ground truth model.

The second strategy is designed for calibrating models with data collected from experimental settings, where the entropy field η is typically unmeasurable. In this more physically-grounded calibration approach, the absence of the field η introduces technical differences in the calibration process between potentials dependent on θ and those dependent on η. The latter requires the implicit satisfaction of the work conjugacy relation between the fields η and θ.

A thorough calibration study was conducted for both strategies, evaluating different neural network architectures and a wide range of ground truth constitutive models. The excellent agreement in the predictive performance of the calibrated models on larger datasets, compared to those used during calibration, is reflected in the results of a complex finite element simulation carried out using both the ground truth and neural network-based models.

8. Acknowledgements

R. Ortigosa, J. Martínez-Frutos and I. Castañar acknowledge the support of grant PID2022-141957OA-C22 funded by MICIU/AEI/10.13039/501100011033 and by "ERDF A way of making Europe". R. Ortigosa and J. Martínez-Frutos also acknowledge the support provided by the Autonomous Community of the Region of Murcia, Spain through the programme for the development of scientific and technical research by competitive groups (21996/PI/22), included in the Regional Program for the Promotion of Scientific and Technical Research of Fundacion Seneca - Agencia de Ciencia y Tecnologia de la Region de Murcia. N. Ellmer and A. J. Gil acknowledge the support provided by the defence, science and technology laboratory (Dstl), United Kingdom. A. J. Gil acknowledges the financial support provided by the Leverhulme Trust.

Appendix A. In-silico data generation strategy

In this section, we present the procedure used for generating synthetic data for the training strategy denoted as strategy 1. For that, we have made use of the generic form of the Helmholtz free energy density in equation (33), and a variety of models for the isothermal purely mechanical and electro-mechanical contributions $\Psi_m(\boldsymbol{F})$ (see Table 1) and $\Psi_{em}(\boldsymbol{F}, \boldsymbol{E}_0)$ (refer to Table 2).

To acquire the dataset, we have adhered to the procedure outlined in [43], extended to the coupled context of thermo-electro-mechanics. The deformation gradient tensor $\boldsymbol{F}$ is parameterized via a chosen set of deviatoric directions, amplitudes, and Jacobians (J, i.e., the determinant of $\boldsymbol{F}$). The process of generating sample points for deviatoric directions, amplitudes, and Jacobians is elucidated in Algorithm 1. Similarly, the electric displacement $\boldsymbol{E}_0$ (for the neural network-based potentials $\Psi_{nn}(\boldsymbol{F}, \boldsymbol{E}_0, \theta)$ and $\Upsilon_{nn}(\boldsymbol{F}, \boldsymbol{E}_0, \eta)$) or $\boldsymbol{D}_0$ (for the neural network-based potentials $e_{nn}(\boldsymbol{F}, \boldsymbol{D}_0, \eta)$ and $\Gamma_{nn}(\boldsymbol{F}, \boldsymbol{D}_0, \theta)$) is also parametrised in terms of unitary directions and amplitudes. Concerning the deviatoric directions for $\boldsymbol{F}$, denoted as $\boldsymbol{V_F}$ we formulate them using a spherical parametrization in $\mathbb{R}^5$, precisely representing these directions using five pertinent angular measures ($\phi_1, \phi_2, \phi_3, \phi_4, \phi_5 \in [0, 2\pi] \times [0, \pi] \times [0, \pi] \times [0, \pi] \times [0, \pi]$) within this 5-dimensional space. For the directions employed for the parametrisation of $\boldsymbol{E}_0$ or $\boldsymbol{D}_0$ (depending on the dependence on the electrical physics of the neural network-based potential), denoted as $\boldsymbol{V}_{\boldsymbol{E}_0}$ or $\boldsymbol{V}_{\boldsymbol{D}_0}$, respectively, these are created using a spherical parametrization in $\mathbb{R}^3$, using as angular measures $(\theta, \psi) \in [0, 2\pi] \times [0, \pi]$, namely

Algorithm 1 Pseudo-code for sample generation

1: Generate deformation gradient tensors $\boldsymbol{F}$ according to:

1.1: Set the number of amplitudes, directions and determinants: $\{n_{\boldsymbol{t_F}}, n_{\boldsymbol{V_F}}, n_{\boldsymbol{J_F}}\}$;
1.2: Initialise a vector of Latin Hypercube Sampled angles: $\boldsymbol{\phi}_1 = [0, 2\pi]_{n_{\boldsymbol{V_F}} \times 1}$ and $\boldsymbol{\phi}_{2,\ldots,4} = [0, \pi]_{n_{\boldsymbol{V_F}} \times 1}$;
1.3: Construct the directions, $\boldsymbol{V}_F$, using $\boldsymbol{\phi}_1, \ldots, \boldsymbol{\phi}_4$ by means of an extended Spherical parametrisation in $\mathbb{R}^5$ - detailed in (A.1);
1.4: Evaluate the deformation gradient tensors, $\boldsymbol{F}$ - detailed in Algorithm 2;

2: Generate electric field vectors $\boldsymbol{E}_0$ (or $\boldsymbol{D}_0$) according to:

2.1: Set the amplitudes and directions: $\{n_{\boldsymbol{t}_{\boldsymbol{E}_0}}, n_{\boldsymbol{V}_{\boldsymbol{E}_0}}\}$;
2.2: Initialise a vector of Latin Hypercube Sampled angles: $\boldsymbol{\psi}_1 = [0, 2\pi]_{n_{\boldsymbol{V}_{\boldsymbol{E}_0}} \times 1}$ and $\boldsymbol{\psi}_2 = [0, \pi]_{n_{\boldsymbol{V}\boldsymbol{E}_0} \times 1}$;
2.3: Construct the directions, $\boldsymbol{V}_{\boldsymbol{E}_0}$ (or $\boldsymbol{V}_{\boldsymbol{D}_0}$), using $\boldsymbol{\psi}_1, \boldsymbol{\psi}_2$ by means of a Spherical parametrisation in $\mathbb{R}^3$;
2.4: Evaluate the deformation $\boldsymbol{E}_0$ (or $\boldsymbol{D}_0$) - detailed in Algorithm 2;

3: Generate temperature data θ (or entropy η) according to:

3.1: Set the maximum temperature difference with respect to θ_R, denoted $\Delta\theta$. Then define the minimum and maximum values of θ: $\theta_R - \Delta\theta$ and $\theta_R + \Delta\theta$; For η-based potentials, set $\eta_{\min}$ and $\eta_{\max}$;
3.2: Set number of temperatures n_θ (or n_η);
3.3: Generate n_θ uniformly distributed temperature (or randomly) in the interval $(\theta_R - \Delta\theta, \theta_R + \Delta\theta)$; For η-based potentials, the interval is $(\eta_{\min}, \eta_{\max})$;

4: Generate combination of data of $\{\boldsymbol{F}, \boldsymbol{E}_0, \theta\}$ (or any other combination, for instance $\{\boldsymbol{F}, \boldsymbol{D}_0, \eta\}$)

$$\boldsymbol{V}_{\boldsymbol{F}}^i = \begin{bmatrix} \cos\phi_1^i \\ \sin\phi_1^i\cos\phi_2^i \\ \sin\phi_1^i\sin\phi_2^i\cos\phi_3^i \\ \sin\phi_1^i\sin\phi_2^i\sin\phi_3^i\cos\phi_4^i \\ \sin\phi_1^i\sin\phi_2^i\sin\phi_3^i\sin\phi_4^i \end{bmatrix};\ 1\le i\le n_{\boldsymbol{V_F}}; \qquad \boldsymbol{V}_{\boldsymbol{E}_0}^i = \begin{bmatrix} \cos\psi_1^i\sin\psi_2^i \\ \sin\psi_1^i\sin\psi_2^i \\ \cos\psi_2^i \end{bmatrix};\ 1\le i\le n_{\boldsymbol{V}_{\boldsymbol{E}_0}} \tag{A.1}$$

Once the sample is generated following Algorithm 1, the reconstruction of the deformation gradient tensor $\boldsymbol{F}$ and of $\boldsymbol{D}_0$ becomes possible at each of the sampling points. This reconstruction process is demonstrated in Algorithm 2, where $\boldsymbol{\Psi}$ represents the basis for symmetric and traceless tensors, defined as

$$\Psi_1 = \sqrt{\frac{1}{6}}\begin{bmatrix} 2 & 0 & 0 \\ 0 & -1 & 0 \\ 0 & 0 & -1 \end{bmatrix} \qquad \Psi_2 = \sqrt{\frac{1}{2}}\begin{bmatrix} 0 & 0 & 0 \\ 0 & 1 & 0 \\ 0 & 0 & -1 \end{bmatrix} \qquad \Psi_3 = \sqrt{\frac{1}{2}}\begin{bmatrix} 0 & 1 & 0 \\ 1 & 0 & 0 \\ 0 & 0 & 0 \end{bmatrix} \tag{A.2}$$

$$\Psi_4 = \sqrt{\frac{1}{2}}\begin{bmatrix} 0 & 0 & 1 \\ 0 & 0 & 0 \\ 1 & 0 & 0 \end{bmatrix} \qquad \Psi_5 = \sqrt{\frac{1}{2}}\begin{bmatrix} 0 & 0 & 0 \\ 0 & 0 & 1 \\ 0 & 1 & 0 \end{bmatrix} \tag{A.3}$$

For the temperature field θ, data generation has been carried out by predefining the maximum difference with respect to the reference temperature θ_R. This approach establishes the lower and upper bounds $\theta_R - \Delta\theta$ and $\theta_R + \Delta\theta$. Consequently, the data for this field is generated either uniformly distributed within this interval or randomly sampled across the defined range.

Algorithm 2 Pseudo-code for construction of the set of deformation gradient tensors and electric fields $\boldsymbol{E}_0$ (similarly for $\boldsymbol{D}_0$)

for $i = 1 : n_{\boldsymbol{V_F}}$ **do**
  for $j = 1 : n_J$ **do**
    for $k = 1 : n_{\boldsymbol{t_F}}$ **do**
      $\boldsymbol{F} = J_j^{1/3}\exp\left([\boldsymbol{t_F}]_k\left[\sum_{m=1}^5[\boldsymbol{V}_{\boldsymbol{F}}^i]_m\boldsymbol{\Psi}_m\right]\right)$;
    end for
  end for
end for
for $i = 1 : n_{\boldsymbol{V}_{\boldsymbol{E}_0}}$ **do**
  for $j = 1 : n_{\boldsymbol{t}_{\boldsymbol{E}_0}}$ **do**
    $\boldsymbol{E}_0 = [\boldsymbol{t}_{\boldsymbol{E}_0}]_j\boldsymbol{V}_{\boldsymbol{E}_0}^i$;
  end for
end for

Notice that the deformation gradient tensor $\boldsymbol{F}$, is defined in terms of the amplitude variable $t_{\boldsymbol{F}}$, the angles $\{\phi_1, \phi_2, \phi_3, \phi_4\}$ and the Jacobian J. The range of values for angular fields $\{\phi_1, \phi_2, \phi_3, \phi_4\}$ has been mentioned above. For $t_{\boldsymbol{F}}$ and J, the lower and upper bounds considered both in training and testing data sets are

$$-0.5 \le t_{\boldsymbol{F}} \le 1.5; \qquad 0.8 \le J \le 1.2 \tag{A.4}$$

For training, the number of deviatoric directions, and hence, the number of angular variables $\{\phi_1, \phi_2, \phi_3, \phi_4\}$, is $n_{\boldsymbol{V_F}} = 20$. The total number of amplitudes is $n_{t_{\boldsymbol{F}}} = 10$, whilst the total number of Jacobians is $n_J = 3$.

For the parametrization of the electric field $\boldsymbol{E}_0$ (or $\boldsymbol{D}_0$), the range of the norm of $\boldsymbol{E}_0$ (or $\boldsymbol{D}_0$), namely $t_{\boldsymbol{E}_0}$ (or $t_{\boldsymbol{D}_0}$) is $0 \leq t_{\boldsymbol{E}_0} \leq 2.2\sqrt{\frac{\mu}{\varepsilon}}$ (or $0 \leq t_{\boldsymbol{D}_0} \leq 2.2\sqrt{\mu\varepsilon}$), with $n_{t_{\boldsymbol{E}_0}} = 10$. In addition, we used $n_{\boldsymbol{V}_{\boldsymbol{E}_0}} = 10$ for the possible orientations of the electric field.

With regards to the temperature field θ, for training we consider $n_\theta = 15$ values for $\Delta\theta$, ranging between $0 \leq \Delta\theta \leq 60$, hence $\theta_R - 60 \leq \theta \leq \theta_R + 60$.

Based on the described parameterization of $\boldsymbol{F}$, $\boldsymbol{E}_0$ and θ, the training dataset would independently consist of $10 \times 20 \times 3$, 15×20 and 15 data points for each respective parameter. However, combining the datasets across the three physical variables would result in 9×10^5 data points for $\{\boldsymbol{F}, \boldsymbol{E}_0, \theta\}$. This naive approach would yield an excessively large dataset, posing significant challenges for training. Instead, the combined training dataset for $\{\boldsymbol{F}, \boldsymbol{E}_0, \theta\}$ is set to never exceed 10^4 data points in our calibrations.

For the test dataset, we tend to multiply by a factor of 3 the variables $n_{\boldsymbol{V}_{\boldsymbol{F}}}$, $n_{t_{\boldsymbol{F}}}$, n_J, $n_{t_{\boldsymbol{E}_0}}$, $n_{\boldsymbol{V}_{\boldsymbol{E}_0}}$ and n_θ.

References

[1] E. B. Anderes. *Kriging, Encyclopedia of Environmetrics*. 2013.

[2] J. M. Ball. Convexity conditions and existence theorems in nonlinear elasticity. *Archive for Rational Mechanics and Analysis*, 63(4):337–403, 1976.

[3] J. M. Ball. Energy-minimising configurations in nonlinear elasticity. *Archive for Rational Mechanics and Analysis*, 63(4):337–403, 1976.

[4] J. M. Ball. *Geometry, Mechanics and Dynamics*, chapter Some open problems in Elasticity, pages 3–59. Springer, 2002.

[5] J. M. Ball and F. Murat. $W^{1,p}$-quasiconvexity and variational problems for multiple integrals. *Journal of Functional Analysis*, 58(3):225–253, 1984.

[6] A. K. Bastola and M. Hossain. The shape – morphing performance of magnetoactive soft materials. *Materials and Design*, 211:110172, 2021.

[7] K. J. Bathe. *Finite Element Procedures*. Prentice Hall, 1996.

[8] C. M. Bishop. *Pattern Recognition and Machine Learning*. Springer, 2006.

[9] J. Bonet, A. J. Gil, and R. Ortigosa. On a tensor cross product based formulation of large strain solid mechanics. *International Journal of Solids and Structures*, 84:49–63, 2016.

[10] J. Bonet, A. J. Gil, and R. D. Wood. *Nonlinear Continuum Mechanics for Finite Element Analysis: Statics*. Cambridge University Press, 2016.

[11] R. Bustamante. Transversely isotropic non-linear electro-active elastomers. *Acta Mechanica*, 206(3-4):237–259, 2009.

[12] R. Bustamante, A. Dorfmann, and R.W. Ogden. Nonlinear electroelastostatics: a variational framework. *Zeitschrift für angewandte Mathematik und Physik*, 60(1):154–177, 2009.

[13] R. Bustamante, A. Dorfmann, and R.W. Ogden. On electric body forces and Maxwell stresses in nonlinearly electroelastic solids. *International Journal of Engineering Science*, 47(11-12):1131–1141, 2009.

[14] R. Bustamante and J. Merodio. Constitutive structure in coupled non-linear electroelasticity: Invariant descriptions and constitutive restrictions. *International Journal of Non-Linear Mechanics*, 46(10):1315 – 1323, 2011.

[15] Jiawei Cao, Lei Qin, Jun Liu, Qinyuan Ren, Choon C Foo, Hongqiang Wang, Heow P Lee, and Jian Zhu. Untethered soft robot capable of stable locomotion using soft electrostatic actuators. *Extreme Mechanics Letters*, 21:9–16, 2018.

[16] Federico Carpi and Danilo De Rossi. Bioinspired actuation of the eyeballs of an adroid robotic face: concept and preliminary investigations. *Bioinspiration & Biomimetics*, 2:50–63, 2007.

[17] Yufeng Chen, Huichan Zhao, Jie Mao, Pakpong Chirarattananon, Elizabeth F Helbling, Nak seung P Hyun, David R Clarke, and Robert J Wood. Controlled flight of a microrobot powered by soft artificial muscles. *Nature*, 575:324–329, 2019.

[18] R. de Boer. *Vektor- und Tensorrechnung für Ingenieure*. Springer-Verlag, 1982.

[19] E.A. de Souza Neto, D. Períc, and D.R.J. Owen. *Computational Methods for Plasticity. Theory and Applications*. 2008.

[20] A. Dorfmann and R. W. Ogden. Nonlinear electroelasticity. *Acta Mechanica*, 174(3-4):167–183, 2005.

[21] A. Dorfmann and R. W. Ogden. Electroelastic waves in a finitely deformed electroactive material. *IMA Journal of Applied Mathematics*, 75(4):603–636, 2010.

[22] A. Dorfmann and R.W. Ogden. Nonlinear electroelastic deformations. *Journal of Elasticity*, 82(2):99–127, 2006.

[23] N. Ellmer, R. Ortigosa, J. Martínez-Frutos, and A. J. Gil. Gradient based hyper-parameter optimisation for well conditioned kriging metamodels. *Computer Methods in Applied Mechanics and Engineering*, 418:1–32, 2024.

[24] M. Flaschel, S. Kumar, and L. D. Lorenzis. Automated discovery of generalized standard material models with euclid. *Computer Methods in Applied Mechanics and Engineering*, 405:1–26, 2023.

[25] M Franke, A. Janz, M. Schiebl, and P. Betsch. An energy momentum consistent integration scheme using a polyconvexity-based framework for nonlinear thermo-elastodynamics. *International Journal for Numerical Methods in Engineering*, 115:549–577, 2018.

[26] M. Franke, R. Ortigosa, J. Martínez-Frutos, A.J. Gil, and P. Betsch. A thermodynamically consistent time integration scheme for non-linear thermo-electro-mechanics. *Computer Methods in Applied Mechanics and Engineering*, 389:114298, 2022.

[27] A. L. Frankel, R. E. Jones, and L. P. Swiler. Tensor basis gaussian process model of hyperelastic materials. *Journal of Machine Learning for Modeling and Computing*, 1:1–17, 2020.

[28] J. Fuhg, A. Jadoon, O. Weeger, D. Seidl, and R. Jones. Polyconvex neural network models of thermoelasticity. *Journal of the Mechanics and Physics of Solids*, 192, 2024.

[29] A. J. Gil and R. Ortigosa. A new framework for large strain electromechanics based on convex multi-variable strain energies: variational formulation and material characterisation. *Computer Methods in Applied Mechanics and Engineering*, 302:293–328, 2016.

[30] O. Gonzalez and A. M. Stuart. *A first course in Continuum Mechanics*. Cambridge University Press, 2008.

[31] J. Gonzalez-Rico, S. Garzon-Hernandez, C. M. Landis, and D. Garcia-Gonzalez. Magneto-mechanically derived diffusion processes in ultra-soft biological hydrogels. *Journal of the Mechanics and Physics of Solids*, 192:105791, 2024.

[32] M. Horak, A. J. Gil, R. Ortigosa, and M. Kruzik. A polyconvex transversely-isotropic invariant-based formulation for electro-mechanics: Stability, minimisers and computational implementation. *Computer Methods in Applied Mechanics and Engineering*, 403:115695, 2023.

[33] M. Itskov and V. N. Khiêm. A polyconvex anisotropic free energy function for electro- and magneto-rheological elastomers. *Mathematics and Mechanics of Solids*, pages 1–12, 2014.

[34] C Jordi, S Michel, and E Fink. Fish-like propulsion of an airship with planar membrane dielectric elastomer actuators. *Bioinspiration & Biomimetics*, 5:1–9, 2010.

[35] A. Joshi, P. Thakolkaran, Y. Zheng, M. Escande, M. Flaschel, L. D. Lorenzis, and S. Kumar. Bayesian-euclid: Discovering hyperelastic material laws with uncertainties. *Computer Methods in Applied Mechanics and Engineering*, 398:1–37, 2022.

[36] K. Kalina, Gebhart P, J. Brummund, L. Linden, W. Sun, and M. Kastner. Neural network-based multiscale modeling of finite strain megneto-elasticity with relaxed convexity criteria. *Computer Methods in Applied Mechanics and Engineering*, 421, 2024.

[37] D. Klein, R. Ortigosa, J. Martínez-Frutos, and O. Weeger. Nonlinear electro-elastic finite element analysis with neural network constitutive models. *Computer Methods in Applied Mechanics and Engineering*, 425, 2024.

[38] D. Klein, F. Roth, I. Valizadeh, and O. Weeger. Parametrized polyconvex hyperelasticity with physics-augmented neural networks. *Data-Centric Engineering*, 2023.

[39] D. K. Klein, M. Fernández, R. J. Martin, P. Neff, and O. Weeger. Polyconvex anisotropic hyperelasticity with neural networks. *Journal of the Mechanics and Physics of Solids*, 159:1–25, 2022.

[40] D. K. Klein, R. Ortigosa, and O. Weeger J. Martínez-Frutos. Finite electro-elasticity with physics-augmented neural networks. *Computer Methods in Applied Mechanics and Engineering*, 400:1–33, 2022.

[41] D. K. Klein, R. Ortigosa, and O. Weeger J. Martínez-Frutos. Nonlinear electro-elastic finite element analysis with neural network constitutive models. *Computer Methods in Applied Mechanics and Engineering*, 425:1–25, 2024.

[42] G. Kofod, P. Sommer-Larsen, R. Kornbluh, and R. Pelrine. Actuation response of polyacrylate dielectric elastomers. *Journal of Intelligent Material Systems and Structures*, 14(12):787–793, 2003.

[43] Oliver Kunc and Felix Fritzen. Finite strain homogenization using a reduced basis and efficient sampling. *Mathematical and Computational Applications*, 24:1–28, 2019.

[44] Guorui Li, Xiangping Chen, Fanghao Zhou, Yiming Liang, Youhua Xiao, Xunuo Cao, Zhen Zhang, Mingqi Zhang, Baosheng Wu, Shunyu Yin, Yi Xu, Hongbo Fan, Zheng Chen, Wei Song, Wenjing Yang, Binbin Pan, Jiaoyi Hou, Weifeng Zou, Shunping He, Xuxu Yang, Guoyong Mao, Zheng Jia, Haofei Zhou, Tiefeng Li, Shaoxing Qu, Zhongbin Xu, Zhilong Huang, Yingwu Luo, Tao Xie, Jason Gu, Shiqiang Zhu, and Wei Yang. Self-powered soft robot in the mariana trench. *Nature*, 591:66–71, 2021.

[45] T. Li, C. Keplinger, R. Baumgartner, S. Bauer, W. Yang, and Z. Suo. Giant voltage-induced deformation in dielectric elastomers near the verge of snap-through instability. *Journal of the Mechanics and Physics of Solids*, 61(2):611–628, 2013.

[46] K. Linka, M. Hillgartner, K. P. Abdolazizi, R. C. Aydin, M. Itskov, and C. J. Cryon. Constitutive artificial neural networks: A fast and general approach to predictive data-driven constitutive modeling by deep learning. *Journal of Computational Physics*, 429:1–17, 2021.

[47] K. Linka and E. Kuhl. A new family of constitutive artificial neural networks towards automated model discovery. *Computer Methods in Applied Mechanics and Engineering*, 403:1–27, 2023.

[48] Tongqing Lu, Zhibao Shi, Qian Shi, and T J Wang. Bioinspired bicipital muscle with fibre-constrained dielectric elastomer actuator. *Extreme Mechanics Letters*, 6:75–81, 2016.

[49] J. I. Marden. *Multivariate Statistics: Old School*. CreateSpace Independent Publishing, 2015.

[50] M. Mehnert, M. Hossain, and P. Steinmann. Numerical modeling of thermo-electro-viscoelasticity with field-dependent material parameters. *International Journal of Non-Linear Mechanics*, 106:13–24, 2018.

[51] M. Mehnert, M. Hossain, and P. Steinmann. A complete thermo–electro–viscoelastic characterization of dielectric elastomers, part i: Experimental investigations. *Journal of the Mechanics and Physics of Solids*, 157:104603, 2021.

[52] M. A. Moreno-Mateos, M. Hossain, P. Steinmann, and D. García-González. Hybrid magnetorheological elastomers enable versatile soft actuators. *Nature*, 8, 2022.

[53] Canh T Nguyen, Hoa Phung, Tien D Nguyen, Hosang Jung, and Hyouk R Choi. Multiple-degrees-of-freedom dielectric elastomer actuators for soft printable hexapod robot. *Sensors and Actuators A: Physical*, 267:505–516, 2017.

[54] Chengyun Ning, Zhengnan Zhou, Guoxin Tan, Ye Zhu, and Chuanbin Mao. Electroactive polymers for tissue regeneration: Developments and perspectives. *Progress in Polymer Science*, 81:144–162, 2018.

[55] J. Ollar, C. Mortished, R. Jones, J. Sienz, and V. Toropov. Gradient based hyper-parameter optimisation for well conditioned kriging metamodels. *Structural and Multidisciplinary Optimization*, 55:2029–2044, 2017.

[56] R. Ortigosa and A. J. Gil. A new framework for large strain electromechanics based on convex multi-variable strain energies: Conservation laws, hyperbolicity and extension to electro-magneto-mechanics. *Computer Methods in Applied Mechanics and Engineering*, 309:202–242, 2016.

[57] R. Ortigosa and A. J. Gil. A new framework for large strain electromechanics based on convex multi-variable strain energies: Finite element discretisation and computational implementation. *Computer Methods in Applied Mechanics and Engineering*, 302:329–360, 2016.

[58] R. Ortigosa, A. J. Gil, and C. H. Lee. A computational framework for large strain nearly and truly incompressible electromecahnics based on convex multi-variable strain energies. *Computer Methods in Applied Mechanics and Engineering*, 310:297–334, 2016.

[59] R. Ortigosa, J. Martínez-Frutos, C. Mora-Corral, P. Pedregal, and F. Periago. Optimal control and design of magnetic field-responsive smart polymer composites. *Applied Mathematical Modelling*, 103:141–161, 2022.

[60] R. Pelrine, R. Kornbluh, Q. Pei, and J. Joseph. High-speed electrically actuated elastomers with strain greater than 100 %. *Science*, 287(5454):836–839, 2000.

[61] R. E. Pelrine, R. D. Kornbluh, and J. P. Joseph. Electrostriction of polymer dielectrics with compliant electrodes as a means of actuation. *Sensors and Actuators A: Physical*, 64(1):77–85, 1998.

[62] Ron Pelrine, Roy D. Kornbluh, Qibing Pei, Scott Stanford, Seajin Oh, Joseph Eckerle, Robert J. Full, Marcus A. Rosenthal, and Kenneth Meijer. Dielectric elastomer artificial muscle actuators: toward biomimetic motion, 2002.

[63] Martínez-Frutos J. Ortigosa R. et al Pérez-Escolar, A. Learning nonlinear constitutive models in finite strain electromechanics with gaussian process predictors. *Computational Mechanics*, 74, 2024.

[64] Carl Edward Rasmussen and Christopher K. I. Williams. *Gaussian Processes for Machine Learning*. The MIT Press, 11 2005.

[65] Govindjee S Reese, S. Theoretical and numerical aspects in the thermo-viscoelastic material behaviour of rubber-like polymers. *Mechanics of Time-Dependent Materials*, 1:357–396, 1997.

[66] J. Schröder. Anisotropic polyconvex energies. In J. Schröder and P. Neff, editors, *Poly-, quasi- and rank-one convexity in Applied Mechanics, volume 516 of CISM Courses and Lectures*, volume 516 of CISM Courses and Lectures, pages 53–105. Springer-Verlag, 2010.

[67] J. Schröder and P. Neff. Invariant formulation of hyperelastic transverse isotropy based on polyconvex free energy functions. *International Journal of Solids and Structures*, 40:401–445, 2003.

[68] J. Schröder, P. Neff, and D. Balzani. A variational approach for materially stable anisotropic hyperelasticity. *International Journal of Solids and Structures*, 42:4352–4371, 2005.

[69] J. Schröder, P. Neff, and V. Ebbing. Anisotropic polyconvex energies on the basis of crystallographic motived structural tensors. *Journal of Mechanics and Physics of Solids*, 56:3486–3506, 2008.

[70] J. Schröder, P. Wriggers, and D. Balzani. A new mixed finite element based on different approximations of the minors of deformation tensors. *Computer Methods in Applied Mechanics and Engineering*, 200(49-52):3583–3600, 2011.

[71] M. Silhavy. *The Mechanics and Thermodynamics of Continuous Media*. Springer, 1997.

[72] P. Thakolkaran, A. Joshi, Y. Zheng, M. Flaschel, L. D. Lorenzis, and S. Kumar. Nn-euclid: Deep-learning hyperelasticity without stress data. *Journal of the Mechanics and Physics of Solids*, 169:1–29, 2022.

[73] Rocco Vertechy, Giovanni Berselli, Vincenzo Parenti Castelli, and Massimo Bergamasco. Continuum thermo-electro-mechanical model for electrostrictive elastomers. *Journal of Intelligent Material Systems and Structures*, 24(6):761–778, 2013.

[74] Yuzhe Wang and Jian Zhu. Artificial muscles for jaw movements. *Extreme Mechanics Letters*, 6:88–95, 2016.